

**ISTANBUL TECHNICAL UNIVERSITY ★ GRADUATE SCHOOL OF**  
**SCIENCE ENGINEERING AND TECHNOLOGY**

**CAPACITANCE-VOLTAGE AND CURRENT-VOLTAGE  
CHARACTERISTIC PROPERTIES OF ZnO:Al/p-Si HETEROJUNCTION**

**M.Sc. THESIS**

**Yeliz KÖSE**

**Metallurgical and Materials Engineering Department**

**Materials Engineering Master Program**

**Thesis Advisor: Assoc. Prof. Dr. Murat BAYDOĞAN**

**DECEMBER 2015**



**ISTANBUL TECHNICAL UNIVERSITY ★ GRADUATE SCHOOL OF**  
**SCIENCE ENGINEERING AND TECHNOLOGY**

**CAPACITANCE-VOLTAGE AND CURRENT-VOLTAGE  
CHARACTERISTIC PROPERTIES OF ZnO:Al/p-Si HETEROJUNCTION**

**M.Sc. THESIS**

**Yeliz KÖSE  
(506091448)**

**Metallurgical and Materials Engineering Department**

**Materials Engineering Master Program**

**Thesis Advisor: Assoc. Prof. Dr. Murat BAYDOĞAN**

**DECEMBER 2015**



**İSTANBUL TEKNİK ÜNİVERSİTESİ ★ FEN BİLİMLERİ ENSTİTÜSÜ**

**ZnO:Al/p-Si HETEROKAVŞAKLARIN KAPASİTANS-VOLTAJ VE  
AKIM-VOLTAJ KARAKTERİSTİK ÖZELLİKLERİ**

**YÜKSEK LİSANS TEZİ**

**Yeliz KÖSE  
(506091448)**

**Metalurji ve Malzeme Mühendisliği Anabilim Dalı**

**Malzeme Mühendisliği Programı**

**Tez Danışmanı :Doc. Dr. Murat BAYDOĞAN**

**ARALIK 2015**



Yeliz KÖSE, a M.Sc. student of ITU Institute of Science and Technology student ID 506091448 successfully defended the thesis entitled “Capacitance-Voltage and Current-Voltage Characteristic Properties of ZnO:Al/p-Si Heterojunction” which she prepared after fulfilling the requirements specified in the associated legislations, before the jury whose signatures are below.

**Thesis Advisor :**      **Assoc. Prof. Dr. Murat BAYDOĞAN**      .....  
İstanbul Technical University

**Jury Members:**      **Prof. Dr. Hüseyin ÇİMENÖĞLU**      .....  
İstanbul Technical University

**Assoc. Prof. Dr. Erdem ATAR**      .....  
Gebze Technical University

**Date of Submission : 27 September 2015**  
**Date of Defense : 25 December 2015**





*To my husband and family,*



## **FOREWORD**

This master thesis is supported by ITU Institute of Science and Technology and studied under the teaching supervision of Prof. Dr. Hüseyin ÇİMENÖĞLU and Assoc. Prof. Dr. Murat BAYDOĞAN, Department of Metallurgical and Materials Engineering and Prof. Dr. Nilgün BAYDOĞAN, Department of Nuclear Researches.

I would like to express my deep appreciation and thanks to my advisor Assoc. Prof. Dr. Murat BAYDOĞAN for his technical and spiritual guidance and Prof. Dr. Nilgün BAYDOĞAN for her great help during the development of my thesis.

I owe Özge KARACASU a great debt of gratitude for her supportive friendship and for her endless helps.

I am grateful to study with Res. Assist. Onur MEYDANOĞLU, Res. Assist. Faiz MUHAFFEL and all my colleagues as my workmate and as my friends.

At last but not at least thanks to my parents Kürşat KÖSE and Hacer KÖSE for their standing back of me.

December 2015

Yeliz KÖSE  
Metallurgical and Materials Engineer



## TABLE OF CONTENTS

	<u>Page</u>
<b>FOREWORD</b> .....	<b>ix</b>
<b>TABLE OF CONTENTS</b> .....	<b>xi</b>
<b>ABBREVIATIONS</b> .....	<b>xiii</b>
<b>LIST OF SYMBOLS</b> .....	<b>xv</b>
<b>LIST OF TABLES</b> .....	<b>xvii</b>
<b>LIST OF FIGURES</b> .....	<b>xix</b>
<b>SUMMARY</b> .....	<b>xxiii</b>
<b>ÖZET</b> .....	<b>xxv</b>
<b>1. INTRODUCTION</b> .....	<b>1</b>
<b>2. ELECTRICAL PROPERTIES OF SOLID MATERIALS</b> .....	<b>7</b>
2.1 Metals .....	7
2.2 Insulators .....	9
2.3 Semiconductors .....	10
2.3.1 Types of semiconductors .....	11
<b>3. ZINC OXIDE THIN FILMS</b> .....	<b>15</b>
3.1 Properties of Zinc Oxide Thin Films .....	15
3.2 Dopands and Their Effects on ZnO Thin Films .....	17
3.2.1 Al doped zinc oxide thin films .....	18
3.3 Production Techniques of ZnO:Al Thin Films .....	18
<b>4. SOL GEL COATING TECHNIQUE</b> .....	<b>21</b>
4.1 Applications of Sol-Gel Process .....	23
4.2 Deposition Techniques of Sol-Gel .....	24
4.2.1 Spin coating technique .....	24
4.2.2 Roll/gravure coating technique .....	25
4.2.3 Dip coating technique .....	27
<b>5. P-N JUNCTIONS</b> .....	<b>31</b>
5.1 P-N Junctions Diodes .....	31
5.1.1 Bias of P-N junctions .....	34
5.1.1.1 Zero bias or thermal equilibrium .....	34
5.1.1.2 Forward bias .....	35
5.1.1.3 Reverse bias .....	36
5.1.2 I-V Characteristics of P-N junction diode .....	38
5.1.2.1 Effect of temperature on diode characteristics .....	40
5.1.3 C-V Measurement of P-N junction diode .....	41
5.1.4 Properties of ZnO/Si heterojunction .....	44
5.1.4.1 Structural properties of ZnO/Si heterojunctions .....	44
5.1.4.2 Electrical properties of ZnO/Si heterojunctions .....	48
5.1.4.3 Production techniques of ZnO/Si heterojunctions .....	60
<b>6. EXPERIMENTAL PROCEDURE</b> .....	<b>61</b>
6.1 Production Process of ZnO:Al Thin Films and ZnO:Al/p-Si Heterojunctions .....	62

6.1.1 Sol Preparation .....	62
6.1.2 Pre-Treatments of substrates .....	63
6.1.3 Deposition of films.....	64
6.2 Characterization of ZnO:Al Thin Films .....	65
6.2.1 Structural properties .....	65
6.2.2 Electrical properties.....	66
6.3 Characterization of ZnO:Al/Si Heterojunctions .....	66
<b>7. RESULTS AND DISCUSSION.....</b>	<b>71</b>
7.1 Structural Properties of ZnO:Al Thin Films.....	71
7.1.1 Effects of Al concentration .....	71
7.1.2 Effects of annealing temperature.....	74
7.2 Electrical Properties of ZnO:Al Thin Films .....	77
7.2.1 Effects of Al concentration .....	77
7.2.2 Effects of annealing temperature.....	78
7.3 Heterojunction Properties of ZnO:Al/ p-Si .....	81
7.3.1 Effects of Al concentration .....	81
7.3.2 Effects of annealing temperature.....	87
7.4 Capacitance-Voltage (C-V) Properties of ZnO:Al/ p-Si .....	93
<b>8. CONCLUSION.....</b>	<b>97</b>
<b>REFERENCES .....</b>	<b>99</b>
<b>APPENDICES .....</b>	<b>107</b>
<b>CURRICULUM VITAE.....</b>	<b>111</b>

## ABBREVIATIONS

<b>AFM</b>	: Atomic Force Microscopy
<b>AZO</b>	: Aluminium Doped ZnO
<b>BJT</b>	: Bipolar Junction Transistor
<b>CRT</b>	: Cathode Ray Tube
<b>CV</b>	: Capacitance Voltage
<b>CVD</b>	: Chemical Vapor Deposition
<b>DC</b>	: Direct Current
<b>DEA</b>	: Diethanolamine
<b>DTA</b>	: Differential Thermal Analysis
<b>DUT</b>	: Device Under Test
<b>FESEM</b>	: Field Emission Scanning Electron Microscopy
<b>FF</b>	: Fill Factor
<b>FWHM</b>	: Full Width Half Maximum of Distinctive Peak
<b>HBT</b>	: Heterojunction Bipolar Transistor
<b>HEMT</b>	: High-Electron Mobility Transistor
<b>HJ</b>	: Heterojunction
<b>IBS</b>	: Ion-Beam Sputtering
<b>ITO</b>	: Indium Tin Oxide
<b>IR</b>	: Infrared
<b>IV</b>	: Current Voltage
<b>JFET</b>	: junction Field-Effect Transistor
<b>LD</b>	: Laser Diode
<b>LED</b>	: Light Emitting Diode
<b>MEA</b>	: Mono ethanolamine
<b>MEMS</b>	: Microelectromechanical System
<b>MESFET</b>	: Metal-Semiconductor Field-Effect Transistor
<b>MIS</b>	: Metal-Insulator-Semiconductor
<b>MOCVD</b>	: Metal-Organic Chemical Vapor Deposition
<b>MQW</b>	: Multiquantum Well
<b>PL</b>	: Photoluminescence
<b>PLA</b>	: Pulsed Laser Deposition
<b>PV</b>	: Photovoltaic
<b>PVC</b>	: Photovoltaic Cell
<b>RF</b>	: Radio Frequency
<b>RMS</b>	: Rootmean-Square
<b>RPP</b>	: Rapid Photo-thermal Processing
<b>SAW</b>	: Surface Acoustic Wave
<b>SCS</b>	: Semiconductor Characterization System
<b>SCSD</b>	: Successive Chemical Solution Deposition
<b>SEM</b>	: Scanning Electron Microscopy
<b>SL</b>	: Superlattice
<b>SPT</b>	: Spray Pyrolysis

<b>TCO</b>	: Transparent Conducting Oxide
<b>TEOS</b>	: Tetraethoxysilane
<b>TGA</b>	: Thermo Gravimetric Analysis
<b>TMOS</b>	: Tetramethoxysilane
<b>UV</b>	: Ultraviolet
<b>VIS</b>	: Visible Range
<b>XRD</b>	: X- Ray Diffraction



## LIST OF SYMBOLS

$\lambda$	: Wavelength
$\theta$	: Wetting Angle
$\theta_\beta$	: Bragg Diffraction Angle
$B$	: Material Constant
$\beta$	: FWHM (Full width half maximum of distinctive peak) of $\theta_\beta$
$C$	: Capacitance
$V$	: Applied Voltage Through the Diode
$V_{bi}$	: Built-in-potential
$V_r$	: Threshold Voltage
$V_{d0}$	: Diffusion Voltage Zero Bias
$V_T$	: Thermal Voltage
$V_{oc}$	: Open Circuit Voltage
$I$	: Net Current Flowing Through the Diode
$I_0$	: Saturation Current
$I_F$	: Forward Current
$I_R$	: Reverse Current
$I_{sc}$	: Short-circuit Current
$q$	: Absolute Value of Electron Charge
$k_B$	: Boltzmann's Constant
$n$	: Ideality factor
$\eta$	: Liquid Viscosity
$\eta_P$	: Conversion Efficiency
$\rho$	: Resistivity
$\rho$	: Liquid Density
$U_0$	: Withdrawal Speed
$P$	: Capillary Pressure
$P_W$	: Working Gas Pressure
$\gamma$	: Liquid-vapor Surface Tension
$\gamma_{LV}$	: Surface Tension
$\delta$	: Boundary Layer
$h$	: Coating Thickness
$g$	: Gravity
$T$	: Absolute Temperature
$T_{sub}$	: Substrate Temperature
$E_g$	: Band-gap Energy
$N_A$	: Acceptor Density in p-Si
$N_c$	: The Effective Density of States in The Conduction Band of The Semiconductor
$N_D$	: Donor Density in n-ZnO
$\epsilon$	: Dielectric Constant
$\epsilon_s$	: Semiconductor Permittivity
$J_0(T)$	: Reverse Saturation Current Density

**$J_{sc}$**  : Shortcircuit Current Density  
 **$FF$**  : Fill Factor  
 **$\chi$**  : Electron Affinity

## LIST OF TABLES

	<u>Page</u>
<b>Table 2.1 :</b> Classification of solid materials according to resistivity .....	7
<b>Table 5.1 :</b> Built-in potential, donor concentration and barrier heights for ZnO films grown at different substrate temperatures. ....	43
<b>Table 5.2 :</b> Characteristic parameters of p-n junction. ....	58
<b>Table 7.1 :</b> $I_0$ , $n$ and $I_F/I_R$ values of ZnO:Al/p-Si heterojunctions for 0.8% at. and 1.2 % at. Al concentrations... ..	83
<b>Table 7.2 :</b> Measured current at -3V under dark and light for heterojunctions for 0.8% at. and 1.2 % at. Al concentrations.. ....	85
<b>Table 7.3 :</b> Measured $V_{OC}$ , $I_{SC}$ , $V_{MP}$ , $I_{MP}$ and FF values for heterojunctions under light for 0.8% at. and 1.2% at. Al concentrations. ....	85
<b>Table 7.4 :</b> $I_0$ , $n$ and $I_F/I_R$ values for ZnO:Al/ p-Si heterojunctions annealed at 700°C and 800°C.....	89
<b>Table 7.5 :</b> Measured current values at -3V under dark and light for heterojunctions annealed at 700°C and 800°C.....	91
<b>Table 7.6 :</b> Measured $V_{OC}$ , $I_{SC}$ , $V_{MP}$ , $I_{MP}$ and FF values of heterojunctions under light for annealed at 700°C and 800°C... ..	91
<b>Table 7.7 :</b> Built-in potential, donor concentration and barrier heights for ZnO films grown at different substrate temperatures .....	95



## LIST OF FIGURES

	<u>Page</u>
<b>Figure 2.1</b> : Schematic energy band representation of a metal; a) Partially filled conduction band (e.g. Cu), b) Overlapping bands (e.g. Zn or Pb).....	8
<b>Figure 2.2</b> : Schematic energy band representation of an insulator .....	9
<b>Figure 2.3</b> : Schematic energy band representation of a semiconductor. ....	10
<b>Figure 2.4</b> : The diamond lattice of silicon and germanium. ....	12
<b>Figure 2.5</b> : Schematic energy band representation of n-type extrinsic semiconductor. ....	12
<b>Figure 2.6</b> : Schematic energy band representation of p-type extrinsic semiconductor. ....	13
<b>Figure 2.7</b> : The lattice of n-type silicon. ....	13
<b>Figure 2.8</b> : The lattice of p-type silicon. ....	13
<b>Figure 3.1</b> : Stick and ball representation of ZnO crystal structures: a) cubic rocksalt (B1), b) cubic zinc blende (B3) and c) hexagonal wurzite (B4). Shaded gray and black spheres denote Zn and O atoms, respectively ...	16
<b>Figure 4.1</b> : Schematic illustration of the main processing steps involved in the formation of transparent coatings containing oxide nanoparticles ...	21
<b>Figure 4.2</b> : Colloidal network formation in sol-gel materials.....	22
<b>Figure 4.3</b> : Sol-Gel routes for glass formation .....	22
<b>Figure 4.4</b> : Stages of coating process via sol-gel process .....	24
<b>Figure 4.5</b> : The four stages of spin coating.....	25
<b>Figure 4.6</b> : Gravure coating evolved from the printing industry .....	26
<b>Figure 4.7</b> : a) Schematic of the steady-state dip-coating process, showing the sequential stages of structural development that result from draining accompanied by solvent evaporation and continued condensation reactions, $U_0$ is the withdrawal speed, $h(x)$ is the film thickness at position $x$ measured from the drying line $\lambda_0$ , $h_0$ is the entrained film thickness just above the stagnation point $S$ , $\eta$ is the liquid viscosity, $\rho$ is the liquid density, $P$ is the capillary pressure, $\gamma_{LV}$ is the surface tension, and $\theta$ is the wetting angle. b) Detail of the flow patterns (streamlines) during dip coating. $\delta$ is the boundary layer, and $h$ is the thickness of the fluid film .....	28
<b>Figure 4.8</b> : Schematic drawing of dip coating process .....	29
<b>Figure 5.1</b> : Diffusion establishes ‘built-in’ electric field.....	32
<b>Figure 5.2</b> : Motion of mobile electrons and holes due to diffusion and the ‘built-in’ electric field.....	33
<b>Figure 5.3</b> : Depletion region .....	33
<b>Figure 5.4</b> : Zero bias of the p-n junction .....	35
<b>Figure 5.5</b> : Forward characteristics curve for a junction diode ...	35
<b>Figure 5.6</b> : Reduction in the depletion layer due to forward bias.....	36
<b>Figure 5.7</b> : Increase in the depletion layer due to reverse bias .....	37

<b>Figure 5.8 :</b> Reverse characteristics curve for a junction diode ...	37
<b>Figure 5.9 :</b> Forward current–voltage characteristics of various types of diodes: a) germanium diode, b) silicon diode, c) Schottky diode, d) tunnel diode, e) backward diode, and f) LED diode.....	38
<b>Figure 5.10 :</b> Electrical (I-V) characteristics of ideal diodes .....	38
<b>Figure 5.11 :</b> Effect of temperature on forward characteristics .....	40
<b>Figure 5.12 :</b> Effect of temperature on avalanche diodes.....	41
<b>Figure 5.13 :</b> $1/C^2$ vs. V bias for ZnO films grown at different substrate temperatures .....	43
<b>Figure 5.14 :</b> The XRD pattern of ZnO films with Al doping concentration of a) as-grown pure ZnO films, b) pure ZnO films after RPP at 650 °C, c) 1 at% Al ZnO films as- grown, d) 1 at% Al ZnO films after RPP at 650 °C, and e) 2 at% Al ZnO films after RPP at 650 °C .....	45
<b>Figure 5.15 :</b> Secondary electron micrographs of undoped and doped ZnO films onto glass substrates showing the influence of doping and RPP annealing on surface morphology: a) undoped as-grown film, b) as-grown 1 at % Al-doped ZnO, c) 4 at % Al-doped ZnO after the RPP 650 °C, 20s, and d) 6 at % Al- doped ZnO. The scale bar is 10 nm.....	46
<b>Figure 5.16 :</b> Scanning electron micrographs of ZnO:Al thin films at different deposition temperatures .....	47
<b>Figure 5.17 :</b> AFM images of ZnO:Al films at different deposition temperatures...	48
<b>Figure 5.18 :</b> I-V curve of the ZnO:Al/p-Si heterojunction device under dark.....	48
<b>Figure 5.19 :</b> Logarithmic scale in current with forward bias condition .....	49
<b>Figure 5.20 :</b> I-V characteristic of the ZnO:Al/p-Si heterojunction under dark and under light (light 1 6.3mW/cm <sup>2</sup> white light; light 2: 20W halogen lamp) .....	50
<b>Figure 5.21 :</b> Current-voltage characteristics of the nc-ZnO/p-Si heterojunctions at various temperatures in dark. The current is plotted as a function of the applied voltage using a linear a) and b) semilogarithmic scale ..	52
<b>Figure 5.22 :</b> Measured current-voltage characteristics of a ZnO:Al/n-Si heterojunction sample .....	53
<b>Figure 5.23 :</b> Measured dark I-V characteristics (forward bias) of a ZnO:Al/n-Si heterojunction sample for temperatures in the range 283-363 K .....	54
<b>Figure 5.24 :</b> J-V curve of the heterojunction under dark and under AM1.5G (100 mW/cm <sup>2</sup> ) simulated sunlight. The inset shows the I-V curve of the heterojunction under dark and under AM1.5G (100 mW/cm <sup>2</sup> ) simulated sunlight .....	55
<b>Figure 5.25 :</b> Band diagrams of the n-ZnO/p-Si heterojunction under dark a) and under solar illumination b).....	56
<b>Figure 5.26 :</b> C-V characteristics in the reverse bias region at 300K for the n-ZnO:Al/p-Si and n-ZnO/p-Si heterojunctions at 1MHz .....	57
<b>Figure 5.27 :</b> C <sup>-2</sup> -Vbias relationship for the n-ZnO:Al/p-Si and n-ZnO/p-Si heterojunctions at .....	57
<b>Figure 5.28 :</b> Band diagram for the n-ZnO/p-Si and the n-ZnO/n-Si.....	58
<b>Figure 5.29 :</b> $1/C^2$ versus voltage plot of an nc-ZnO/c-Si heterojunction measured at 1 MHz in dark ...	59
<b>Figure 6.1 :</b> Flow chart of the preparation of the coating sol and coating procedure for ZnO:Al multilayer coatings.....	61
<b>Figure 6.2 :</b> a) Nüve OT 012 Bench Top Steam Sterilizer b) Binder ED 53 etuve.	62

<b>Figure 6.3</b>	: TG/DT Analyses of dried ZnO:Al gel with 10°C/min heating and cooling rate .....	63
<b>Figure 6.4</b>	: Bondelin Sonorex Ultrasonic Bath.....	64
<b>Figure 6.5</b>	: KSV Dip coater LMX2 equipment.....	64
<b>Figure 6.6</b>	: GBC-MMA X-Ray diffractometer .....	65
<b>Figure 6.7</b>	: JEOL 6335F Scanning Electron Microscope .....	66
<b>Figure 6.8</b>	: a) and b) Veeco Dektak- 6M surface profilometer.....	66
<b>Figure 6.9</b>	: Rusonic Cold Gas Dynamic Spray equipment .....	67
<b>Figure 6.10</b>	: Schematic diagram of ZnO:Al/Si heterojunction .....	67
<b>Figure 6.11</b>	: a) Bandgap structure of the novel ZnO:Al /p-Si heterojunction b) Optical band gaps of ZnO:Al thin films at 0.8 and 1.6 at % Al concentrations for unirradiated and their radiated states.....	68
<b>Figure 6.12</b>	: a) Keithley 4200 Semiconductor characterization system (SCS) b) LOT-Oriel 100/150 W Hg/Hg(Xe) Light Source .....	68
<b>Figure 6.13</b>	: Hewlett Packard 4192A Impedance Analyzer .....	69
<b>Figure 7.1</b>	: a) X-Ray diffraction patterns of ZnO:Al thin films depends on Al concentration annealed at 700°C in vacuum b) 2 $\theta$ value of the samples at different doping concentrations. ....	72
<b>Figure 7.2</b>	: Average crystallite sizes of ZnO:Al thin films oriented in (101) depends on Al concentration annealed at 700°C in vacuum.. ....	73
<b>Figure 7.3</b>	: X-ray diffraction patterns of 1.2 at. % Al doped ZnO:Al thin films annealed in air depends on annealing temperature .....	74
<b>Figure 7.4</b>	: Average Crystallite Size 1.2 at. % Al doped ZnO:Al thin films oriented in (101) annealed in air as a function of annealing temperature .....	75
<b>Figure 7.5</b>	: SEM images of 1.2 at. % Al doped ZnO:Al thin films annealed in air at a) 550°C b) 600°C c) 700°C d) 800°C (20.000X and 30.000X) .....	75
<b>Figure 7.6</b>	: Variation of ZnO:Al thin film thickness as a function of annealing temperature for 1.2 at.% Al .....	77
<b>Figure 7.7</b>	: Variation of resistivity as a function of dopant concentration for Al doped ZnO thin films annealed at 700°C under vacuum .....	78
<b>Figure 7.8</b>	: Variation of resistivity as a function of dopant concentration for Al doped ZnO thin films annealed at different temperatures under vacuum.....	79
<b>Figure 7.9</b>	: Variation of resistivity as a function of annealing temperature for 1.2 at. % Al doped ZnO thin films annealed under vacuum .....	80
<b>Figure 7.10</b>	: Variation of resistivity as a function of annealing temperature for 1.2 at % Al doped ZnO thin films annealed in air .....	80
<b>Figure 7.11</b>	: Current-voltage characteristics of ZnO:Al/p-Si heterojunctions under dark condition for different Al concentrations annealed at 700°C under vacuum .....	82
<b>Figure 7.12</b>	: Semilog I-V characteristics of ZnO:Al/p-Si heterojunctions under dark condition for 0.8 % at. and 1.2 % at. Al concentrations annealed at 700°C under vacuum .....	82
<b>Figure 7.13</b>	: I-V characteristic of ZnO:Al/p-Si heterojunction annealed under vacuum at 700°C in dark and in light for a) 0.8 % at. and b) 1.2 % at. Al concentrations. ....	84

<b>Figure 7.14</b> : Measured current density- voltage characteristics of ZnO:Al/p-Si heterojunctions for different Al concentrations annealed at 700°C under vacuum for a) 0.8 % at. % b) 1.2 % at.....	86
<b>Figure 7.15</b> : Cross-section SEM image of the Cu/ZnO:Al/p-Si/Al heterojunction films, annealed at b) 500°C and b)700 °C.....	87
<b>Figure 7.16</b> : Measured current density-voltage characteristics of ZnO:Al/p-Si heterojunctions for 1.2 % at. Al concentration under dark condition, annealed under vacuum at different annealing temperatures.....	88
<b>Figure 7.17</b> : Semilog I-V characterictics of ZnO:Al/p-Si heterojunctions under dark with 1.2.% at Al annealed at 700°C and 800 °C under vacuum. ..	89
<b>Figure 7.18</b> : Measured current-voltage characteristics of ZnO:Al/p-Si Heterojunctions with 1.2 % at. Al dop concentration under dark and light, annealed under vacuum at a) 700 °C and b) 800 °C.....	90
<b>Figure 7.19</b> : Measured current density-voltage characteristics of ZnO:Al/p-Si heterojunctions for 1.2 % at. Al concentration, annealed under vacuum at different annealing temperatures a) 700°C and b)800°C.....	92
<b>Figure 7.20</b> : C-V characteristics in the reverse bias region at a) 700°C and b) 800°C for n-ZnO:Al/p-Si heterojunctions at 1MHz.....	93
<b>Figure 7.21</b> : $C^{-2}$ -V characteristics for the n-ZnO:Al/p-Si heterojunctions at 1MHz for at a) 700°C and b) 800°C.....	94



## **CAPACITANCE-VOLTAGE AND CURRENT-VOLTAGE CHARACTERISTIC PROPERTIES OF ZnO:Al/p-Si HETEROJUNCTION**

### **SUMMARY**

In the modern world, finding new alternative energy sources is a vital issue for many reasons. One reason is that traditional energy sources like coal, gas, and oil are not renewable sources and they will eventually be depleted. Another important reason is that burning of fossil fuels cause air and water contamination. Additionally, one of the most important another reason is that the electricity generated from fossil fuels has led to high concentrations of harmful gases like carbon monoxide, carbon dioxide, etc. in the atmosphere, which increase the average temperature on the planet, which is known as the global warming.

Clean and renewable energy sources like solar energy, wind energy and hydrogen fuel energy can be considered as an alternative. This kind of energy resources cause fewer emissions, reduce pollution and stand out as a viable source of clean and limitless energy. In this study, we will focus on the solar energy as one of the most promising sources of alternative energy.

Among renewable energy, solar energy is the most abundant one that can supply the energy needed by the world's population. It has also an advantage for isolated places to where they are away from the grid. Electricity from sun has no damage to environment since there is no toxicity and waste products. It can be categorized as the cleanest and most abundant source of energy

Transparent conducting oxide (TCO) films have much interest in recent years. The optical and electrical properties of the films have been improved over the years. TCO's have been widely used in various industry areas such as optoelectronics, display industry, solar cells, with their desirable optical and electrical properties. In<sub>2</sub>O<sub>3</sub>, SnO<sub>2</sub> and ZnO are metal oxides that widely used as transparent conductive oxide (TCO) materials

ZnO has received much attention over the past few years because it has a wide range of properties that depend on doping, including a range of conductivity from metallic to insulating (including n-type and p-type conductivity), high transparency, high piezoelectricity, wide-bandgap semiconductivity, room-temperature ferromagnetism, huge magneto-optic and chemical-sensing effects, non-toxicity, high resistivity control, high chemical, mechanical and thermal stability together with its abundance in nature which makes it a lower cost material. These characteristics have made ZnO thin films very attractive for promising applications in solar cells, gas sensors, transducers, luminescent materials, transparent conductors, heat mirrors and semiconductor heterojunctions.

Un-doped ZnO films which have poor electrical properties due to the low carrier concentration, showed high conductivity due to defects like oxygen vacancies and Zn

interstitial. Its electrical properties are significantly affected by adsorption of O<sub>2</sub>, CO<sub>2</sub>, hydrocarbons, S-containing compounds, and water.

Doping of ZnO with aluminum (ZnO:Al) can increase film conductivity. Aluminum-doped zinc oxide (ZnO:Al) has attracted much attention because of its low cost, good optical and electronic properties, heat stability, non-toxicity and high transparency in the near-infrared (IR) and invisible regions (90 %)

ZnO films have been used as solar cell electrodes, gas sensors and optical devices. For fabrication of ZnO films various techniques have been used such as sputtering, chemical vapor deposition, spray pyrolysis, sol-gel etc.

Among these, the sol-gel process presents an easy way to integrate ZnO devices into the Si technology, since it offers the possibility of excellent compositional control, multicomponent oxide layers of many compositions on substrate, simplicity, homogeneity, lower crystallization temperature and low production costs. Sol-gel process can be used to fabricate almost any single or multi-component oxide coating. Such coatings have been deposited on glass to provide coloration, anti-reflection, selective reflection, electrochromism and photochromism, selective absorption, wave guiding, reduced friction, anti-soiling reduced adhesion, transparent conductors, electro-optics, Ferro-electrics, sensors, and dye lasers.

Deposition of ZnO films on p/n type substrates provides to produce heterojunction which are generally used for fabrication of solar cells. Recently n-ZnO/p-Si heterojunctions has received much attention for electronical applications. The biggest advantage of these heterojunctions is to combine the large binding energy of ZnO thin films and the inexpensiveness of Si substrates.

In this work Al doped n-ZnO/p-Si heterojunctions were fabricated by sol-gel dip coating process. P type Si (100) wafers and glasses were used as the substrates. The structural and electrical properties of ZnO:Al thin films and heterojunction properties of ZnO:Al/p-Si were investigated with respect to effects of Al doping concentration and process parameters (i.e. thermal treatment temperature and ambient). After the coating process, characterization of the ZnO:Al thin films and ZnO:Al/p-Si heterojunctions were made by X-Ray diffractometer, scanning electron microscopy, surface profilometer, dispensible four point resistivity probe and a semiconductor characterization system (SCS).

Structural properties investigation by X-ray diffraction method showed that the films were in the form of hexagonal wurzite and tetragonal structure. The XRD patterns of the ZnO:Al films on p type si substrate had (100), (002) and (101) diffraction peaks were in accordance with literature. SEM images show that ZnO:Al films had granular nanostructure. The increasing of the thermal treatment temperature caused an increase on crystalline size. The annealing ambient tended to change the crystalline size of the thin films. The thicknesses of the thin films are in the range of 150-500 nm and the certain decrease was detected while the annealing temperature was increased.

Electrical resistivity changed with respect to Al doping concentration, annealing ambient and temperature. Minimum resistivity were detected at 1.2 at.% Al concentration.

ZnO:Al/p-Si heterojunction properties were analysed by current-voltage (I-V) measurements and capacitance-voltage (C-V) depend on the Al dopand concentrations and annealing temperatures. Most of the ZnO:Al/p-Si heterojunctions

exhibited diode-like rectifying behavior. Under UV illumination the photoelectric behavior observed for the diodes. In this study the 1.2 at.% Al doping concentration, vacuum ambient and 700°C annealing temperature are the optimum process parameters to produce heterojunction.



## **ZnO:Al/p-Si HETEROKAVŞAKLARIN KAPASİTANS-VOLTAJ VE AKIM-VOLTAJ KARAKTERİSTİK ÖZELLİKLERİ**

### **ÖZET**

Modern dünyada yeni alternatif enerji kaynakları bulmak birçok nedenden dolayı hayati bir konudur. Nedenlerinden biri kömür, gaz, petrol ve benzeri geleneksel enerji kaynaklarının yenilenebilir kaynaklar olmaması ve sonunda tükenecek olmasıdır. Bir başka önemli nedeni de fosil yakıtların yanması sonunda hava ve su kirlenmesine neden olmasıdır. Ayrıca, en önemli nedenlerinden birisi de fosil yakıtlardan elektrik üretimi sırasında atmosferdeki karbonmonoksit, karbondioksit gibi dünyanın ortalama sıcaklığını artırıcı özellik yani küresel ısınmaya neden olan zararlı gazların konsantrasyonunda artışa sebep olmasıdır.

Güneş enerjisi, rüzgar enerjisi ve hidrojen yakıt enerjisi gibi temiz ve yenilenebilir enerji kaynakları alternatif olarak kabul edilebilir. Bu tür enerji kaynakları daha az emisyonu ve kirliliğe sebep olurken, temiz ve sınırsız enerji kaynağı olarak uygulanabilirliği mevcuttur. Bu çalışmada alternatif enerjinin en umut verici kaynağı olarak görülen güneş enerjisi üzerinde durulacaktır.

Yenilenebilir enerji sistemleri arasında güneş enerjisi, dünya nüfusunun ihtiyaç duyduğu enerjiyi temin edebilecek enerji bolluğuna sahiptir. Avantajlarından biri kablo şebekesinden yeterince uzak izolasyon yerlerinin olmasıdır. Güneşten elektrik üretiminde toksisite ve atık ürünleri olmadığından çevreye zararı yoktur. Güneş enerjisi en temiz ve en bol yenilenebilir enerji sistemi olarak katagorize edilebilir.

Geçirgen iletken oksit filimler son yıllarda çok ilgi görmektedir. Bu filmlerin optik ve elektriksel özellikleri yıllar geçtikçe geliştirilmektedir. Geçirgen iletken oksitler cazip optik ve elektriksel özellikleriyle optoelektronik, görüntüleme güneş pilleri gibi birçok endüstri alanında yaygın olarak kullanılmaktadır.  $\text{In}_2\text{O}_3$ ,  $\text{SnO}_2$  ve  $\text{ZnO}$  gibi metal oksitler geçirgen iletken oksit malzemeler olarak yaygın kullanılırlar.

$\text{ZnO}$  son yıllarda çok ilgi duyulan bir malzemedir. Katkı maddasına bağlı olarak geniş özelliklere sahiptir. Bunlar metallere yarıtkanlara (n-tipi ve p-tipi yarıiletkenleride içeren) kadar geniş iletkenlik özelliği, yüksek geçirgenlik, yüksek piezoelektrik özelliği, geniş bant aralıklı yarıiletkenlik, oda şartlarında ferromanyetizma özelliği, yüksek manyetooptik ve kimyasal kararlılık, toksik olmama, yüksek direnç kontrolü, yüksek kimyasal-mekanik ve termal kararlılık, doğada çok bulunması ve ucuz olmasıdır.  $\text{ZnO}$  ince filmlerin bu özellikleri sayesinde güneş pillerinde, gaz sensörlerinde, dönüştürücülerde, parlak malzemelerde, geçirgen iletkenlerde, ısı aynalarda ve yarıiletken heterokavşak uygulamalarında kullanımı oldukça artmıştır.

Katkısız  $\text{ZnO}$  filmleri oksijen boşlukları ve  $\text{Zn}$  arayer atomları gibi hatalarından dolayı yüksek öziletkenlik, düşük taşıyıcı konsantrasyonundan dolayı zayıf elektriksel özelliklere sahiptir. Elektriksel özellikleri oksijen absorpsiyonundan,

karbondioksitten, hidrokarbondan, kükürt katkılı bileşiklerden ve sudan oldukça etkilenmektedir.

Çinko oksitin Alüminyum ile katkılanması (ZnO:Al) iletkenliği artırabilir. Alüminyum katkılı çinko oksit filmlerine (ZnO:Al) düşük maliyet, yüksek optik ve elektrik özellikleri, ısıl kararlılık, toksik olmama, görünür ve kızıl ötesi bölgesinde yüksek geçirgenlik (%90) özelliklerinden dolayı oldukça ilgi duyulmaktadır.

Çinko oksit filmler güneş pili elektrotu, gaz sensörü ve optik cihaz olarak kullanılmaktadır. ZnO filmlerin üretimi için sıçratma, kimyasal buhar biriktirme, spreylendirme, sol-gel vb. birçok çeşitli teknik kullanılmaktadır.

Bunların arasında sol-jel prosesi Si teknolojisinde ZnO araçlarının entegre edilmesinde en kolay yöntem olarak görülmektedir. Çünkü mükemmel kompozisyon kontrolü, yüzey üstüne çok bileşenli oksit tabakalaştırma, basitlik, homojenlik, düşük kristalleşme sıcaklığı ve düşük üretim maliyetine sahiptir. Sol-jel prosesi tek yada çok bileşenli oksit kaplama üretiminde kullanılabilir. Bu tür kaplamalar renklendirme, yansıma önleyici, seçici yansıma, elektrokromizm ve fotokromizm, kirlenme azaltıcı, geçirgen iletken, elektro-optik, ferro-elektrik, sensör ve boya lazer sağlamak için cam üzerine kaplanmaktadır.

Al katkılı ZnO filmler p ve n tip altlıklara genellikle güneş pilleri yapımında kullanılan heterokavşakların üretimi için biriktirilmiştir. Son zamanlarda n-ZnO/p-Si heterokavşaklar elektronik uygulamalar için dikkat çekmektedir. Bu heterokavşakların en büyük avantajı geniş bağlanma enerjisi olan ZnO ince filmlerle silikon altlığın ekonomikliğini bir araya getirmesidir.

Bu çalışmada Al katkılı n-ZnO/p-Si heterokavşaklar sol-gel daldırma prosesi ile üretilmiştir. P tip Si (100) waferlar ve camlar altlık olarak kullanılmıştır. ZnO:Al ince filmlerin yapısal ve elektriksel özellikleri ve ZnO:Al/p-Si yapılarının heterokavşak özellikleri Al katkı konsantrasyonuna ve üretim parametrelerine (ısıl işlem sıcaklığı ve ortamın gibi) göre incelenmiştir. Kaplama işleminden sonra, ZnO:Al ince filmlerin ve ZnO:Al/p-Si heterokavşakların karakterizasyonları, X ışınları kırınımı, taramalı elektron mikroskobu, yüzey profilometresi, dört ayaklı iletkenlik probu ve yarı iletken karakterizasyon sistemi ile yapılmıştır.

Yapısal özellikler X-ışını kırınımı yöntemiyle incelendiğinde filmlerin hexagonal wurzite ve tetragonal yapıda olduğu gözlenmiştir. XRD desenlerinde filmlerin literatürde uygun olarak (100), (002) ve (101) kırınım piki verdiği gözlenmiştir. SEM görüntüleri ZnO:Al filmlerin granüler nano-yapıda olduğunu göstermiştir. Tavlama sıcaklığının artışı kristal boyutunda artışa sebep olmaktadır. Tavlama ortamı kristal boyutunu değiştirme eğilimindedir. Filmlerin kalınlığı 150-500 nm. aralığındadır ve sıcaklık artışıyla belirgin derecede düşmektedir.

Elektriksel öz direnç değişimi Al katkı konsantrasyonu, tavlama ortamı ve sıcaklığına bağlı olarak incelenmiştir. Minimum öz direnç değerleri %1.2 atomik katkı miktarında saptanmıştır.

Heterokavşak özellikleri Al katkı konsantrasyonu ve tavlama sıcaklığına bağlı olarak akım-voltaj (I-V) ve kapasitans-voltaj (C-V) ölçümleri ile analiz edilmiştir. Çoğu ZnO:Al/Si heterokavşaklar diyot tipi doğrultucu özellik göstermiştir. UV aydınlanma altında diyotlarda fotoelektrik özellik gözlemlenmiştir. Bu çalışmada heterokavşak üretmek için 1.2 at.% Al katkı konsantrasyonu, vakum ortamı ve 700°C tavlama sıcaklığı optimum işlem parametreleridir.

## 1. INTRODUCTION

In the modern world, finding new alternative energy sources is a vital issue for many reasons. One reason is that traditional energy sources like coal, gas, and oil are not renewable sources and they will eventually be depleted. Another important reason is that burning of fossil fuels cause air and water contamination. Additionally, one of the most important another reason is that the electricity generated from fossil fuels has led to high concentrations of harmful gases like carbon monoxide, carbon dioxide, etc. in the atmosphere, which increase the average temperature on the planet, which is known as the global warming.

Clean and renewable energy sources like solar energy, wind energy and hydrogen fuel energy can be considered as an alternative. This kind of energy resources cause fewer emissions, reduce pollution and stand out as a viable source of clean and limitless energy. In this study, we will focus on the solar energy as one of the most promising sources of alternative energy [1].

Among renewable energy, solar energy is the most abundant one that can supply the energy needed by the world's population. It has also an advantage for isolated places to where they are away from the grid. Electricity from sun has no damage to environment since there is no toxicity and waste products. It can be categorized as the cleanest and most abundant source of energy [2].

Photovoltaic energy conversion is one of the major technologies of solar energy conversion. The history of the photovoltaic technologies started with the discovery of photogalvanic effect by Becquerel in 1839. Russel Ohl owned the first patented modern semiconductor solar cells in 1946 [3]. The highly efficient solar cell was first developed by Daryl Chapin, Calvin Souther Fuller and Gerald Pearson in 1954 using a diffused silicon p-n junction [4].

Monocrystalline and polycrystalline solar cells are historically first solar cells developed in 1960s. They are usually considered as the first generation solar cell. In spite of their relatively high cost, these types of solar cells, as the most mature and reliable technology, dominates the solar cell market today.

The crystalline Si solar cells stems from the fact that the material and device has reached very high quality because of extensive research efforts carried out in the last 50 years. In addition, the active part of the device, i.e., the p-n junction, is formed by deriving the doping front into the pure crystalline substrate. This makes the the p-n junction free from any contamination that might naturally exists at artificially formed interfaces. The major disadvantage of the crystalline cells is the high cost due to the extensive material usage. Module efficiencies about 19% have been reached with monocrystalline silicon solar cell [2]. However, for the polycrystalline silicon, the module efficiency about 17% has been achieved. Different cell and contact designs are still under investigation to push the efficiency to higher values.

One uses the solar energy in converting this energy into (a) heat, and (b) electricity. In the first case, it is used for directly heating homes or for water heating where the sun's rays are incident on a panel containing circulating water in tubes. In the second case, it is used for generating electricity using photovoltaic panels [5].

Transparent conducting oxides (TCOs) are electrical conductive materials with a comparably low absorption of light. They are usually prepared with thin film technologies and used in opto-electrical devices such as solar cells, displays, opto-electrical interfaces and circuitries. Glass fibers are nearly less conductors of light, but electrical insulators; silicon and compound semiconductors are wavelength dependent optical resistors (generating mobile electrons), but dopant dependent electrical conductors. Transparent conducting oxides are highly flexible intermediate states with both these characteristics. Their conductivity can be tuned from insulating via semiconducting to conducting as well as their transparency adjusted. As they can be produced as n-type and p-type conductives, they open a wide range of power saving opto-electrical circuitries and technological applications.  $\text{In}_2\text{O}_3$ ,  $\text{SnO}_2$  and  $\text{ZnO}$  are metal oxides that widely used as transparent conductive oxide (TCO) materials [6].

$\text{ZnO}$  has received much attention over the past few years because it has a wide range of properties that depend on doping, including a range of conductivity from metallic to insulating (including n-type and p-type conductivity), high transparency, high piezoelectricity, wide-bandgap semiconductivity, room-temperature ferromagnetism, huge magneto-optic and chemical-sensing effects, non-toxicity, high resistivity control, high chemical, mechanical and thermal stability together with its abundance



in nature which makes it a lower cost material [7]. These characteristics have made ZnO thin films very attractive for promising applications in solar cells, gas sensors, transducers, luminescent materials, transparent conductors, heat mirrors and semiconductor heterojunctions [8].

ZnO is an n-type II-VI semiconductor. ZnO has numerous attractive characteristics for electronics and optoelectronics devices. It has direct bandgap energy of 3.37 eV, which makes it transparent in visible light and operates in the UV to blue wavelengths. The exciton binding energy ~60meV for ZnO, as compared to GaN ~25 meV; the higher exciton binding energy enhances the luminescence efficiency of light emission [9]. ZnO can be grown on inexpensive substrate, such as glass, at relatively low temperatures [10].

Un-doped ZnO films which have poor electrical properties due to the low carrier concentration [11], showed high conductivity due to defects like oxygen vacancies and Zn interstitial. Its electrical properties are significantly affected by adsorption of O<sub>2</sub>, CO<sub>2</sub>, hydrocarbons, S-containing compounds, and water [12]. Doped ZnO thin films have better surface smoothness than un-doped ZnO thin films regardless of doping elements [11].

Single crystals and polycrystalline films of zinc oxide have been doped to enhance their mechanical, electrical, and optical properties with elements of the alkali metals such as Li, Ga, In, N, Al, Sn, and P from groups IIIB to VIIB [13]. However, Doping ZnO with appropriate impurities, from III group elements such as Al, Ga, and In determined to be the most suitable elements [14].

In the last decade, Aluminum is commonly used as dopants for ZnO by replacing Zn<sup>+2</sup> ions with Al<sup>+3</sup> and showed photoluminescence in the ultraviolet (UV) and visible spectral range because of its optical properties and excitonic emission at room temperature. Aluminum-doped zinc oxide (ZnO:Al) has attracted much attention because of its low cost, good optical and electronic properties, heat stability, non-toxicity and high transparency in the near-infrared (IR) and invisible regions (90 %) [15].

The more pronounced electrical and optical changes were observed when the doping concentration of Al is 1.2 at. %. High transmittance in the visible range was achieved with 1.2 at. % of aluminum doped ZnO [16]. ZnO:Al thin films with high c-axis

orientated crystalline structure along (002) plane can reduce the electrical resistivity due to an increase in carriers mobility by reducing the probability of the scattering of the carriers at the grain boundary [17].

The properties of ZnO thin films are much influenced by not only the growth methods but also the heat treatment parameters, especially the thermal annealing. Therefore, it is essential to investigate the effect of annealing process on the microstructure, transparent properties, and morphology of ZnO films [18]. The film exhibited a resistivity of  $7.5 \times 10^{-4} \Omega\text{-cm}$  and an optical transmittance over 85% in the visible spectral region [19].

ZnO thin films have been prepared by employing various processes such as thermal evaporation, chemical vapor deposition (CVD), pulsed laser deposition (PLA), spray pyrolysis (SPT), sol-gel, RF magnetron sputtering, ion-beam sputtering (IBS) [20], metal organic chemical vapor deposition (MOCVD), ion-assisted deposition and reactive evaporation etc. [21]. In several studies, it was shown that the optical and electrical properties of AZO thin films could be obviously improved by optimizing deposition conditions and doping [22].

Among these, the sol-gel process presents an easy way to integrate ZnO devices into the Si technology, since it offers the possibility of excellent compositional control, multicomponent oxide layers of many compositions on substrate, simplicity, homogeneity, lower crystallization temperature and low production costs [23]. This technique offers the possibility of preparing a small as well as large-area coating of ZnO thin films at low cost for technological applications. However, the sol-gel method is difficult to obtain high preferential c-axis orientation films due to its film growth procedure [17]. The ZnO thin films prepared by sol-gel technique show high optical transmittance (85-90%) in the near UV, VIS and IR regions [24].

Sol-gel process can be used to fabricate almost any single or multi-component oxide coating. Such coatings have been deposited on glass to provide coloration, anti-reflection, selective reflection, electrochromism and photochromism, selective absorption, wave guiding, reduced friction, anti-soiling reduced adhesion, transparent conductors, electro-optics, Ferro-electrics, sensors, and dye lasers [25].

The main factors affecting the sol-gel film microstructure and properties are: solution chemical equilibrium (chemical composition, concentration, pH, order-time-

temperature of reagents mixing), substrate–film interaction during film deposition (sol viscosity, spin/dip coating parameters) and thermal processing of the as-deposited gel film (time and temperature of preheating between each layer deposition, time-temperature-atmosphere of postheating, time-temperature, atmosphere of final annealing) [26].

In the preparation of epitaxial ZnO films with high crystallinity, sapphire substrates of the a, c and r axis have been widely employed due to its stability at growth temperatures. However, the sapphire substrates are unsatisfactory to be used as electrodes, because of its high resistivity and are expensive. In this point of view, silicon (Si) wafers are interesting for the substrates on which optical devices are fabricated. The Si wafer is an especially suitable substrate for ZnO growth, because the thermal expansion coefficient of Si ( $3.57 \times 10^{-6}/^{\circ}\text{C}$ ) is nearly equal to that of ZnO ( $4 \times 10^{-6}/^{\circ}\text{C}$ ) [27].

Therefore the properties of TCO layers deposited on crystalline or amorphous (a-Si:H) Si substrates of Si based HJ solar cells is an important subject for investigation. It has been proved that the heterojunction (HJ) Si based solar cells (TCO/a-Si:H/Si) have conversion efficiency above 21% [28].

In general, ZnO films grown without intentional doping are n-type because of donor defects such as the oxygen vacancies and zinc interstitials. With regard to applications, ZnO:p-Si heterojunctions are of particular interest because this structure can be integrated with standard Si circuits using established technologies. ZnO/p-Si structures have been prepared and their properties studied by various investigators, but they mainly focused on non-intentionally doped ZnO [29].



## 2. ELECTRICAL PROPERTIES OF SOLID MATERIALS

Solids can be divided into three groups according to electrical properties (resistivity) as shown on Table 2.1. Materials with resistivity's value greater than  $10^8 \Omega\text{m}$  are considered insulating or dielectric. Materials with resistivity's value at between  $10^{-6}$ - $10^8 \Omega\text{m}$  are considered semiconductors. Materials with resistivity's value at between  $10^{-8}$ - $10^{-6} \Omega\text{m}$  are considered conductors [30].

**Table 2.1:** Classification of solid materials according to resistivity [30].

Materials	Resistivity, $\Omega\text{m}$
Conductors	$10^{-8} - 10^{-6}$
Semiconductors	$10^{-6} - 10^8$
Insulators	$\geq 10^8$

The origin of electronic conduction in solids can be understood by the application of the Schrödinger equation to the atoms in a solid. Several band theories including the tight binding model, Kronig-Pennel model and density functional theory [31] predict that the allowed electron energies fall into a series of two bands called the conduction and the valence bands separated by a forbidden gap known as the band gap. The band theory partially explains the distinction between the conductivity of metal, insulator and a semiconductor, since conduction could also be explained based on hopping of carriers. Also conduction could also take place via hopping. Figures 2.1 – 2.3 illustrate the band structures of these three types of materials [32].

### 2.1. Metals

An electric potential applied across a conducting material will cause electrons to become detached from their atoms and move (as they are negatively charged) towards the positive potential. As an electron leaves its atom, that atom is of course deficient of negative charge and becomes a positively charged ion. This makes it attractive to another electron that takes the place of the one just attracted away, and so on. Thus a flow of electrons moves, atom by atom towards the positive terminal, being replaced by an excess of electrons at the negative terminal [33].

In a conductor, there are a large number of easily detached electrons within the structure. Some of these electrons are already moving randomly about the structure due to thermal energy (heat) at room temperature and are called free electrons. Applying an electric potential across the conductor greatly increases the number of free electrons as they move from the negative to positive terminal as previously described. As these free electrons travel through the structure however, they are bound to collide with some of the electrons moving under the influence of heat, as well as being attracted to individual atoms as they jump from one atom's orbit to the next. It is these collisions and the pull of individual atomic nuclei, which give the material the electrical property of resistance. The resistance of a material indicates how well or how badly the material conducts (allows the movement of electrons under the influence of an electric potential or voltage). The higher the value of resistance, the more difficult it is to move the electrons. Materials with higher resistance will therefore need a higher potential (higher voltage) applied to cause a given amount of current, (movement of electrons) [33].

The conduction band of metal is believed to be either partially filled (such as Cu) or overlaps with the valence band (Zn) as shown in Fig. 2.1. Upon the application of small electric field to a metal, electrons move to unoccupied states close to the occupied states, since there is no band gap separating the conduction and the valence bands. As a result, metals have high electronic conductivity and high carrier mobility [32].

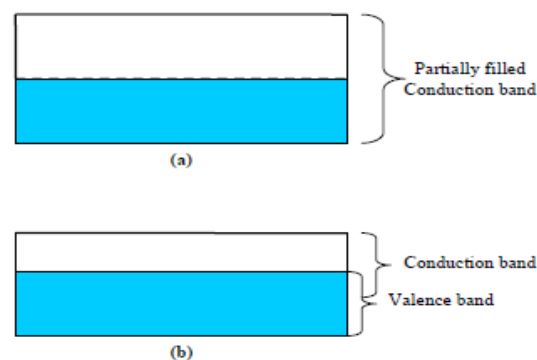


**Figure 2.1:** Schematic energy band representation of a metal; a) Partially filled conduction band (e.g. Cu), b) Overlapping bands (e.g. Zn or Pb) [32].

## 2.2. Insulators

An insulator has all its electrons tightly bonded to the nucleus and so it takes very large forces of either heat or potential to dislodge them.

Insulators do not normally pass current. In some cases, for example at high temperatures or with very high voltages applied, some insulating materials will conduct. In these circumstances, the insulating material is said to have "Broken down" and usually the structure of the material is permanently damaged. In some insulators (glass for example), heating the material to a high temperature will vibrate the atoms so violently that it will shake free enough electrons for conduction to occur. Cooling the material once more stops conduction. In most insulators however, conduction in a normally insulating material, whether caused by excessive heat or by excessive voltage will permanently destroy the material. For this reason insulating materials for electrical insulators, each have a safe working limit quoted by the manufacturer using the material, for both voltage and temperature [33].

The band structure of an insulator is depicted in Fig. 2.2. In the ideal situation, the valence band of the insulator is completely filled and the conduction band is completely empty. However, actually, there are a few empty levels in the valence band and some electrons in the conduction band. Upon the application of an electric field, very few electrons are able to cross over the large forbidden gap to the conduction band [32].

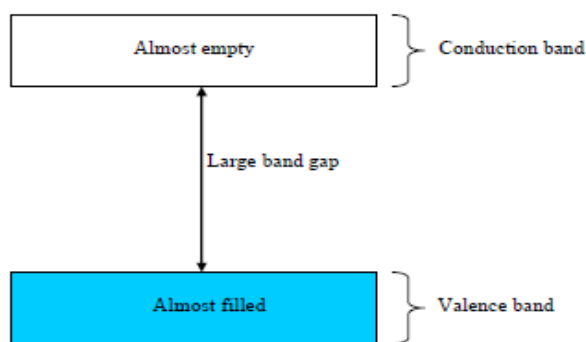


**Figure 2.2:** Schematic energy band representation of an insulator [32].

Owing to the strong bonding between the atoms and the large band gap between the conduction and the valence bands of insulators, they are characterised by very low electronic conductivity and mobility. Examples of this type of material include diamond,  $\text{SiO}_2$ ,  $\text{Al}_2\text{O}_3$ ,  $\text{S}_3\text{N}_4$  etc. [32].

### 2.3. Semiconductors

Semiconductors are materials with electronic properties intermediate between those of metals and insulators. Semiconductors are insulators at 0 Kelvin and that at this temperature the valence band is completely filled while the conduction band is empty [32].

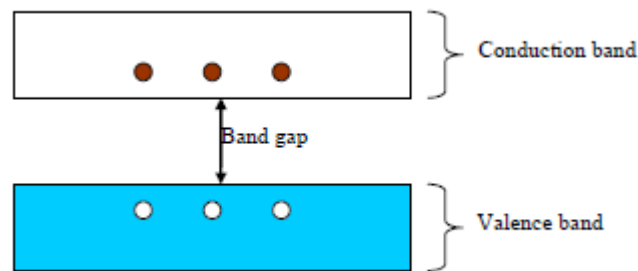


**Figure 2.3:** Schematic energy band representation of a semiconductor [32].

However as the temperature is raised, some electrons are raised to the conduction band thereby giving rise to electronic conduction. At room temperature, the energy band gap of the semiconductor is smaller, so also, the valence band is less populated and the conduction band is more populated with electrons than for the case of an insulator. A typical schematic diagram of the band structure of a semiconductor is shown in Fig. 2.3. When an electron is raised into the conduction band, this leads to a missing electron or an empty state in the valence band. This empty state may be filled by neighbouring electrons in the valence band that in turn results in a shift in the location of the empty state. The empty state in the valence band is considered to be a quasi-particle called a hole. It carries a positive charge and moves in the opposite direction to the electron [32].

There is no doubt that semiconductors changed the world beyond anything that could have been imagined before them. Although people have probably always needed to communicate and process data, it is thanks to the semiconductors that these two important tasks have become easy and take up infinitely less time. Semiconductors may be considered as the information carrier of our times. In the history of information, there were two revolutions (approximately 500 years apart). The first was that of Johan Gutenberg who made information available to many, the other is the invention of the transistor. Currently the global amount of information doubles every year. Many things we are taking for granted (such as, e.g., computers, Internet



and mobile phones) would not be possible without silicon microelectronics. Electronic circuits are also present in cars, home appliances, machinery, etc. Optoelectronic devices are equally important in everyday life, e.g., fiberoptic communications for data transfer, data storage (CD and DVD recorders), digital cameras, etc. [34]. Semiconductor devices such as diodes, transistors and integrated circuits can be found everywhere in our daily lives, in Walkman, televisions, automobiles, washing machines and computers. We have come to rely on them and increasingly have come to expect higher performance at lower cost [35].

### **2.3.1. Types of semiconductors**

Semiconductors are either elements or compounds. Si and Ge are most common elemental semiconductors. InSb, InAs, GaP, GaAs, SiC and GaN are compound semiconductors [36].

An intrinsic semiconductor conducts in its pure state. In this case, electron-hole pairs are equally thermally generated and the concentration of the electrons equals that of the holes. According to [37], the generation of intrinsic carriers is determined by the thermal excitation and recombination of electron holes. Under steady state conditions, the generation rate of electron-hole pairs must be equal to the recombination rate of electrons and holes. In solid-state electronics, either pure silicon or germanium may be used as the intrinsic semiconductor that forms the starting point for fabrication. As shown in Fig. 2.4, Silicon crystallizes in the same pattern as diamond, in a structure which Ashcroft and Mermin call "two interpenetrating face-centered cubic" primitive lattices. The lines between silicon atoms in the lattice illustration indicate nearest-neighbor bonds. The cube side for silicon is 0.543 nm. Germanium has the same diamond structure with a cell dimension of 0.566 nm. However, germanium will at a given temperature have more free electrons and a higher conductivity. Silicon is by far the more widely used semiconductor for electronics, partly because it can be used at much higher temperatures than germanium [38].

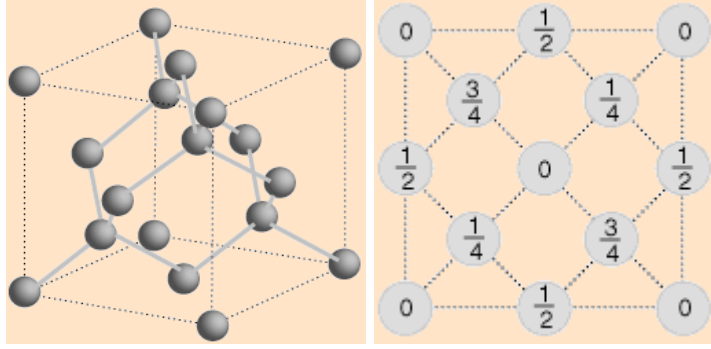


**Figure 2.4:** The diamond lattice of silicon and germanium [38].

An extrinsic semiconductor is formed when small quantity of foreign atoms known as dopant is introduced to the crystal of an intrinsic semiconductor in order to increase its electrical conductivity. Dopants introduce energy levels from which free carriers can move into the bands. Either extra electrons or holes can be introduced into the crystal by doping. The respective dopants are known as donors for semiconductors that have excess electrons (n-type) and acceptors for semiconductors that have excess holes (p-type) as carriers [32].

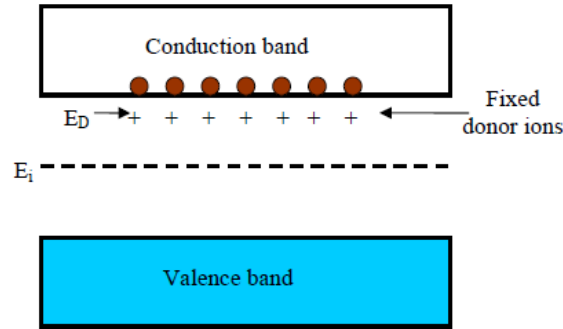


**Figure 2.5:** Schematic energy band representation of n-type extrinsic semiconductor [32].

The band diagrams of both n and p-type semiconductors are shown in Fig. 2.5 and 2.6, respectively. The donor impurity level is normally situated near the conduction band and when the thermal energy exceeds the small ionisation energy of the donor atoms, electrons will be raised into the conduction band as shown in Fig. 2.5, resulting in electrical conduction [32].

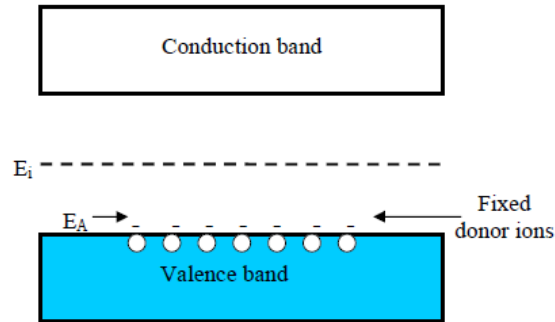


**Figure 2.6:** Schematic energy band representation of p-type extrinsic semiconductor [32].

In a similar a manner to the donor levels, at sufficient thermal energy, electrons are raised from the valence band to the acceptor level leading to the formation of holes in the valence band as illustrated in Fig. 2.6 [32].

As shown in Fig. 2.7, the addition of pentavalent impurities such as antimony (Sb), arsenic (As) or phosphorous (P) contributes free electrons, greatly increasing the conductivity of the intrinsic semiconductor.(N type Semiconductor) [38].

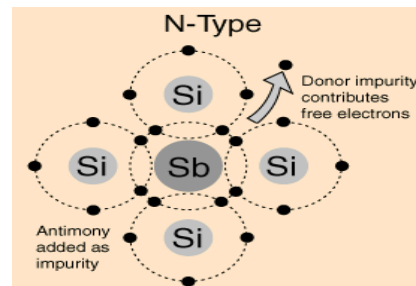


**Figure 2.7:** The lattice of n-type silicon [38].

As shown in Fig. 2.8, the addition of trivalent impurities such as boron (B), aluminum (Al) or gallium (Ga) to an intrinsic semiconductor creates deficiencies of valence electrons, called "holes" [38].

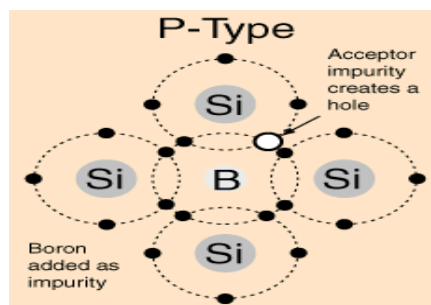


**Figure 2.8:** The lattice of p-type silicon [38].



### **3. ZINC OXIDE THIN FILMS**

Transparent conducting oxides (TCOs) are electrical conductive materials with a comparably low absorption of light. They are usually prepared with thin film technologies and used in opto-electrical devices such as solar cells, displays, opto-electrical interfaces and circuitries. Glass fibers are nearly less conductors of light, but electrical insulators; silicon and compound semiconductors are wavelength dependent optical resistors (generating mobile electrons), but dopant dependent electrical conductors. Transparent conducting oxides are highly flexible intermediate states with both these characteristics. Their conductivity can be tuned from insulating via semiconducting to conducting as well as their transparency adjusted. As they can be produced as n-type and p-type conductives, they open a wide range of power saving opto-electrical circuitries and technological applications.  $\text{In}_2\text{O}_3$ ,  $\text{SnO}_2$  and  $\text{ZnO}$  are metal oxides that widely used as transparent conductive oxide (TCO) materials [6].

#### **3.1. Properties of Zinc Oxide Thin Films**

$\text{ZnO}$  has received much attention over the past few years because it has a wide range of properties that depend on doping, including a range of conductivity from metallic to insulating (including n-type and p-type conductivity), high transparency, high piezoelectricity, wide-bandgap semiconductivity, room-temperature ferromagnetism, huge magnetooptic and chemical-sensing effects, non-toxicity, high resistivity control, high chemical, mechanical and thermal stability together with its abundance in nature which makes it a lower cost material [7]. These characteristics have made  $\text{ZnO}$  thin films very attractive for promising applications in solar cells, gas sensors, transducers, luminescent materials, transparent conductors, heat mirrors and semiconductor heterojunctions [8].

Most of the group II-VI binary compound semiconductors crystallize in either cubic zinc blende or hexagonal wurtzite (Wz) structure where each anion is surrounded by four cations at the corners of a tetrahedron, and vice versa. This tetrahedral

coordination is typical of sp covalent bonding nature, but these materials also have a substantial ionic character that tends to increase the bandgap beyond the one expected from the covalent bonding. ZnO is an II-VI compound semiconductor whose ionicity resides at the borderline between the covalent and ionic semiconductors. The crystal structures shared by ZnO are *wurtzite* (B4), *zinc blende* (B3), and *rocksalt* (or Rochelle salt) (B1) as schematically shown in Fig. 3.1. B1, B3, and B4 denote the *Strukturbericht* designations for the three phases. Under ambient conditions, the thermodynamically stable phase is that of wurtzite symmetry. The zinc blende ZnO structure can be stabilized only by growth on cubic substrates and the rocksalt or Rochelle salt (NaCl) structure may be obtained at relatively high pressures, as in the case of GaN. The *wurtzite* structure has a hexagonal unit cell with two lattice parameters  $a$  and  $c$  in the ratio of  $c/a = \sqrt{8/3} = 1.633$  (in an ideal wurtzite structure) [39].

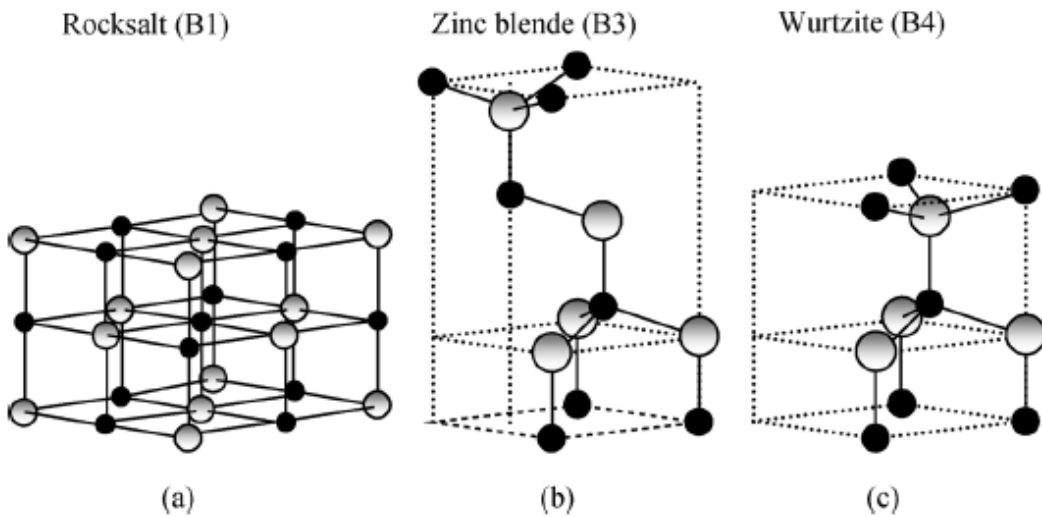


**Figure 3.1:** Stick and ball representation of ZnO crystal structures: a) cubic rocksalt (B1), b) cubic zinc blende (B3) and c) hexagonal wurzite (B4). Shaded gray and black spheres denote Zn and O atoms, respectively [39].

ZnO is an n-type II-VI semiconductor. ZnO has numerous attractive characteristics for electronics and optoelectronics devices. It has direct bandgap energy of 3.37 eV, which makes it transparent in visible light and operates in the UV to blue wavelengths. The exciton binding energy  $\sim 60$  meV for ZnO, as compared to GaN  $\sim 25$  meV; the higher exciton binding energy enhances the luminescence efficiency of light emission. The room temperature electron Hall mobility in single crystal ZnO is  $\sim 200 \text{ cm}^2 \text{ V}^{-1}$ , slightly lower than that of GaN, but ZnO has higher saturation velocity. ZnO has exhibited better radiation resistance than GaN for possible devices

used in space and nuclear applications [9]. ZnO can be grown on inexpensive substrate, such as glass, at relatively low temperatures. Nanostructures, such as nanowires and nanorods, have been demonstrated. These structures are ideal for detection applications due to its large surface area to volume ratio. Recent work on ZnO has shown ferromagnetism in ZnO by doping with transition metal, e.g. Mn, with practical Curie temperatures for spintronic devices [10]. One main attractive feature of ZnO is the ability to bandgap tuning via divalent substitution on the cation site to form heterostructures. Bandgap energy of ~3.0 eV can be achieved by doping with Cd<sup>+2</sup> while Mg<sup>+2</sup> increases the bandgap energy to ~4.0 eV [40].

### **3.2. Dopands and Their Effects on ZnO Thin Films**

Un-doped ZnO films which have poor electrical properties due to the low carrier concentration [11], showed high conductivity due to defects like oxygen vacancies and Zn interstitial. Its electrical properties are significantly affected by adsorption of O<sub>2</sub>, CO<sub>2</sub>, hydrocarbons, S-containing compounds, and water [12]. Doped ZnO thin films have better surface smoothness than un-doped ZnO thin films regardless of doping elements [11].

Single crystals and polycrystalline films of zinc oxide have been doped to enhance their mechanical, electrical, and optical properties with elements of the alkali metals such as Li, Ga, In, N, Al, Sn, and P from groups IIIB to VIIB [13]. However, Doping ZnO with appropriate impurities, from III group elements such as Al, Ga, and In determined to be the most suitable elements [14].

ZnO thin films doped with Ga have improved the optical transmittance in the visible region. The addition of Ga also induced an obvious increase in the optical band gap of these films; the optical band gap of Ga-doped films was slightly higher than that of undoped samples (3.1 eV). Ga can be effectively used to dope ZnO thin films for the purpose of enhancing optical properties, and increasing their band gap optical band gap increase due to doping. Optical parameters tended to increase with increasing doping concentration [41].

The transmittance of the AZO and GZO thin films was higher than 85% in the visible region, and the optical bandgap of the AZO and GZO thin films became broader with increasing Al or Ga dopant concentration because of the Burstein-Moss effect. In

conclusion, the structural, morphological, electrical, and optical characteristics of AZO and GZO thin films were observed, and Ga doping seems to be more effective [14].

### **3.2.1. Al doped zinc oxide thin films**

Tin-doped indium oxide ( $\text{In}_2\text{O}_3/\text{Sn}$ , ITO) has been the most commercially selected TCO material due to its excellent characteristics of low DC electrical resistivity ( $\sim 10^{-4} \Omega\text{cm}$ ) and high visible transmittance ( $>80\%$ ) [42]. Owing to the scarcity of its rare indium element, however, the cost of ITO films is expensive. In the last decade, Aluminum is commonly used as dopants for ZnO by replacing  $\text{Zn}^{+2}$  ions with  $\text{Al}^{+3}$  and showed photoluminescence in the ultraviolet (UV) and visible spectral range because of its optical properties and excitonic emission at room temperature. Aluminum-doped zinc oxide (ZnO:Al) has attracted much attention because of its low cost, good optical and electronic properties, heat stability, non-toxicity and high transparency in the near-infrared (IR) and invisible regions (90 %) [15].

If highly conductive and transparent AZO films could be made with an inexpensive deposition technique, the films could be a potential low-cost alternative to the widely used tin-doped indium oxide (ITO) [43].

ZnO doped with Al also can lead to a tunable band gap. Specially, ZnO:Al thin films with high c-axis orientated crystalline structure along (002) plane are potential device applications in broad band UV photodetectors with high tunable wavelength resolution [44]. Specially, ZnO:Al thin films can reduce the electrical resistivity due to an increase in carriers mobility by reducing the probability of the scattering of the carriers at the grain boundary [17].

### **3.3. Production Techniques of ZnO:Al Thin Films**

ZnO thin films have been prepared by employing various processes such as thermal evaporation, chemical vapor deposition (CVD), pulsed laser deposition (PLA), spray pyrolysis (SPT), sol-gel, RF magnetron sputtering, ion-beam sputtering (IBS) [20], metal organic chemical vapor deposition (MOCVD), ion-assisted deposition and reactive evaporation etc. [21]. In several studies, it was shown that the optical and electrical properties of AZO thin films could be obviously improved by optimizing deposition conditions and doping [22].



The underlying substrate-crystalline, amorphous or organic- may have an influence on the grown structure and the opto-electronic properties of the thin film [45], independent of the used deposition method. For example, in the case of solar cell production, an ultra-thin CdS buffer layer is usually the basis for ZnO: Al deposition. Even if the substrate is identical, the layer thickness (deposition time, position upon the substrate) itself influences the physical values of the deposited thin film [46]. A variation of the physical values from the grown thin films can also be reached by changing process parameters, as temperature [47] or pressure [48], or by additions to the process gas, as oxygen [49] or hydrogen [50].

A possible route to improve the electrical conduction and maintain the transmittance is to prepare AZO films with better crystal structure. In comparison with the other sputtering techniques, there are several advantages of ion-beam sputtering (IBS) deposition [51]. Particularly, IBS deposition is executed in a high-vacuum environment and with tunable ion-beam energy that enables the preparation of high-purity films. Besides, epitaxial ZnO films on sapphire substrates have great potential for applications of both surface acoustic wave (SAW) filters in the GHz range and UV light emitting devices [20].

RF magnetron sputtering since the ZnO:Al films produced by this method offer safety advantages, avoid the use of toxic gases, have low cost, have a high stability against a hydrogen plasma and heat cycling, and grow at a low temperature with good optical and electronic properties. In addition, sputtering of the ZnO:Al has a relatively high deposition rate and hence is well suited to industrial-scale large-area deposition [52].

Compared to other thin film deposition techniques, SPT offers advantage of use of inexpensive equipment (non-vacuum method), ease of large-scale adoption by moving nozzle over a large substrate and possibility of microprocessor based spraying which is useful tool in electronics. In SPT, there is easy control of roughness leading to light scattering that is a useful tool in solar cells and ease of tailoring of film properties for desired application by changing deposition and post deposition conditions. Resistivity of sprayed doped ZnO has arrived at a stage of favourable comparison with those from other well-established deposition techniques such as sputtering [53].

Among these, the sol–gel process presents an easy way to integrate ZnO devices into the Si technology, since it offers the possibility of excellent compositional control, multicomponent oxide layers of many compositions on substrate, simplicity, homogeneity, lower crystallization temperature and low production costs [23]. This technique offers the possibility of preparing a small as well as large-area coating of ZnO thin films at low cost for technological applications. However, the sol–gel method is difficult to obtain high preferential c-axis orientation films due to its film growth procedure [17]. The ZnO thin films prepared by sol-gel technique show high optical transmittance (85-90%) in the near UV, VIS and IR regions [24].

## 4. SOL GEL COATING TECHNIQUE

Sol-Gel is a coating technique (see Fig. 4.1) which can be applied on glass, ceramic, metals and polymers to improve the optical, electrical, chemical and mechanical properties of surfaces [54].

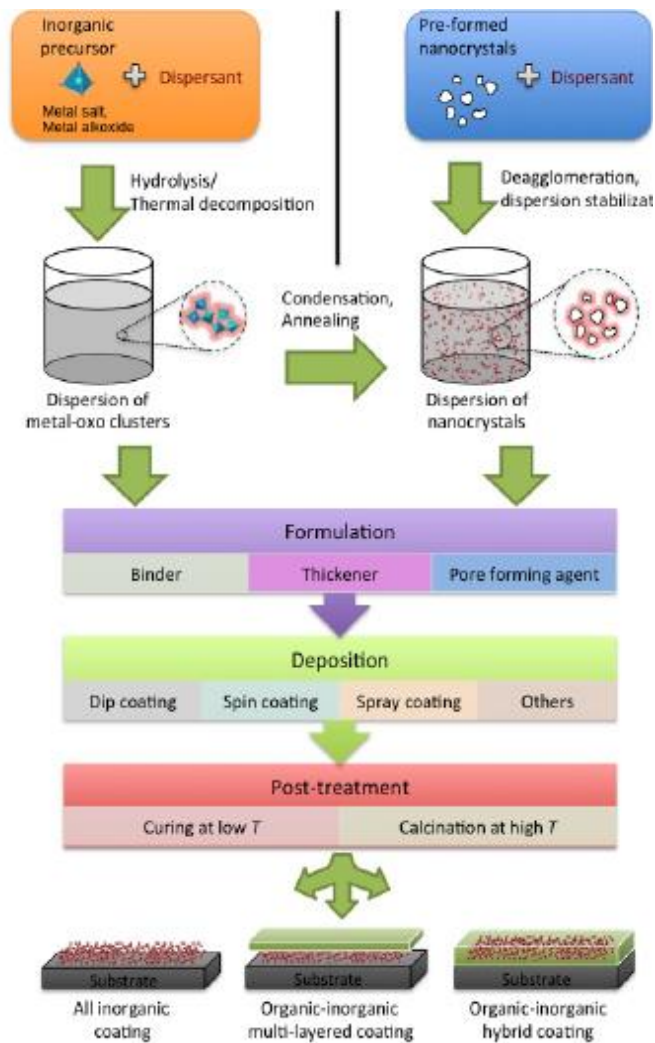


**Figure 4.1:** Schematic illustration of the main processing steps involved in the formation of transparent coatings containing oxide nanoparticles [54].

The sol-gel chemical process is self-described in the definition of a sol, a gel, and a summary of the process in which a sol evolves into a gel (Fig. 4.2) [55].

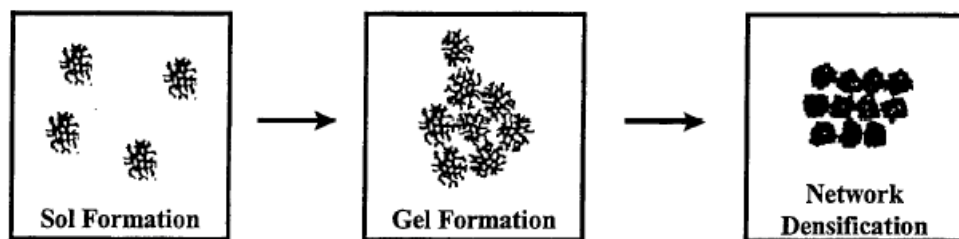


**Figure 4.2:** Colloidal network formation in sol-gel materials [55].

A sol is a colloidal dispersion of small particles in a liquid; a gel is usually a substance composed of a continuous network encompassing a continuous liquid phase [56]. Sol-gel reactions promote the growth of colloidal particles (sol) and their subsequent network formation (gel) through the hydrolysis and condensation reactions of inorganic alkoxide monomers. The precursors for synthesizing these colloids consist of a metal or metalloid element surrounded by various reactive ligands. Metal alkoxides are most popular because they react readily with water. The most widely used metal alkoxides are the alkoxysilanes, such as tetramethoxysilane (TMOS) and tetraethoxysilane (TEOS). However, other alkoxides such as aluminates, titanates, zirconates, and borates are also commonly used in the sol-gel process, either alone or in combination with other alkoxides such as TEOS [57].

As shown in Fig. 4.3, the fabrication and use of materials prepared by sol-gel process can be divided into three main categories, bulk glass, coatings and fibers [58].

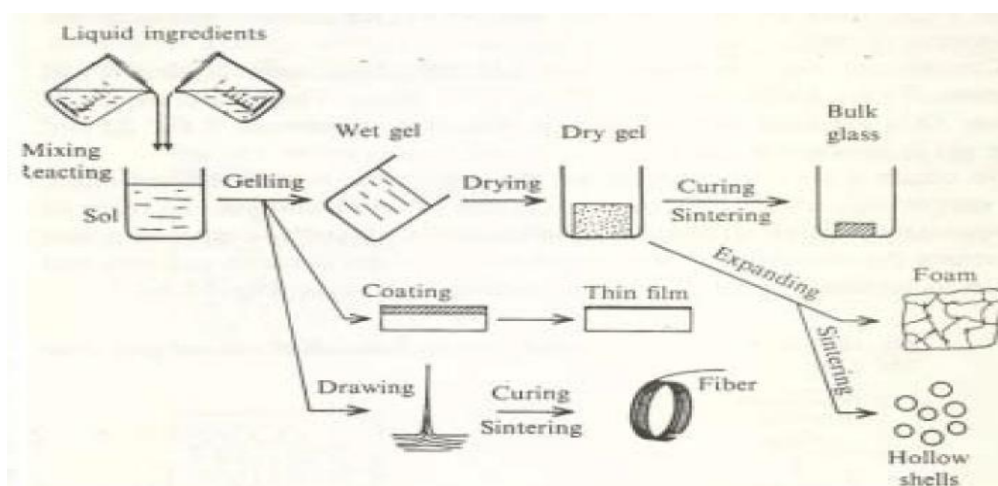


**Figure 4.3:** Sol-Gel routes for glass formation [58].

#### 4.1. Applications of Sol-Gel Process

While it was studied earlier, sol-gel chemistry has been investigated extensively since the mid-1970s, when sol-gel reactions were shown to produce a variety of inorganic networks that can be formed from metal aloxide solutions [59].

The sol-gel technique offers a low-temperature method for synthesizing materials that are either totally inorganic in nature or both inorganic and organic. The process, which is based on the hydrolysis and condensation reaction of organometallic compounds in alcoholic solutions, offers many advantages for the fabrication of coatings, including excellent control of the stoichiometry of precursor solutions, ease of compositional modifications, customizable microstructure, ease of introducing various functional groups or encapsulating sensing elements, relatively low annealing temperatures, the possibility of coating deposition on large area substrates, and simple and inexpensive equipment. Within the past several years, a number of developments in precursor solutions, coating processes and equipment have made the sol-gel technique even more widespread [60].

The final film microstructure and properties depend on: *i*) the structure of the entrained inorganic species in the original sol (for example, size and fractal dimension), *ii*) the reactivity of these species (for example, condensation or aggregation rates), *iii*) the time scale of the deposition process (related to evaporation rate and film thickness), and *iv*) the magnitude of shear forces and capillary forces that accompany film deposition (related to surface tension of the solvent or carrier and surface tension gradients). The most common means of controlling the film microstructure is through particle size. For unaggregated, monosized particulate sols, the pore size decreases and the surface area increases with decreasing particle size [57]. Chemical precursors play a key role in the sol-gel coating by directly affecting the porosity, refractive index, hardness and other performance characteristics of the resultant coatings and thin films. In addition, the precursor is frequently a decisive factor for production in terms of cost and usability [60].

The process consists of successive five stages, preparing the sol, preparing the substrates, film deposition, pre-heating and post heating. The stages are shown in Fig. 4.4. In preparing the sol stage, all the required chemicals are mixed in estimated ratios to form homogeneous, clear and transparent sol. Then the prepared sol is aged

for a certain time. In the second stage, the substrates are cleaned ultrasonically in acetone and alcohol then dried in air, respectively. Film deposition stage starts with dipping the prepared substrate in the prepared solution for a certain time until the substrate is completely wetted and the film thickness reaches satisfactory levels then finished by withdrawal the substrate from the sol at a controlled rate. In pre-heating organic residuals are evaporated. The decomposing of the strong radicals and the forming of the crystal structure take place in post heating.



**Figure 4.4:** Stages of coating process via sol-gel process.

Sol-gel process can be used to fabricate almost any single or multi-component oxide coating. Such coatings have been deposited on glass to provide coloration, anti-reflection, selective reflection, electrochromism and photochromism, selective absorption, wave guiding, reduced friction, anti-soiling reduced adhesion, transparent conductors, electro-optics, ferro-electrics, sensors, and dye lasers [25].

## **4.2. Deposition Techniques of Sol-Gel**

Several methods can be used to make sol-gel coatings with the sol-gel process such as spin coating, dip coating, flow coating, laminar coating, roll coating and spray coating. Spin coating and dip coating are two basic techniques used to deposit sol-gel coatings. Spin coating produces a one-sided coating, while dip coating yields a double-sided coating. Both techniques are used in manufacturing to make different coatings and thin films [60].

### **4.2.1. Spin coating technique**

Spin coating is used for many applications where relatively flat substrates or objects are coated with thin layers of material. For example, several cathode ray tube (CRT) manufacturers use the spin coating method to make anti-glare or anti-reflection coatings. In spin coating, the material to be made into coating is dissolved or dispersed into a solvent, and this coating solution is then deposited onto the surface

and spun off to leave a uniform layer for subsequent processing stages and ultimate use [60].

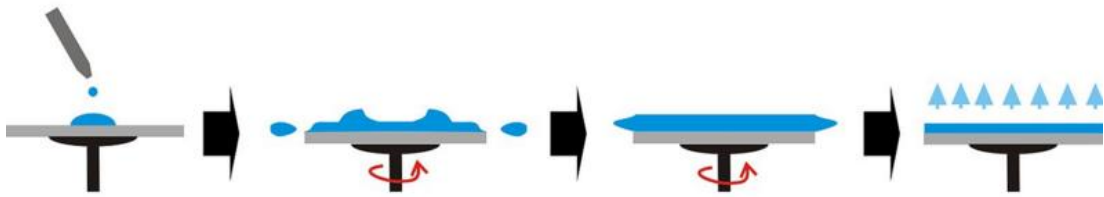


**Figure 4.5:** The four stages of spin coating [60].

There are four key stages in spin coating as shown Fig.4.5: • *Stage 1*: The deposition of the coating fluid onto the substrate • *Stage 2*: Aggressive fluid expulsion from the substrate surface by the rotational motion • *Stage 3*: Gradual fluid thinning • *Stage 4*: Coating thinning by solvent evaporation.

The coating thickness is inversely proportional to the square root of the rotation speed: thickness  $\sim [1/\text{speed}]^{1/2}$ . In addition, the coating solution properties (such as viscosity and liquid density) also affect coating thickness.

Some spin coating systems are specifically designed for depositing scratchresistant coatings on ophthalmic lenses. These systems have multiple functions, including cleaning, providing the solution, spin coating and curing (either thermal or ultraviolet). The temperature and atmosphere in the chamber environment can be precisely controlled to ensure high quality results [60].

#### **4.2.2.Roll/Gravure coating technique**

Roll coating is a process by which a thin liquid film is formed on a continuously moving web or substrate by using one or more rotating rolls. Gravure coating is a roll coating technique that has evolved from the printing industry as shown Fig.4.6 [61].

## DIRECT GRAVURE COATING

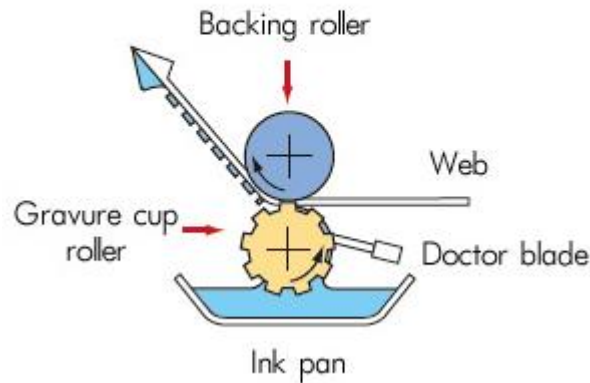


**Figure 4.6:** Gravure coating evolved from the printing industry [61].

It is used to apply very thin coatings of low-viscosity liquids at high speed. Typical coatings are 1-50  $\mu\text{m}$  thick, and the coating speed can be up to 15 meters per second.

The most important feature of a gravure coater is the patterned chrome roll. The pattern of cells or grooves is engraved onto the surface of the roll by mechanical engraving (knurling), chemical etching or electromechanical engraving. An excess of coating solution is applied to the gravure roll, which is then doctored by a flexible blade. The blade meters the cells partially full of coating liquid. The cells then pass into a nip where a fraction of the coating in the cells is transferred either to the web (in direct gravure) or to the offset roll (in offset gravure). In an offset gravure coater, the final transfer of coating to the web is at a second nip.

The main strength of gravure coating is the ability to apply thin coatings at high speed, with the coating thickness and uniformity controlled by the cell volume and cell uniformity. However, this method also has several drawbacks. Changing the coating thickness more than a small amount requires the gravure roll to be changed because the coating thickness is primarily determined by the volume of the cells on the gravure roll. Each cell must act like all the others, and the stability of the removal of the film from each cell is difficult to achieve at higher speeds and lower coating thickness. Additionally, wear of the gravure roll can be a problem when using abrasive coating formulations [61].



This technique has been used to make anti-reflective coatings on plastic films. The resultant coating is uniform and shows good mechanical performance. The coating can be made at a speed of up to 250 ft per minute.

There are many types of sol gel deposition techniques such as spin coating, dip coating, flow coating, laminar coating, roll coating and spray coating. Dip coating is the most widely used sol gel deposition technique because of its easy application procedure and low cost [61].

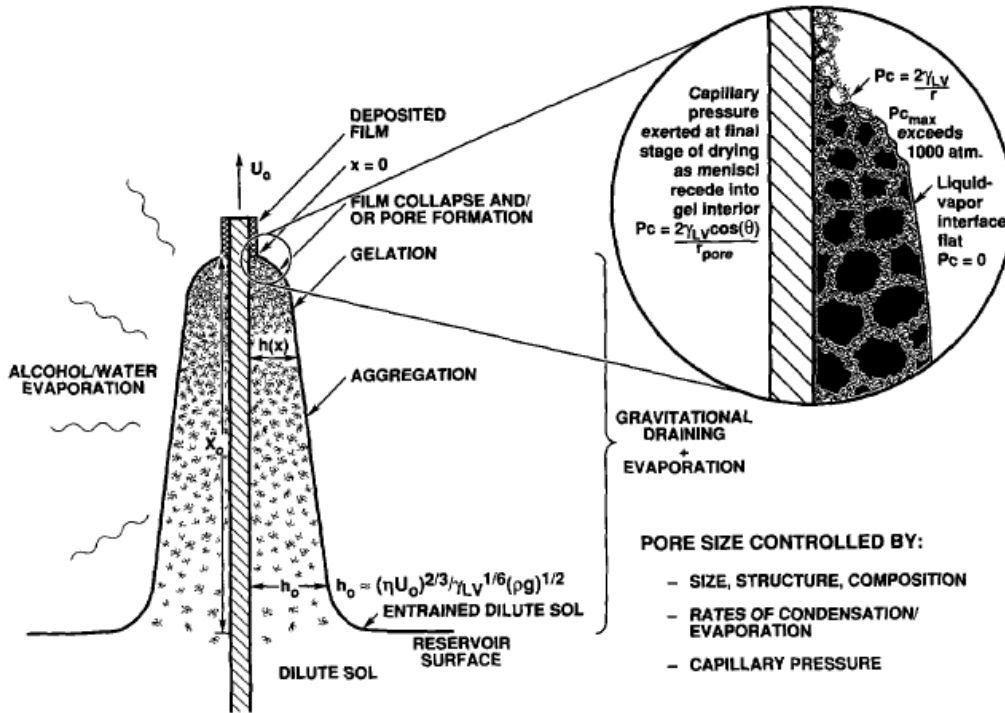
#### **4.2.3.Dip coating technique**

Thin films formed by a dip-coating process represent the oldest commercial application of sol-gel technology. The first patent based on this process was issued to Jenaer Glaswerk Schott & Gen. in 1939 for silica films.

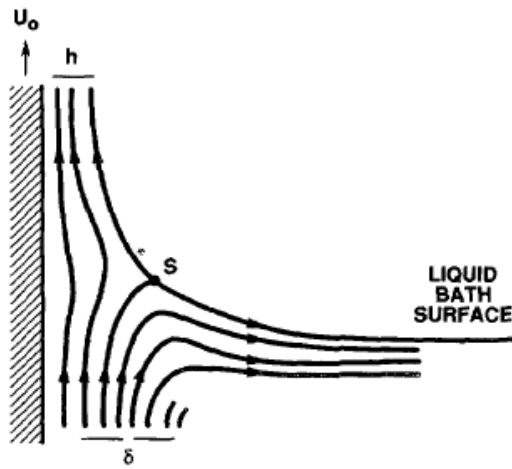
The only requirements for successful dip-coating are that the condensed phase remain dispersed in the fluid medium, that macroscopic gelation be avoided, and that the sol be sufficiently dilute so that upon deposition the critical cracking thickness not be exceeded [57].

In dip coating, the substrate is normally withdrawn vertically from the coating bath at a constant speed  $U_0$  (Fig. 4.7a) [62]. The moving substrate entrains the liquid in a viscous boundary layer that splits in two at the free surface (point S in Fig. 4.7b), returning the outer layer to the bath. Since the solvent is evaporating and draining, the entrained film acquires an approximate wedge shape that terminates in a well-defined drying line ( $x = 0$  in Figure 4.7a). Above the stagnation point S (Fig. 4.7b), when the upward moving flux is balanced by that due to evaporation, the film position and shape of the film profile remain steady with respect to the coating bath surface. Within the thinning film, the inorganic species are progressively concentrated by evaporation, leading to aggregation, gelation, and final drying to form a type of a dry gel or xerogel [57].

## SOL-GEL DIP-COATING



a)



b)

**Figure 4.7:** a) Schematic of the steady-state dip-coating process, showing the sequential stages of structural development that result from draining accompanied by solvent evaporation and continued condensation reactions,  $U_0$  is the withdrawal speed,  $h(x)$  is the film thickness at position  $x$  measured from the drying line  $\lambda_0$ ,  $h_0$  is the entrained film thickness just above the stagnation point  $S$ ,  $\eta$  is the liquid viscosity,  $\rho$  is the liquid density,  $P$  is the capillary pressure,  $\gamma_{LV}$  is the surface tension, and  $\theta$  is the wetting angle. b) Detail of the flow patterns (streamlines) during dip coating.  $\delta$  is the boundary layer, and  $h$  is the thickness of the fluid film [57].

Dip coating is a process where the substrate to be coated is immersed in a liquid and then withdrawn with a well-defined withdrawal speed under controlled temperature

and atmospheric conditions. Schematic drawing of dip coating process is shown in Fig. 4.8.

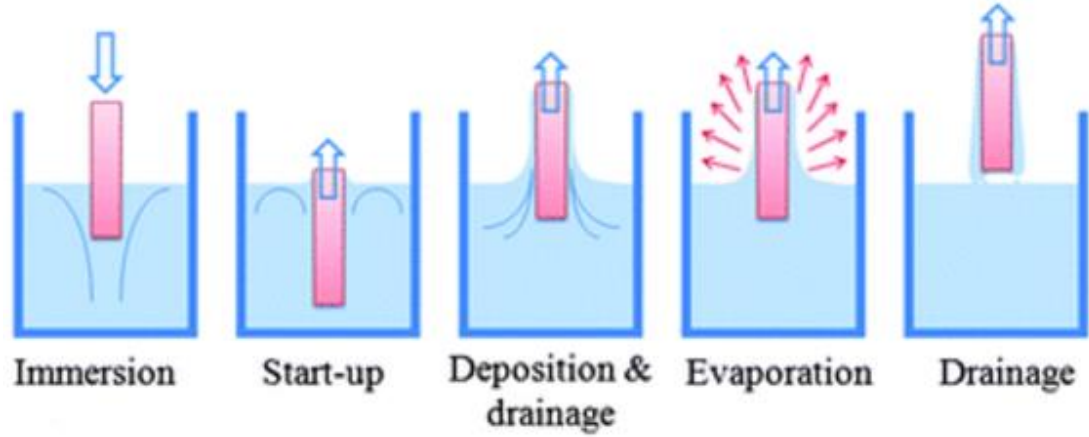


**Figure 4.8:** Schematic drawing of dip coating process [58].

Vibration-free mountings and very smooth movement of the substrate is essential for dip systems. An accurate and uniform coating thickness depends on precise speed control and minimal vibration of the substrate and fluid surface. The coating thickness is mainly defined by the withdrawal speed, the solid content and the viscosity of the liquid. If the withdrawal speed is chosen such that the sheer rates keep the system in the Newtonian regime, the coating thickness can be calculated by the Landau-Levich equation (4.1):

$$h = 0.94 \frac{(\eta v)^{2/3}}{(\rho g)^{1/2} \gamma^{1/6}} \quad (4.1)$$

where  $h$  = coating thickness,  $v$  = viscosity,  $\gamma$  = liquid-vapor surface tension,  $\rho$  = density,  $g$  = gravity [63]. Other parameters affecting the coating thickness are surface tension of the solution, vapor pressure and relative humidity above the coating bath [58].

The advantages of the dip coating technique are the high degree of uniformity obtained, simple thickness control, low labor and cost, low processing temperature, good shape ability and minimal manpower-equipment requirements [64].

One dip coating system commonly used for sol-gel coatings incorporates atmosphere control, drying/curing, a programmable dip coating profile (withdraw speed, immersion time, etc.) and solution manageable tanks (temperature, filtration, etc.). Accurate speed control is obtained by a proven precision, off-the- shelf motion

system. Vibration control is enhanced by structural rigidity, isolation of the tank and motor drive, and spring mounting supports. Such a system is capable of achieving a uniform coating ( $\pm 3$  % thickness variation) [60].

The sol-gel dip process is almost exclusively applied for the fabrication of transparent layers, primarily for the deposition of oxide films on float glass as a transparent substrate with a high degree of planarity and surface quality [58].

## 5. P-N JUNCTIONS

Heterostructures such as p-n junction have been used in fabricating the switching diodes, diode rectifiers, solar cells, light emitting diodes (LEDs), laser diodes (LDs), photodetectors, bipolar junction transistors (BJTs), heterojunction bipolar transistors (HBTs), and junction field-effect transistors (JFETs), metal-semiconductor field-effect transistors (MESFETs), high-electron mobility transistors (HEMTs), tunnel diodes, multiquantum well (MQW) and superlattice (SL) devices [65].

### 5.1.P-N Junctions Diodes

A p-n junction diode can be fabricated by doping the semiconductor material with opposite doping impurities (i.e., acceptor or donor impurities) to form the p and n regions of the diode. Since the p-n junction is formed on the same semiconductor, it is referred to as a p-n homojunction diode. On the other hand, if a p-n junction is formed by using two semiconductor materials of different band gaps and with opposite doping impurities, then it is referred to as a p-n heterojunction diode [65].

Doping one side of a piece of silicon with boron (a p-type dopant) and the other side with phosphorus (an n-type dopant) form a *p-n* junction. The n-type material has large numbers of free electrons (negatively charged) that can move through the material. The number of positively charged phosphorus atoms (called positive ions), which are not free to move, exactly balance the number and charge of these negative free electrons. Similarly, for the p-type material, there are large numbers of free holes (positively charged) that can move through the material. Their number and positive charge is exactly counter-balanced by the number of negatively charged boron atoms (called negative ions) [66].

When n-type and the p-type materials are brought together, Due to the doping of the silicon crystal, there are large numbers of mobile electrons on the n-type side, but very few mobile electrons on the p-type side. Because of the random thermal motion of the free electrons, electrons from the n-type side start to diffuse into the p-type side. Similarly, due to the doping of the silicon, there are large numbers of mobile

holes on the p-type side, but very few mobile holes on the n-type side. Holes in the p-type side, therefore, start to diffuse across into the n-type side. Now, if the electrons and holes had no electric charge, this diffusion process would eventually result in the electrons and holes being uniformly distributed throughout the entire volume.

As the electrons in the n-type material diffuse across towards the p-type side, they leave behind positively charged phosphorus ions, near the interface between the n and p regions. Similarly, the positive holes in the p-type region diffuse towards the n-type side and leave behind negatively charged boron ions as shown Fig. 5.1. In a process called "diffusion", the random motions of mobile electrons and holes over time cause them to attempt to distribute equally within the total volume. As they cross the junction, the fixed ions they leave behind establish a "built-in" electric field at the junction [66].

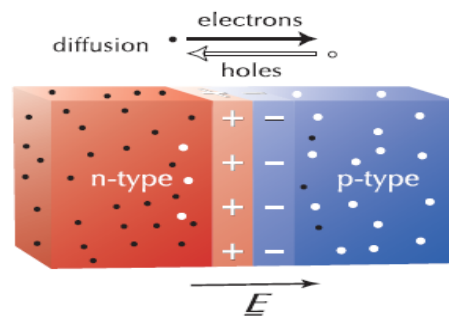


**Figure 5.1:** Diffusion establishes ‘built-in’ electric field [66].

These fixed ions set up an electric field right at the junction between the n-type and p-type material. This electric field points from the positively charged ions in the n-type material to the negatively charged ions in the p-type material. The free electrons and holes are influenced by this "built-in" electric field with the electrons being attracted towards the positive phosphorus ions and the holes being attracted towards the negative boron ions. Thus, the “built-in” electric field causes some of the electrons and holes to flow in the opposite direction to the flow caused by diffusion as shown Fig. 5.2. A mobile electron or hole near the "built-in" electric field will be attracted and swept back into its original volume. At the junction there are two effects occurring *i*) diffusion with electrons moving from n-type to p-type and, *ii*) the "built in" electric field sweeping locally affected electrons back into the n-type volume. The holes are affected similarly but in opposite directions [66].

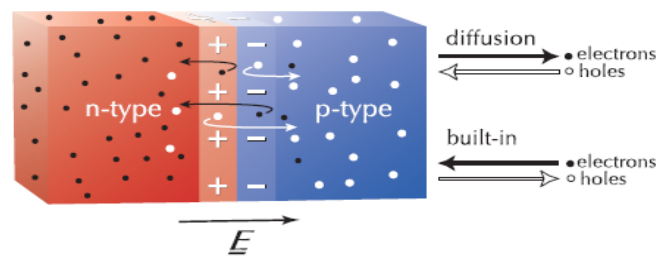


**Figure 5.2:** Motion of mobile electrons and holes due to diffusion and the ‘built-in’ electric field [66].

These opposing flows eventually reach a stable equilibrium with the number of electrons flowing due to diffusion exactly balancing the number of electrons flowing back due to the electric field. The net flow of electrons across the junction is zero and the net flow of holes across the junction is zero [66].

Within the depletion region as shown Fig. 5.3, there are very few mobile electrons and holes. It is "depleted" of mobile charges, leaving only the fixed charges associated with the dopant atoms. As a result, the depletion region is highly resistive and now behaves as if it were pure crystalline silicon: as a nearly perfect insulator. The resistance of the depletion region can be modified by "adding" an external electric field to the "built-in" electric field. If the "added" electric field is in the same direction as the "built-in" electric field, the depletion region's resistance will become greater. If the "added" electric field is opposite in direction to the "built-in" electric field, the depletion region's resistance will become smaller. The depletion region can therefore be considered to operate as a voltage-controlled resistor [67].

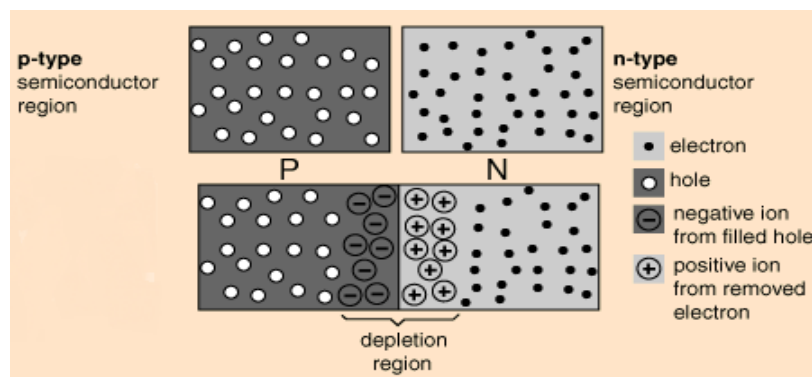


**Figure 5.3:** Depletion region [67]

### 5.1.1. Bias of P-N junctions

Semiconductor devices have three modes of operation: *i) Thermal Equilibrium (Zero Bias)*: At thermal equilibrium, there are no external inputs such as light or applied voltage. The currents balance each other out so there is no net current within the device. *ii) Steady State*: Under steady state, there are external inputs such as light or applied voltage, but the conditions do not change with time. Devices typically operate in steady state and are either in forward or reverse bias. *iii) Transient*: If the applied voltage changes rapidly, there will be a short delay before the solar cell responds. As solar cells are not used for high speed operation there are few extra transient effects that need to be taken into account [68].

If an external potential is applied to the terminals of P-N junction, it will alter the potential between the P and N regions. This potential difference can alter the flow of majority carriers, so that the P-N junction can be used as an opportunity for the diffusion of electrons and holes. If the voltage applied decreases, the width of the depletion layer, then the diode is assumed to be in forward bias and if the applied voltage increases the depletion layer width then the diode is assumed to be in reverse bias. If the width of depletion layer do not alters then it is in the zero bias state [69].

#### 5.1.1.1. Zero bias or thermal equilibrium

In zero bias or thermal equilibrium as shown Fig. 5.4 state junction potential provides higher potential energy to the holes on the P-side than the N-side. If the terminals of junction diode are shorted, few majority charge carriers (holes) in the P side with sufficient energy to surmount the potential barrier travel across the depletion region. Therefore, with the help of holes, current starts to flow in the diode and it is referred to as forward current. In the similar manner, holes in the N side move across the depletion region in reverse direction and the current generated in this fashion is referred to as reverse current.

Potential barrier opposes the migration of electrons and holes across the junction and allow the minority charge carriers to drift across the P-N junction. As a result of it, a state of equilibrium is established when the majority charge carriers are equal in concentration on either side of the junction and when minority charge carriers are moving in opposite directions. A net zero current flows in the circuit and the junction is said to be in dynamic equilibrium. By increasing the temperature of



semiconductors, minority charge carriers have been continuously generated and thereby leakage current starts to rise. In general no conduction of electric current takes place because no external source is connected to the P-N junction [69].

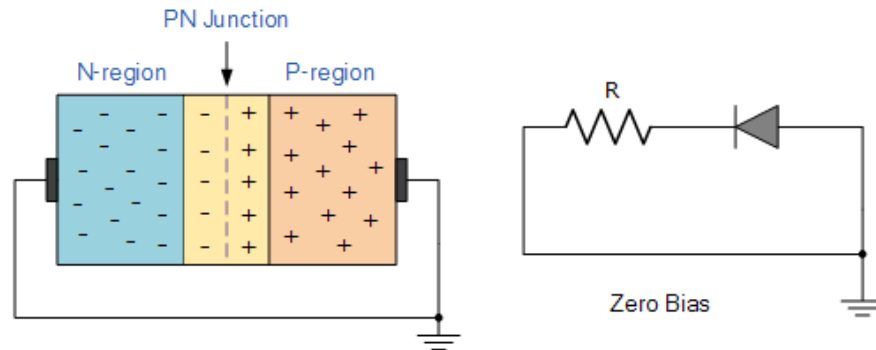


**Figure 5.4:** Zero bias of the p-n junction [69].

#### 5.1.1.2. Forward bias

When a diode is connected in a Forward Bias condition, a negative voltage is applied to the N-type material and a positive voltage is applied to the P-type material. If this external voltage becomes greater than the value of the potential barrier, approx. 0.7 volts for silicon and 0.3 volts for germanium, the potential barriers opposition will be overcome and current will start to flow.

This is because the negative voltage pushes or repels electrons towards the junction giving them the energy to cross over and combine with the holes being pushed in the opposite direction towards the junction by the positive voltage. This results in a characteristics curve of zero current flowing up to this voltage point, called the “knee” on the static curves and then a high current flow through the diode with little increase in the external voltage as shown Fig.5.5 [70].

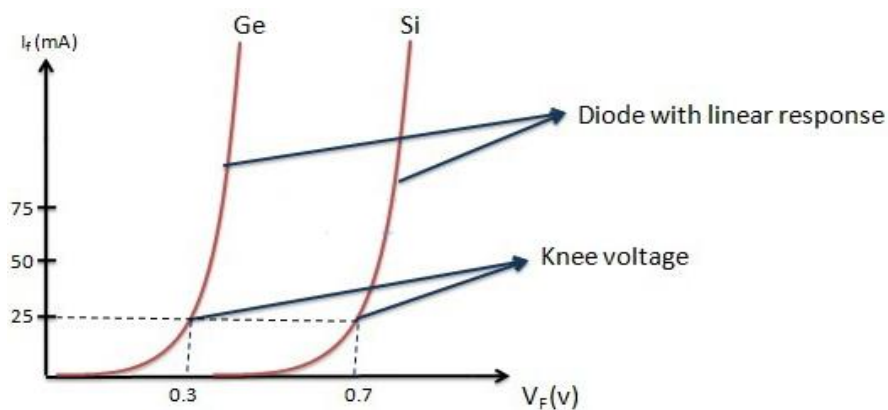


**Figure 5.5:** Forward characteristics curve for a junction diode [70].

The application of a forward biasing voltage on the junction diode results in the depletion layer becoming very thin as shown Fig. 5.6 and narrow which represents a low impedance path through the junction thereby allowing high currents to flow. The point at which this sudden increase in current takes place is represented on the static I-V characteristics curve above as the “knee” point [70].

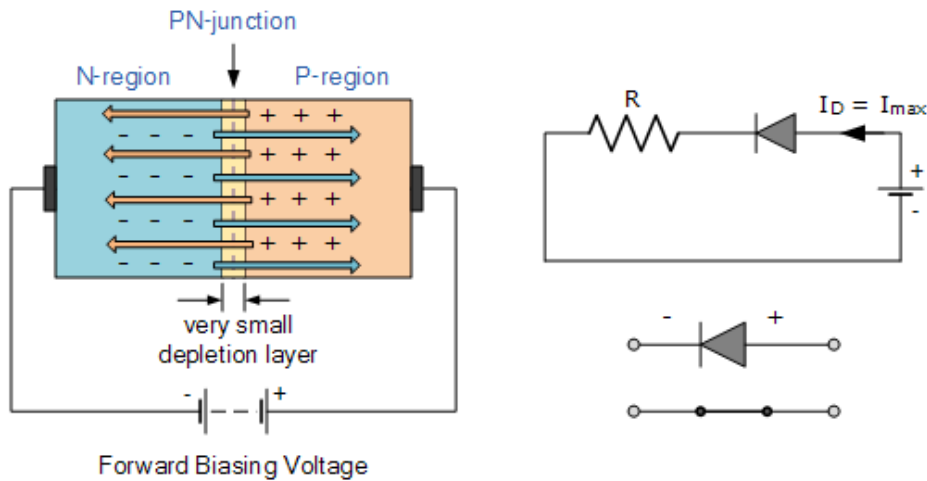


**Figure 5.6:** Reduction in the depletion layer due to forward bias [70].

This condition represents the low resistance path through the PN junction allowing very large currents to flow through the diode with only a small increase in bias voltage. The actual potential difference across the junction or diode is kept constant by the action of the depletion layer at approximately 0.3v for germanium and approximately 0.7v for silicon junction diodes.

Since the diode can conduct “infinite” current above this knee point as it effectively becomes a short circuit, therefore resistors are used in series with the diode to limit its current flow. Exceeding its maximum forward current specification causes the device to dissipate more power in the form of heat than it was designed for resulting in a very quick failure of the device [70].

### 5.1.1.3. Reverse bias

When a diode is connected in a Reverse Bias condition, a positive voltage is applied to the N-type material and a negative voltage is applied to the P-type material.

The positive voltage applied to the N-type material attracts electrons towards the positive electrode and away from the junction, while the holes in the P-type end are also attracted away from the junction towards the negative electrode.

The net result is that the depletion layer grows wider as shown Fig.5.7 due to a lack of electrons and holes and presents a high impedance path, almost an insulator. The result is that a high potential barrier is created thus preventing current from flowing through the semiconductor material [70].

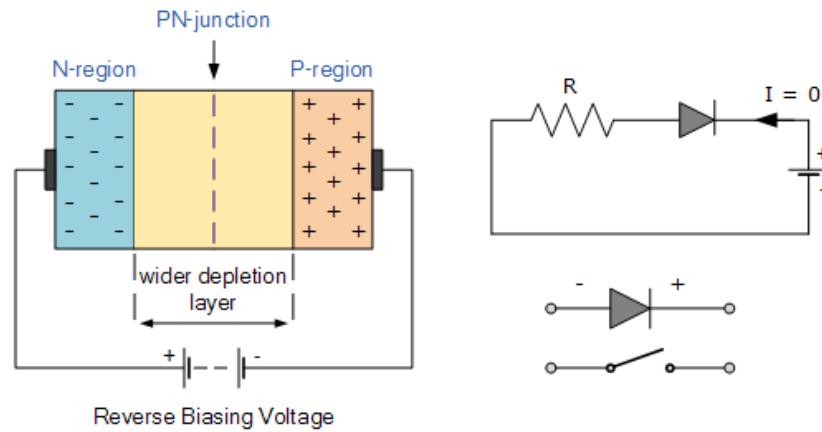


**Figure 5.7:** Increase in the depletion layer due to reverse bias [70].

This condition represents a high resistance value to the P-N junction and practically zero current flows through the junction diode with an increase in bias voltage. However, a very small leakage current does flow through the junction which can be measured in micro-amperes, ( $\mu\text{A}$ ).

One final point, if the reverse bias voltage  $V_r$  applied to the diode is increased to a sufficiently high enough value, it will cause the diode's P-N junction to overheat and fail due to the avalanche effect around the junction. This may cause the diode to become shorted and will result in the flow of maximum circuit current and this shown as a step downward slope in the reverse static characteristics curve below as shown Fig.5.8 [70].

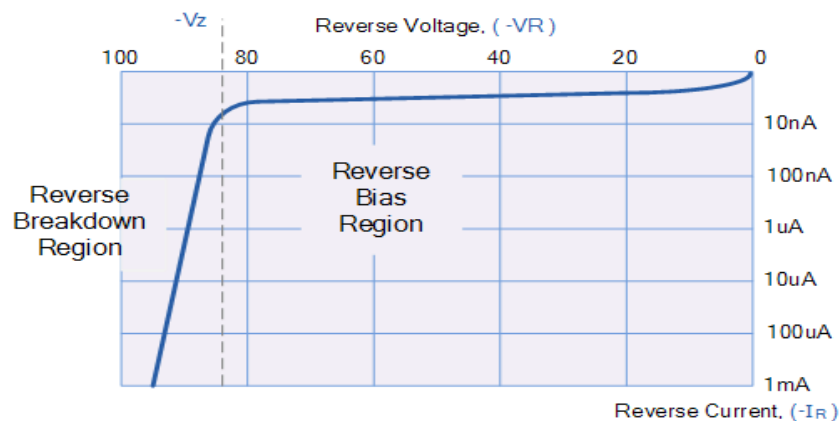


**Figure 5.8:** Reverse characteristics curve for a junction diode [70].

Sometimes this avalanche effect has practical applications in voltage stabilising circuits where a series limiting resistor is used with the diode to limit this reverse breakdown current to a preset maximum value thereby producing a fixed voltage output across the diode. These types of diodes are commonly known as Zener Diodes [70]. Typical I–V diode characteristics are shown in Fig.5.9 [71].

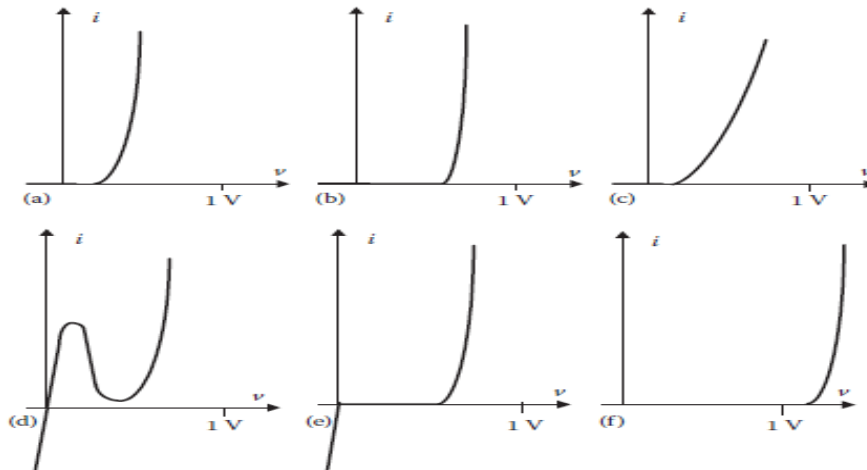


**Figure 5.9:** Forward current–voltage characteristics of various types of diodes: a) germanium diode, b) silicon diode, c) Schottky diode, d) tunnel diode, e) backward diode, and f) LED [71].

### 5.1.2. I-V Characteristics of P-N junction diode

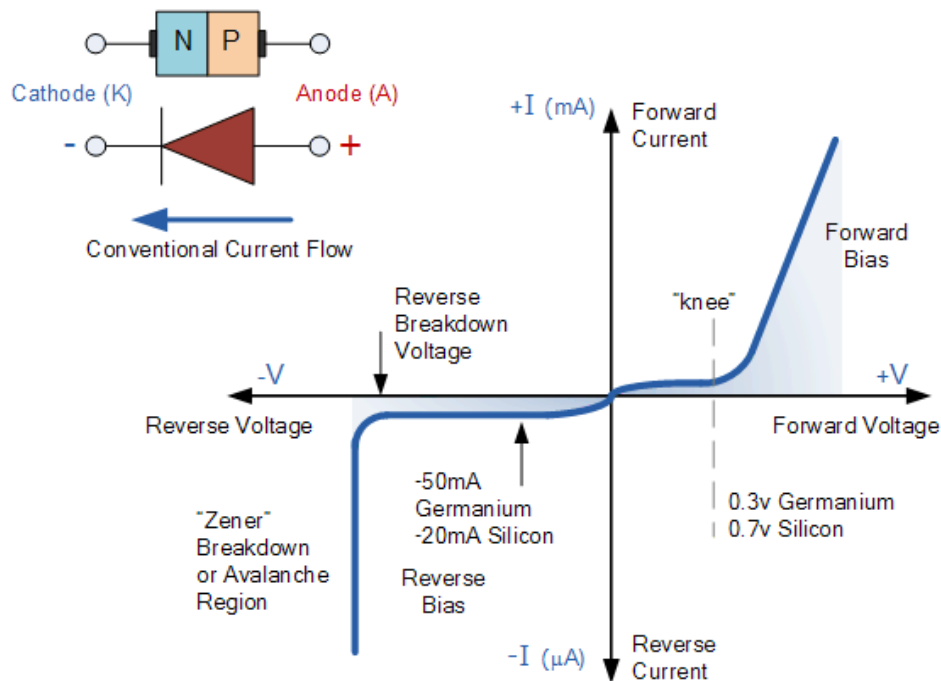


**Figure 5.10:** Electrical (I-V) characteristics of ideal diodes [69].

In the current–voltage characteristics of junction diode as shown Fig.5.10 from the first quadrant in the figure current in the forward bias is incredibly low if the input voltage applied to the diode is lower than the threshold voltage ( $V_r$ ). The threshold voltage is additionally referred to as cut-in voltage. Once the forward bias input voltage surpasses the cut-in voltage (0.3 V for germanium diode, 0.6-0.7 V for silicon diode), the current spectacularly increases, as a result the diode functions as short-circuit.

The reverse bias characteristic curve of diode is shown in the fourth quadrant of the figure above. The current in the reverse bias is low till breakdown is reached and therefore the diode looks like as open circuit. When the reverse bias input voltage has reached the breakdown voltage, reverse current increases spectacularly [69].

The current through a diode as a function of voltage is expressed by the diode equation. The Ideal Diode Law (Shockley's equation), expressed as (5.1):

$$I = I_0(e^{(qV/nk_B T)} - 1) \quad (5.1)$$

where,  $I$  is the net current flowing through the diode;  $I_0$  is the dark saturation current, (the diode leakage current density in the absence of light);  $V$  is the applied voltage though the diode;  $q$  is the absolute value of electron charge ( $1.6 \times 10^{-19}$  C);  $n$  is the ideality factor;  $k_B$  is the Boltzmann's constant ( $1.38 \times 10^{-23}$  J/K);  $T$  is the absolute temperature in Kelvin [72].

If we take the log of both sides of the equation 5.1;

$$\ln I = \ln I_0 + (q/nk_B T)V \quad (5.2)$$

ideality factor,  $n$ , is found to be by equation (5.3);

$$n = q/(k_B T) (dV/d \ln(I)) \quad (5.3)$$

The "dark saturation current" ( $I_0$ ) is an extremely important parameter which differentiates one diode from another.  $I_0$  is a measure of the recombination in a device. A diode with a larger recombination will have a larger  $I_0$ . The value of the ideality factor of the heterojunctions can be determined from the slope of the straight line region of the forward bias log I-V characteristics [72].

$I_0$  is given by equation (5.4);

$$I_0 = BT^3 \exp(-E_g/nk_B T) \quad (5.4)$$

where  $E_g$  is the band-gap energy and  $B$  is the material constant [73].

### 5.1.2.1. Effect of temperature on diode characteristics

The Shockley's equation expressed as equation (5.5):

$$I = I_o(e^{(V_D/nV_T)} - 1) \quad (5.5)$$

Consider the term  $V_T$  given in above equation (5.5). This term is called thermal voltage and is dependent on temperature by the relation  $V_T = k_B T/q$ , where  $k_B$  is Boltzmann's constant,  $q$  is the charge on an electron and  $T$  is the temperature in Kelvin. This term indirectly suggests the dependence of diode characteristics on temperature [74].

The characteristics curve of a Si diode shifts to the left at the rate of -2.5 mV per degree centigrade change in temperature in forward bias region.

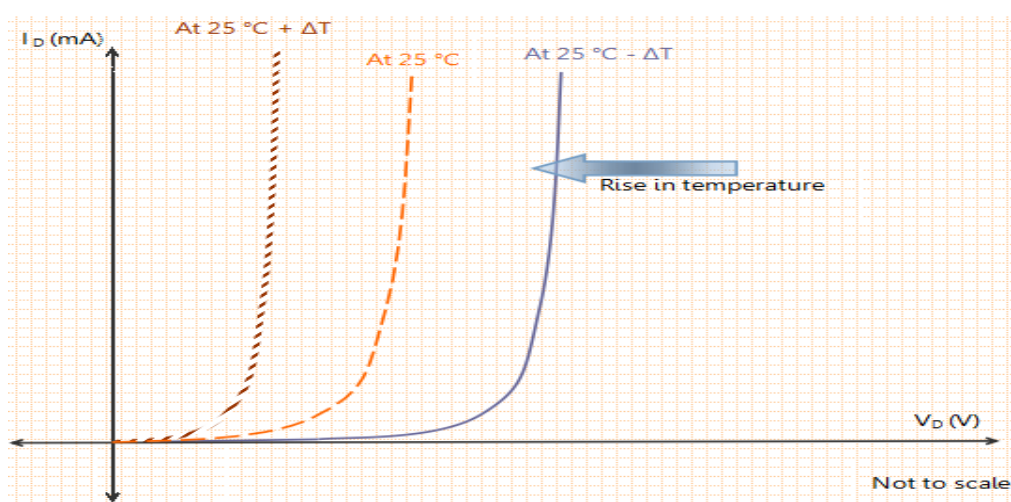


**Figure 5.11:** Effect of temperature on forward characteristics [74].

Refer to the graph as shown Fig. 5.11. The curves are shown far apart just for illustration purpose and are not to scale. The curve shifts to the left at the rate of -2.5 mV per degree centigrade change in temperature. Hence if the temperature increases from room temperature (25°C) to 80°C, the voltage drop across the diode will be  $(80-25) \times 2.5 \text{ mV} = 137.5 \text{ mV}$ .

In the reverse bias region, the reverse saturation current of Si and Ge diodes doubles for every 10°C rise in temperature. A graph showing the variation of reverse saturation current with temperature is shown Fig. 5.12. The difference between the curve is exaggerated for illustration purpose [74].

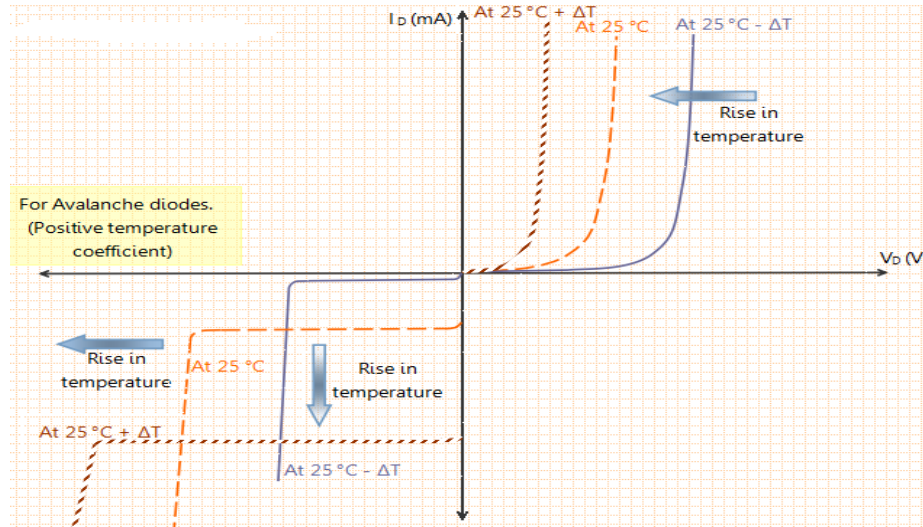


**Figure 5.12:** Effect of temperature on avalanche diodes [74].

From the above graph, it is clear that the reverse saturation current increases with increase in temperature. The graph also shows how the reverse breakdown voltage changes with temperature. It is indicated in the above graph that the reverse breakdown voltage increases with an increase in temperature. However, it is only true for avalanche diodes [74].

### 5.1.3. C-V Measurement of P-N junction diode

Capacitance-voltage (CV) testing is a technique widely used to characterize semiconductor materials and devices and for the extraction of their physical parameters. The basic principle is to apply a varying voltage to a metal-insulator-semiconductor (MIS) or a Schottky junction and to measure the capacitance of the junction. The relationship between the measured capacitance and the applied voltage is then used to derive much relevant information about physical properties of the device under test (DUT).

This method is particularly used in the industry and in the research field for MOSCAP and MOSFET devices. However, a large variety of semiconducting devices can be characterized by C-V measurements including Bipolar Junction Transistors, Junction Field Effect Transistors, III-V compound devices, photovoltaic devices, MEMS devices, organic field effect transistors displays, photodiodes, carbon nanotubes and silicon nanowires.

A C-V measurement system has many important qualities that make it a valuable support and a necessary tool in many activities related to the IC industry and

nowadays increasingly also in the photovoltaic (PV) field. This type of electrical measurement is an effective way to gather informations about materials and devices. Furthermore, they are easy and fast to perform and are flexible enough to be used for different kinds of investigation. As an additional advantage, a C-V measurement system is considerably cheap compared to other material characterization equipment [75].

The capacitance measurements are performed in the dark at room temperature at frequency of 100 kHz under applied forward and reverse DC bias sweeps (-10 to 10V= with an ac oscillation level of 0.5 mV).

The C-V characteristic is described by the conventional heterojunction theory (5.6):

$$C^2 = [(qN_D N_A \epsilon_1 \epsilon_2) / 2(\epsilon_1 N_D + \epsilon_2 N_A)] * [1 / (V_{bi} - V)] \quad (5.6)$$

Here,  $N_D$  and  $N_A$  are donor density in n-ZnO and acceptor density in p-Si, and  $\epsilon_1$  and  $\epsilon_2$  are dielectric constants of n-ZnO and p-Si, respectively and  $V$  is the applied voltage [76].

For an applied reverse voltage  $V \gg k_B T/q$ , and knowing that  $N_A \gg N_D$ , the relationship between the depletion layer capacitance per unit area and the applied voltage is given by equation (5.7) :

$$1/C^2 = [2(V_{bi} - V) / (q\epsilon_s N_d)] \quad (5.7)$$

where  $V_{bi}$  is the built-in potential,  $\epsilon_s$  is the semiconductor permittivity and  $N_d$  its doping level. Assuming a uniform doping level in the semiconductor, the plot of  $1/C^2$  vs.  $V$  is a straight line, of which the intercept with the voltage axis gives the value of the built-in or diffusion potential. The slope of the straight line gives the ionized donor concentration as shown Fig. 5.13 [76].



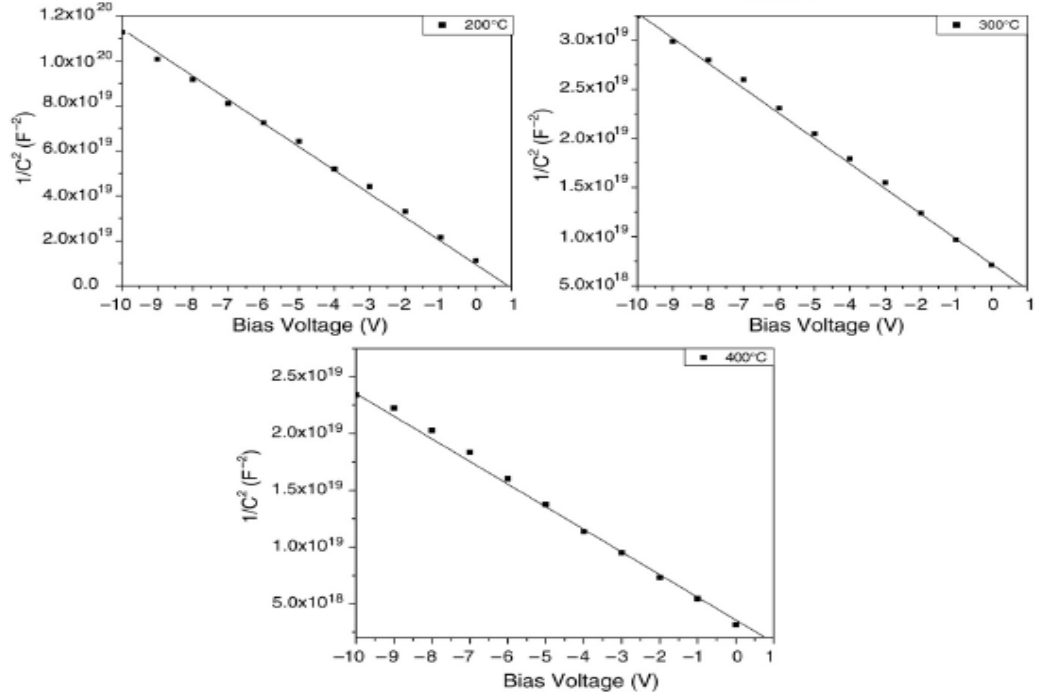


**Figure 5.13:**  $1/C^2$  vs.  $V$  bias for ZnO films grown at different substrate temperatures [76].

The barrier height is given by the following equation (5.8) ;

$$\Phi = V_{d0} + [(k_B T/q) \ln(N_c / N_D)] \quad (5.8)$$

The diffusion voltage zero bias,  $V_{d0}$ , is equal by equation (5.9) ;

$$V_{d0} = V_{bi} + (k_B T/q) \quad (5.9)$$

where  $k_B T/q \ln( N_c/N_D )$  represents the depth of the Fermi level below the conduction band in the neutral region of the semiconductor.  $N_c$  represents the effective density of states (DOS) in the conduction band of the semiconductor.

The barrier height estimated from the extrapolated intercept of  $1/C^2$  with the voltage axis is about 0.8 eV as shown Table 5.1 [76].

**Table 5.1:** Built-in potential, donor concentration and barrier heights for ZnO films grown at different substrate temperatures [76].

Substrate temperature (°C)	$V_{bi}$ (V)	$N_D$ (cm <sup>-3</sup> )	$\Phi$ (eV)
25	0.9	$6.00 \times 10^{17}$	0.93
100	0.6	$8.62 \times 10^{16}$	0.68
200	0.8	$1.03 \times 10^{19}$	0.76
300	0.8	$2.60 \times 10^{18}$	0.79
400	0.7	$1.21 \times 10^{17}$	0.77

#### **5.1.4. Properties of ZnO/Si heterojunction**

Transparent conducting oxides (TCOs) based on ZnO are promising for application in thin film solar photovoltaic cells (PVCs) and various optoelectronic devices. Desired parameters of ZnO and doped ZnO:Al (AZO) thin films are given by their role in superstrate configuration of tandem Si solar cell: the light enters the cell through the glass substrate where two pin absorber thin-film structures are placed between two TCO layers with back metal contact. The upper front contact ZnO:Al layer should fulfill several important requirements: high transparency in VIS/near IR solar spectrum; high electrical conductivity; suitable surface texture in order to enhance light scattering and absorption inside the cell; high chemical stability and adhesion to silicon. Moreover, bottom ZnO interlayer between Si and metal (usually Ag) contact is acting as barrier and adhesion layer as well as optical matching layer to Ag back contact to improve its reflection of radiation, particularly in near IR region. Optimization of the front contact TCO has proven to be crucial for getting the high cell efficiency [77].

##### **5.1.4.1. Structural properties of ZnO/Si heterojunctions**

Lupan et al [78] have reported the successive chemical solution deposition (SCSD) method to deposit adherent and uniform nanocrystalline ZnO films on Si wafer. The effects of Al dopant concentration as well as the effect of rapid photo-thermal processing (RPP) temperature on structure, morphology and photoluminescence (PL) characteristics of deposited ZnO films are investigated. The XRD spectra of as-grown pure ZnO films, ZnO-doped with 1.0 and 2.0 at % Al, are represented in Fig. 5.14 by curves a), c), and e). The influence of RPP on the XRD pattern is also studied and presented by curves b) and d) in Fig. 5.14. The peaks of hexagonal wurtzite-type ZnO (space group:  $P6_3mc$  (186);  $a = 0.3249$  nm,  $c = 0.5206$  nm) structure are present. All diffraction results are in agreement with the JCPDS 036-1451 card for ZnO. The intensity of peaks relative to the background signal demonstrates a high crystalline quality of the ZnO hexagonal phase of the products grown by SCSD and RPP. From Fig. 5.14 the increase in the intensity of XRD signals in the investigated samples can be observed. Through the variation of the duration of maintenance in aqueous solutions during the four-step SCSD process, one can improve the crystallinity and tune the physical properties of the films. It was observed a de-orientation of crystal growth from the (002) direction with the increase

of Al-doping concentration from 1.0 to 2.0 at %. The mean crystallite grain size of nanostructured ZnO samples was calculated using Scherrer's formula. This mean grain size determined from the XRD line broadening is 240Å and 224Å for undoped ZnO and Al-doped ZnO films, respectively. The crystallite sizes were nearly the same for ZnO films before and after RPP, which is in agreement with previous results of Al-doped ZnO. The  $d_{hkl}$  parameter was deduced from the XRD pattern. The mean values are  $a = 3.253$  Å and  $c = 5.209$  Å, which are in accordance with the previously reported results.

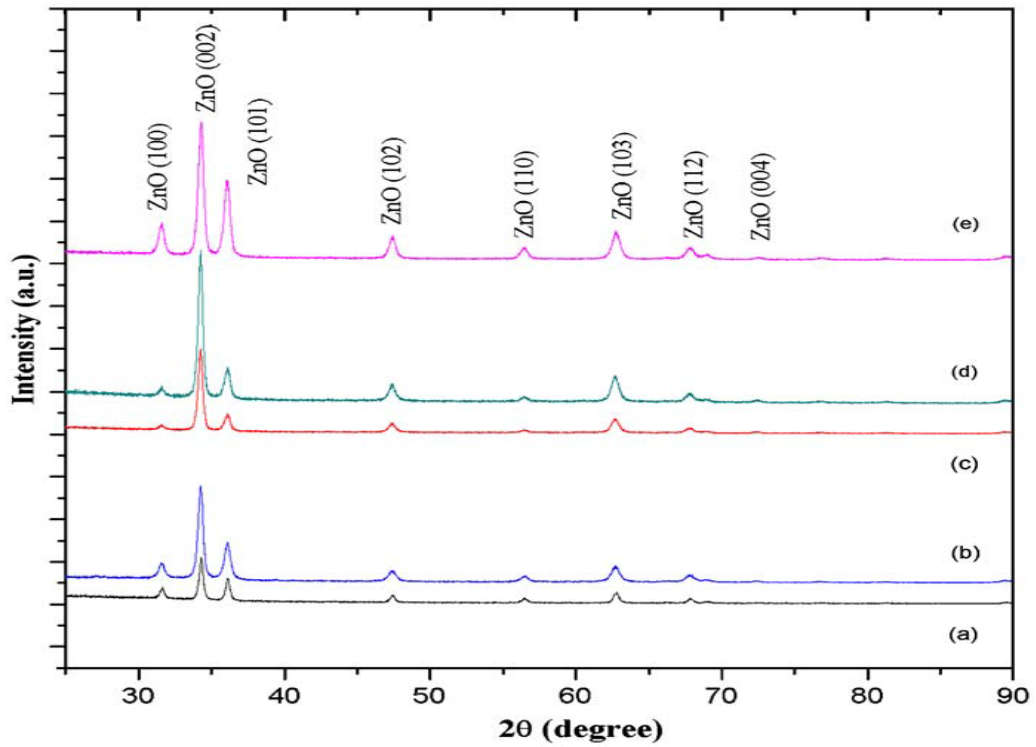


**Figure 5.14:** The XRD pattern of ZnO films with Al doping concentration of a) as-grown pure ZnO films, b) pure ZnO films after RPP at 650 °C, c) 1 at% Al ZnO films as- grown, d) 1 at% Al ZnO films after RPP at 650 °C, and e) 2 at% Al ZnO films after RPP at 650 °C [78].

Fig. 5.15 shows the effect of Al doping on the morphologies of nano structured ZnO films on silicon substrate. The morphology of pure ZnO films is presented in Fig. 5.15a. The increase in Al concentration up to 1.0 at % reduces the average nano particle dimension to about 100 nm as shown Fig. 5.15b and increases the aspect ratio in comparison to pure ZnO films (0.0 at% Al). The increase in Al doping from 1 to 6 at % leads to the increase of particle size as shown Fig.5.15c and d. Fig. 5.15c shows the SEM image of 4 at % Al-doped ZnO films after RPP at 650 °C, 20s. Fig. 5.15d presents the morphology of the 6 at % Al-doped ZnO film. The

increase in doping with Al of ZnO films from 4 at % to 6 at % not only leads to the increase of particle size as shown Fig. 5.15c and d but also leads to the change in film structure. This behavior can be explained in terms of segregation of Al content in to the grain boundaries. At the same time, the independence of surface morphology of RPP temperature up to 650 °C was observed from SEM for pure and Al-doped films [78].

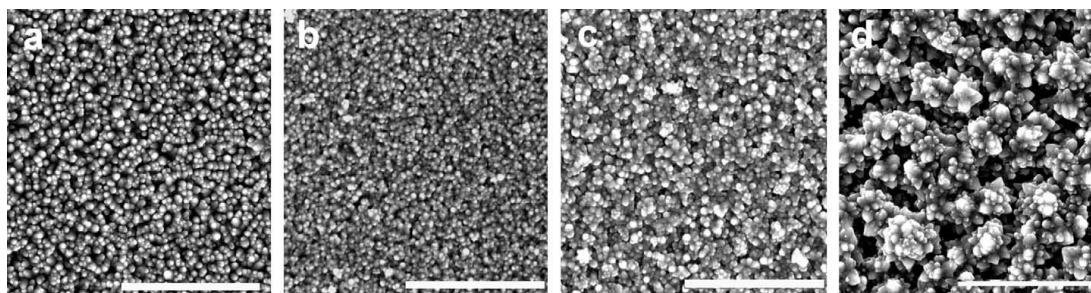


**Figure 5.15:** Secondary electron micrographs of undoped and doped ZnO films onto glass substrates showing the influence of doping and RPP annealing on surface morphology: a) undoped as-grown film, b) as-grown 1 at% Al-doped ZnO, c) 4 at% Al-doped ZnO after the RPP 650 °C, 20s, and d) 6 at% Al- doped ZnO. The scale bar is 10  $\mu\text{m}$  [78].

Park et al [79], ZnO:Al thin films were deposited on Si substrates by employing the RF magnetron sputtering technique. In this study, they investigate the thermal effects of ZnO:Al thin films on glass substrates as a function of the deposition temperature with low oxygen pressure. In order to provide the best condition for applying the ZnO:Al electrode to the optoelectronic device, the structural, optical, and electrical properties are also examined in this paper. A 2 wt % target of Al-doped ZnO was used to deposit. The sputtering system was pumped down to  $4 \times 10^{-6}$  Torr by using a rotary pump and a turbo molecular pump. The working pressure was  $1 \times 10^{-2}$  Torr. The surface morphology was studied by using a scanning electron microscope (SEM) and an atomic force microscope (AFM).

The surface properties of the ZnO:Al thin films can affect electrical and optical properties and characteristics of the optical devices, it is very important to investigate the surface morphology of ZnO:Al thin films. Fig. 5.16 shows SEM surface micrographs of ZnO:Al films prepared at various deposition temperatures. As the deposition temperature increased, the grain size increased and the surface roughness decreased. These results, in agreement with the XRD analysis, indicated that the diffusion probability of ZnO and Al atoms on the surface can be controlled by the deposition temperature. A higher temperature enhances the occupation probability of

Al ions on Zn sites, as well as oxygen vacancies and Zn interstitial atoms. In other words, Al atoms can diffuse to the surface, dependent upon the deposition temperature. An increase in crystalline size would be strongly related to a decrease in resistance for free electrons, because of lower grain and grain-boundary scattering. At higher temperatures, cracks were observed in the ZnO:Al films, and the formation of cracks probably originated from the different thermal expansion coefficients of the films and substrates [79].

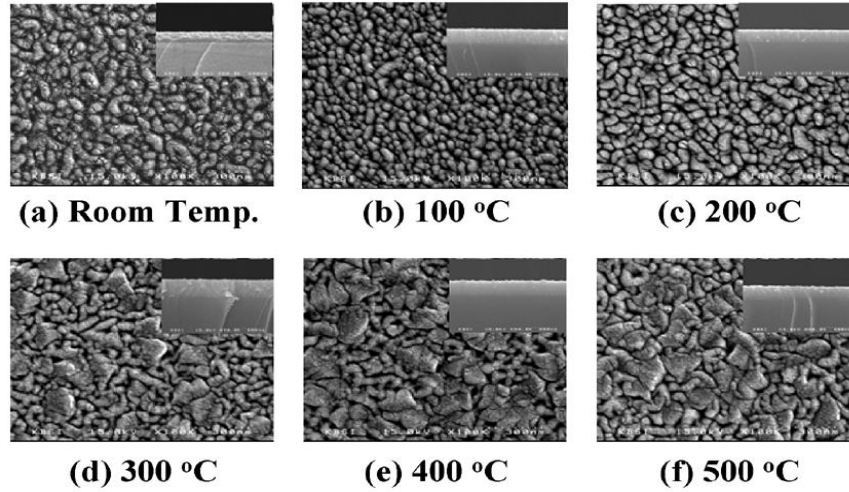


**Figure 5.16:** Scanning electron micrographs of ZnO:Al thin films at different deposition temperatures [79].

The average grain size of ZnO:Al films was checked by AFM images ( $1\ \mu\text{m} \times 1\ \mu\text{m}$ ) at different substrate deposition temperatures as shown in Fig. 5.17. As they can see from Fig. 5.17, the surface was very flat and no very sharp peak appears in the domain. ZnO:Al film deposited at RT had an average grain size of 3.29 nm, and for a sample deposited at 500 °C was 15.03 nm. For all samples, the average grain size was in the range from 3.29 nm to 15.03 nm. They also measured surface roughness of the ZnO:Al thin films. It can be seen that the rootmean-square (RMS) roughness of the thin film increases with increasing deposition temperature. The RMS value of RT-deposited ZnO:Al was 1.38 nm, whereas the RMS value of AZO thin film deposited at 500 °C was 4.66 nm. Increasing the deposition temperature made the surface roughness larger. The larger values of the grain size also influenced the increasing RMS value of the samples [79].

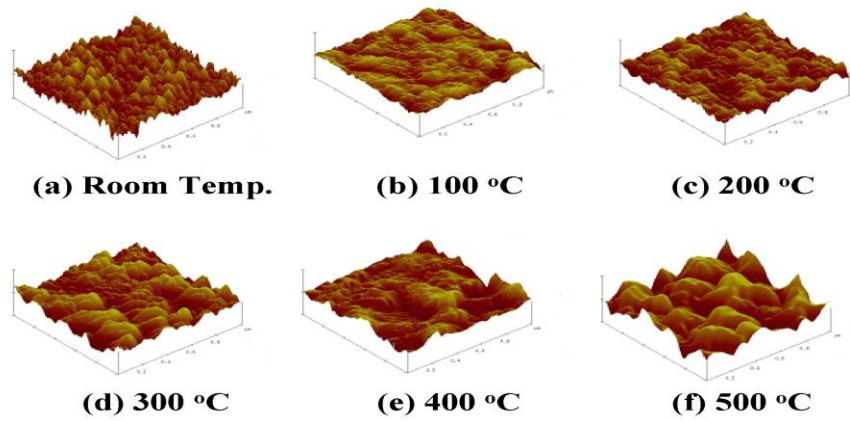
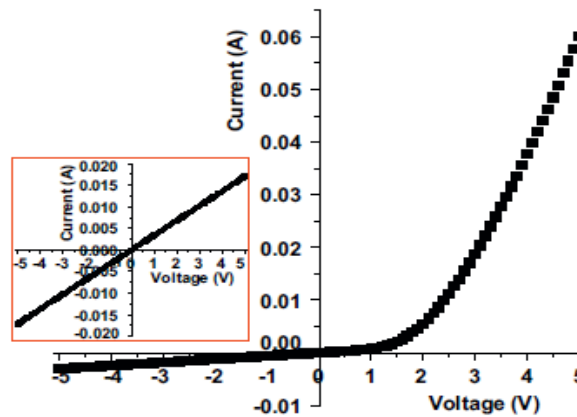


**Figure 5.17:** AFM images of ZnO:Al films at different deposition temperatures [79].

#### 5.1.4.2. Electrical properties of ZnO/Si heterojunctions

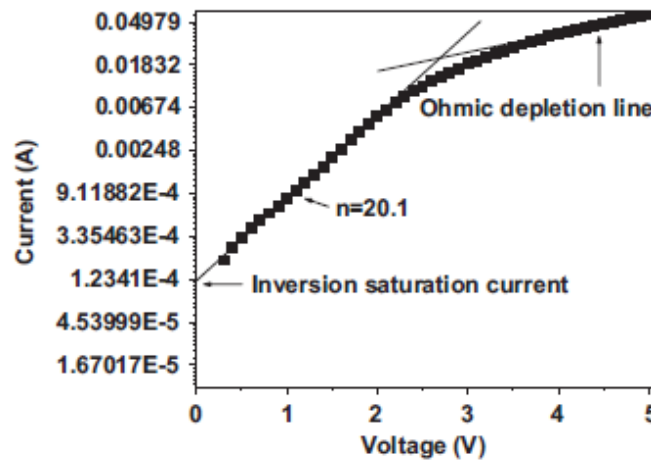
Bo et al [72] have studied I-V characteristics of ZnO:Al /p-Si heterojunction at room temperature in the dark. The electrical properties of films were characterized by four-point probe and Hall effect measurement (Accent HL5500 pc). The current-voltage (I-V) characteristics of the device were measured by Agilent 4155C semiconductor parameter analyzer. In this work, Al doped ZnO film (AZO) was deposited by direct-current (DC) magnetron sputtering on p type single crystal Si wafer as a practical photo-window for Si photoelectric device, and also as a semiconducting layer, which causes a depletion region and a built-in barrier potential in the heterojunction, because the work function of ZnO:Al is 4.2 eV lower than the work function of p-Si.

Fig. 5.18 shows the current-voltage characteristic of the ZnO:Al /p-Si heterojunction measured at room temperature under the dark. The ohmic contacts of Cu metal on ZnO:Al layer are confirmed by the good linear I-V dependences (see inset Fig. 5.18). The I-V curves of devices show good rectifying behaviors.



**Figure 5.18.:** I-V curve of the ZnO:Al /p-Si heterojunction device under dark [72].

A plot of  $\ln I$  against  $V$  is shown in Fig.5.19, which indicates that the current at low voltage ( $V < 2V$ ) varies exponentially with voltage. The characteristics can be described by the stand diode equation.  $I_0$  and  $n$  can be calculated from the measurements in Fig.5.19. The value of the ideality factor of the ZnO:Al/p-Si heterojunction is determined from the slope of the straight-line region of the forward bias log I-V characteristics. At low forward bias ( $V < 2V$ ), the typical values of ideality factors and the reverse saturation current are 20.1 and  $1.19 \times 10^{-4}$  A, respectively. The result of calculation using the standard diode equation where  $n=20.1$  and  $I_0 = 1.19 \times 10^{-4}$  A is similar to the measurement I-V curve. At higher voltages the curves deviate from the exponential behavior, which is seen from the flattening of the characteristic curve as shown Fig.5.19, indicating the effect of a series resistance. A simple series resistance model ( $I = I_s e^{(q(V-IR_s)/nkT)}$ ) can be applied in an attempt to linearize the characteristics. The series resistance of ZnO:Al/p-Si heterojunction is  $28.25 \Omega$  and the ratio  $I_F/I_R$  ( $I_F$  and  $I_R$  stand for the forward and reverse current, respectively) at 5 V is found to be as high as 19.7. This shows the good rectifying behavior, indicating formation of a diode between ZnO:Al and p-Si [72].



**Figure 5.19:** Logarithmic scale in current with forward bias condition [72].

The photo I-V characteristics were measured under illumination by a low power white light ( $6.3 \text{ mW/cm}^2$ ) lamp and a 20W halogen lamp and are shown in Fig.5.20. Typical good rectifying and photoelectric behaviors were observed for the device. Under reverse bias conditions the photocurrent caused by ZnO surfaces exposed to low power white light lamp and 20W halogen lamp is obviously much larger than the

dark current. For example, when the reverse bias is -5V, the dark current is only  $3.05 \times 10^{-3}$  A, while the photo current reaches  $4.06 \times 10^{-3}$  and  $6.99 \times 10^{-3}$  A under low power white light and halogen lamp illumination, respectively.

Since, the ZnO:Al film is highly transparent ( $T > 90\%$ ) in the visible region, visible light passes through the ZnO:Al film and is absorbed primarily in the underlying p-Si, generating electron-hole pairs, responsible for the observed photo current under reverse bias conditions. On the other hand, the UV photons are absorbed mainly in the ZnO:Al layer and the photo-generated electrons are drifted towards the positive electrode through the Al-doped ZnO region since the high carrier concentration of ZnO:Al film causes a depletion region and build-in barrier potential almost in the side of p-Si. Consequently, the current increases linearly as the reverse bias increases as shown Fig.5.20. The insert of Fig.5.20 shows that the ZnO:Al /p-Si heterojunction under halogen lamp illumination has an obvious photovoltaic effect. The photovoltage of the heterojunction is 130mV and the short circuit current is 128  $\mu$ A [72].

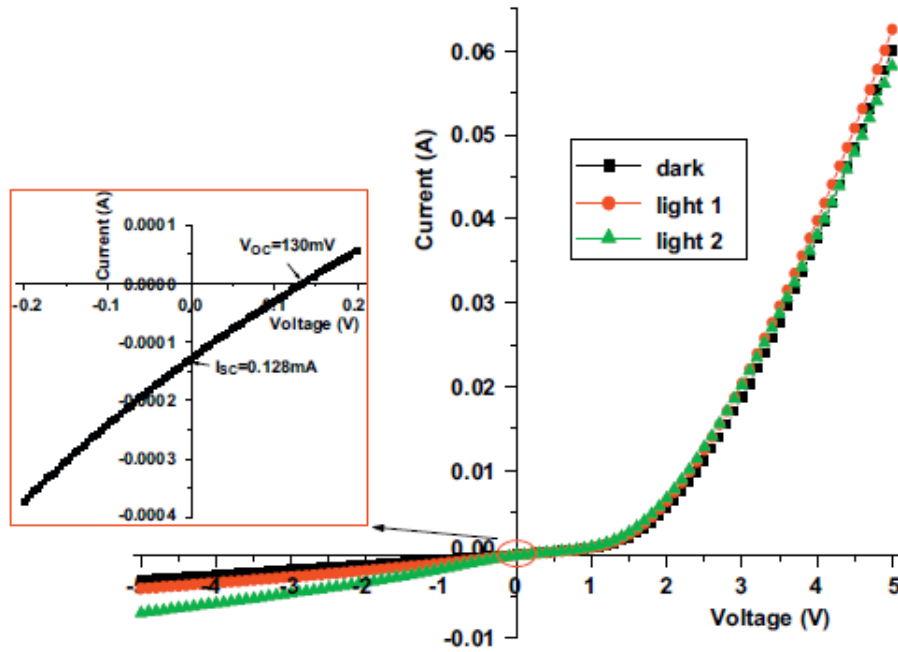


**Figure 5.20:** I-V characteristic of the ZnO:Al/p-Si heterojunction under dark and under light (light 1:  $6.3 \text{ mW/cm}^2$  white light; light 2: 20W halogen lamp [72]).

Zhang et al [80] have studied I-V characteristics of p-Si/n-ZnO heterostructured junctions by using an X-Y function recorder in the temperature range of 207-339 K in the dark. Un-doped nc-ZnO films were prepared on single crystalline p-Si substrates by a sol-gel method. The I-V characteristics were measured by



a laboratory-assembled system consisting of a function generator, an X-Y function recorder, a low-temperature cryostat, and a specially designed sampled holder. Thin films samples are mounted in a specially designed sampled holder.

Fig.5.21 shows the I-V characteristics of nc-ZnO/p-Si heterojunctions measured with temperature ranging from 270 to 339 K in a cryostat. The sample was kept in the dark condition during the measurements. It is obvious from Fig.5.21a that the heterostructures are rectifying in nature with a turn-on voltage of  $\sim 3.0$  V, which is much larger than that of ZnO:Al/n-Si prepared by a magnetron sputtering. Under reverse voltages, the breakdown voltage for the sample is as large as 20 V (not shown in Fig. 5.21). Generally, the native ZnO is n-type semiconductor due to the self-compensation. In the case of ZnO/Si, the work function of p-type Si is larger than that of n-type Si. The potential barrier of p-type Si is higher compared with n-type Si. Therefore, the turn-on voltage of nc- ZnO/p-Si heterojunction is larger in comparison of ZnO:Al/n-Si. Fig. 5.21b shows the temperature dependence of the forward current in logarithmic scale. The forward currents can be classified into two regions according to the applied voltages. In region B, above  $\sim 3.8$  V, the forward current deviates from linearity due to the effect of a series resistance on the system. In region A, below  $\sim 3.8$  V, the temperature dependence of the forward currents can be expressed by equation (5.10);

$$I = I_0 \exp(BV) \quad (5.10)$$

where  $I$  is the current subject to an applied voltage  $V$ ,  $I_0$  the saturation current, and  $B$  is a coefficient. The temperature dependence of the parameter  $B$  depends on the dominant current transport mechanism. If the current is controlled by tunneling,  $B$  is a constant independent of temperature. If the current is controlled by some other mechanisms,  $B$  is generally dependent on temperature. In the plots of  $\log I$  versus  $V$  of nc-ZnO/p-Si heterojunctions,  $B$  is independent of the measurement temperature  $T$ , which indicates that the current in this region is dominated by a tunneling mechanism [80].

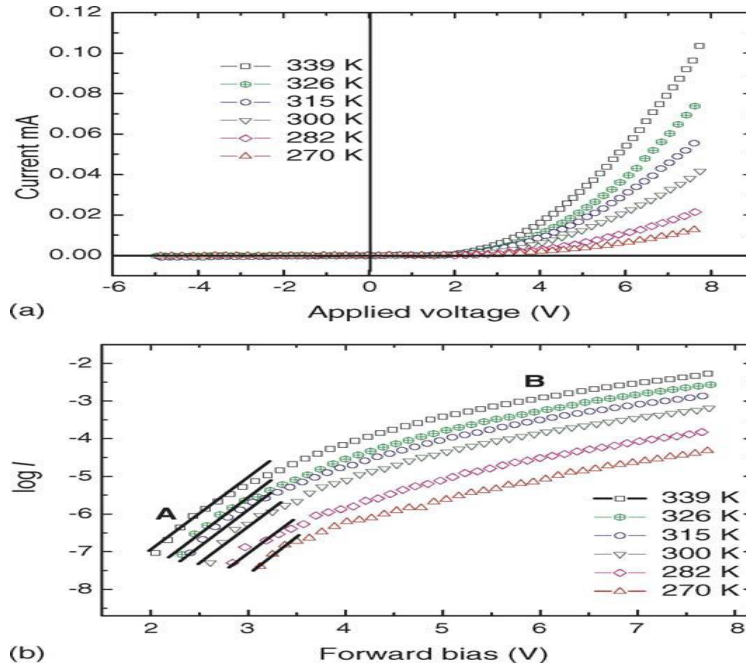


**Figure 5.21:** Current-voltage characteristics of the nc-ZnO/p-Si heterojunctions at various temperatures in dark. The current is plotted as a function of the applied voltage using a linear a) and b) semilogarithmic scale [80].

Song et al [81] have studied current-voltage-temperature measurements ( $J$ - $V$ - $T$  method) of ZnO:Al/n-Si heterostructured junctions forward bias in the dark. The ZnO:Al films were deposited in a radio-frequency (RF) magnetron sputtering system. Before each deposition, the base pressure inside the chamber was pumped down to less than  $1.6 \times 10^{-4}$  Pa. Sputtering was carried out at a working gas pressure ( $P_w$ ) of  $\sim 0.5$  Pa in a pure argon gas with RF power ( $P_{rf}$ ) of 150 W and a substrate temperature ( $T_{sub}$ ) of 250 °C. Low RF power of 30-50 W was used in the initial deposition process (deposition thickness  $\sim 20$  nm) in order to minimise Si wafer surface damage due to energetic particle bombardment from the plasma. Then, the RF power was increased to 150 W to thicken the film to 250-350 nm. No silicon oxide interlayer was intentionally grown between the n-Si wafers and the ZnO:Al films. The current-voltage characteristics of the heterojunctions were measured with an automated measuring system, consisting of a DC voltage-current source/monitor unit (Advantest, TR6143) and a control computer.

Fig.5.22 shows the current-voltage characteristics of a ZnO:Al/n-Si heterojunction measured at room temperature in the dark, demonstrating good rectification. If the forward-biased curve is fitted to the standard diode equation, they find that the ideality factors are 2.7 (for  $V < 0.25$  V) and 1.62 (for  $V > 0.25$  V), respectively. The

turn-on voltage is approximately 0.3 V, in agreement with the turn-on voltage of Si MIS diodes.

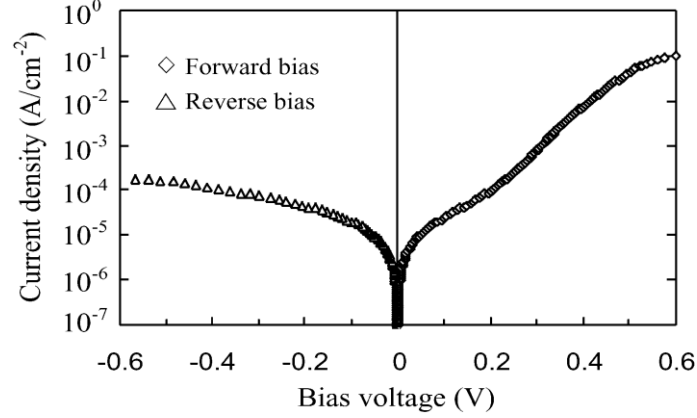


**Figure 5.22.:** Measured current-voltage characteristics of a ZnO:Al/n-Si heterojunction sample [81].

In order to determine the dominant mechanism of carrier transport through ZnO:Al/n-Si heterojunctions, they measured the forward-biased dark current density characteristics as a function of temperature (J-V-T method). Fig.5.23 shows the temperature dependence measured for the dark I-V characteristics of one of they samples in the temperature range 283-363 K. For analysis purposes, consider that, at intermediate voltages, the relationship between forward current density (J) and voltage (V) of a heterojunction is approximately given by equation (5.11):

$$J(V, T) = J_0(T) \exp(AV) \quad (5.11)$$

where A is independent of the voltage, T is the temperature (in K), and  $J_0(T)$  is the reverse saturation current density (which is a function of temperature, depending on the nature of the dominant carrier transport mechanisms in the heterojunction). In general, there are two models for explaining the current transport mechanism through a heterojunction: a) A is temperature-dependent (specifically,  $A = q/nk_B T$ , where q is the electron charge, n is the ideality factor,  $k_B$  is Boltzmann's constant, and  $n=1.0$  for a diffusion-limited model and  $n=2.0$  for a space-charge region recombination-limited model); and b) A is constant (i.e. independent of temperature) for a tunnelling-limited model. The total current density in the dark is the sum of the currents caused by various mechanisms, but one of those is usually dominant in a certain voltage range [81].

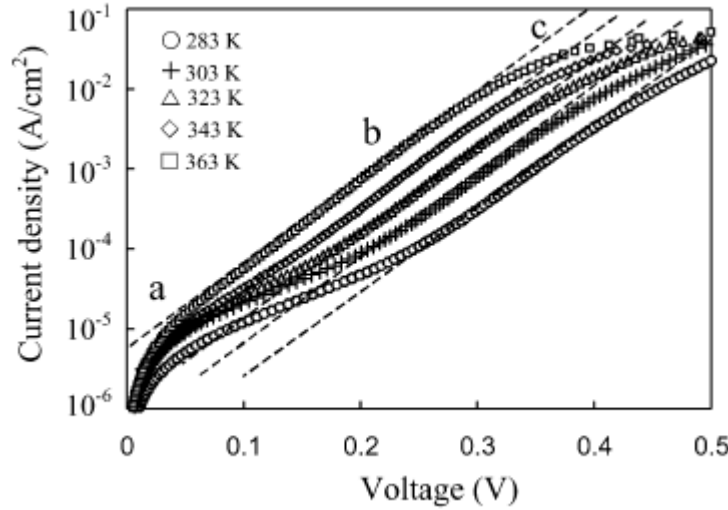


**Figure 5.23:** Measured dark I-V characteristics (forward bias) of a ZnO:Al/n-Si heterojunction sample for temperatures in the range 283-363 K [81].

From Fig. 5.23 it was found that the plots can be approximately divided into three voltage ranges, denoted by a, b and c, respectively. In the low-voltage segment (range a),  $J$  depends strongly on  $T$  and the ideality factor  $n$  reduces from 2.9 to 1.3 when the temperature increases from 283 to 363 K. This suggests that the forward current is mainly limited by recombination within the junction space charge region and/or at the Si interface. The recombination current is proportional to  $\exp(qV/nk_B T)$ .

At intermediate voltages (range b), the feature of almost parallel straight lines for all temperatures (see dashed lines in Fig.5.23) indicates that a different carrier transport mechanism dominates here. If, due to the Schottky barrier-type nature of the ZnO:Al/n-Si devices, they assume that the dominant current mechanism is thermionic emission of carriers across the potential barrier [73].

Li et al [82] have studied I-V characteristics of n-ZnO/p-Si heterojunction by using a source meter (Keithley, 2400). The photocurrent was measured under illumination from a Thermo Oriel 150-W solar simulator with AM1.5G filters with an intensity of  $100 \text{ mW/cm}^2$  or 365-nm UV light with a power intensity of  $8 \text{ mW/cm}^2$ .

Fig.5.24 shows current density-voltage ( $J$ - $V$ ) curves of the n-ZnO/p-Si heterojunction for a ZnO thickness of 550 nm under dark and under illumination by AM1.5G ( $100 \text{ mW/cm}^2$ ) sunlight. As evidenced from the figure, photovoltaic effect is clearly observed under AM1.5G ( $100 \text{ mW/cm}^2$ ) sunlight illumination. The open-circuit

voltage ( $V_{oc}$ ), shortcircuit current density ( $J_{sc}$ ), and fill factor (FF) for the device are 131 mV, 6.7 mA/cm<sup>2</sup>, and 22.8%, respectively. A conversion efficiency ( $\eta_p$ ) of about 0.206% has been achieved in this heterojunction. Typical I-V curves of the heterojunction in the dark and under AM1.5G (100 mW/cm<sup>2</sup>) sunlight illumination are shown in the inset of Fig.5.24. Note that the reverse current of the device under simulated AM1.5G (100 mW/cm<sup>2</sup>) sunlight illumination is larger than that under dark conditions, while the current under forward bias for the two conditions is almost the same. The above phenomenon can be understood as follows: A large number of electron-hole pairs will be generated under the simulated sunlight illumination, and the electrons and holes will be driven toward opposite electrodes with little barrier. As a result, the current for the device under illumination is larger than that under dark. Under forward bias, the electrons and holes will drift to the depletion area and recombine there, so the current is almost the same for the device under sunlight illumination or under dark conditions, as shown in the inset of Fig.5.24.

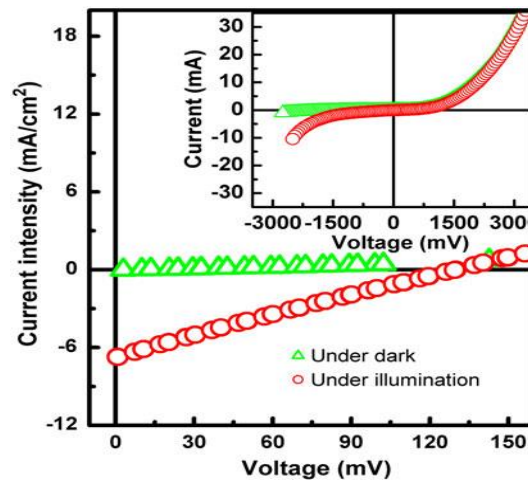


**Figure 5.24:** J-V curve of the heterojunction under dark and under AM1.5G (100 mW/cm<sup>2</sup>) simulated sunlight. The inset shows the I-V curve of the heterojunction under dark and under AM1.5G (100 mW/cm<sup>2</sup>) simulated sunlight [82].

The mechanism for light harvesting in the heterojunction can be understood well in terms of the band alignment. The equilibrium band diagram of the heterojunction derived from the Anderson model is shown in Fig.5.25. The bandgap ( $E_g$ ) and electron affinity ( $\chi$ ) values used are  $E_g(\text{Si}) = 1.12$  eV and  $\chi(\text{Si}) = 4.05$  eV,  $E_g(\text{ZnO}) = 3.37$  eV, and  $\chi(\text{ZnO}) = 4.35$  eV. The carrier concentration in the n-ZnO and p-Si layers measured by Hall measurement is  $2 \times 10^{18}$  cm<sup>-3</sup> and  $1 \times 10^{19}$  cm<sup>-3</sup>, respectively. Based on the carrier concentration data, the Fermi level in ZnO lays 81 meV below

its conduction band, while the Fermi level in Si lays 1.5 meV above its valence band. According to the Anderson model, the conduction band and valence band offsets in the n-ZnO/p-Si heterojunction are 0.3 eV and 2.55 eV, respectively. When the heterojunction is illuminated by sunlight, the majority of the UV photons [with energy  $E > E_g(\text{ZnO})$ ] of the sunlight will be absorbed by the ZnO film due to its large absorption coefficient in this spectral region, and electron-hole pairs will be generated in the ZnO layer. Meanwhile, most of the photons with energy  $E < E_g(\text{ZnO})$  will be transmitted through the n-ZnO film due to its high transparency in the visible and near infrared regions. These transmitted photons will be absorbed by the p-Si, and electron-hole pairs will be generated there in. The built-in electric field in the n-ZnO/p-Si interface will drive the photo-generated holes in the ZnO layer toward the Si side, while the electrons generated in the Si layer will be driven to the ZnO side. As shown in Fig.5.25 the barrier that hinders holes in ZnO from moving toward Si is negligible; simultaneously the barrier that hinders electrons in Si from moving toward ZnO is also negligible. Consequently, electrons and holes are separated at the heterojunction interface, and a photovoltaic effect result [82].

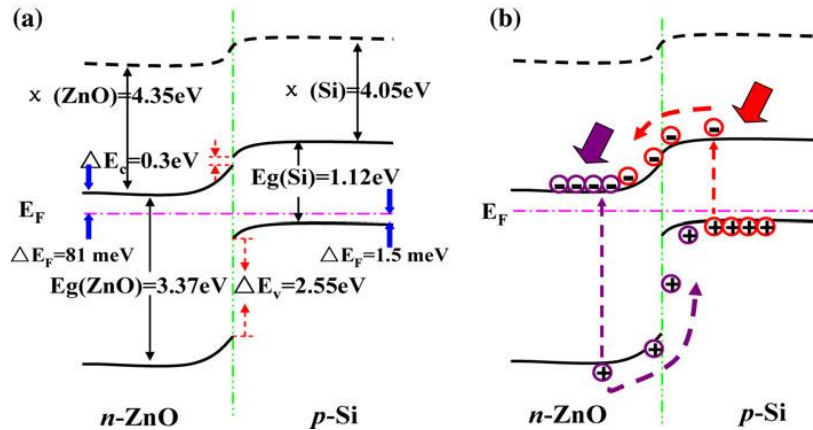


**Figure 5.25:** Band diagrams of the n-ZnO/p-Si heterojunction under dark a) and under solar illumination b) [82].

Romero et al [83] have studied the electrical, structural and compositional properties of the junctions of both pure and Al (1 at. %) doped thin films of ZnO on p- and n-type silicon, as obtained by chemical spray pyrolysis. Electrical properties were determined by admittance spectroscopy using a Broadband Dielectric Converter (BDC) from Novocontrol with a Solartron 1255 Frequency Response Analyzer (FRA) for a frequency range between 1Hz and 1MHz. The n-ZnO/p-Si

heterojunction was placed in a Novocontrol sample holder modified in our laboratory; the ohmic contact with the p-Si substrate was performed with Al and with the n-Si with In–Ga. The temperature range was between 223 and 373 K, and was controlled by a Quatro temperature controller from Novocontrol.

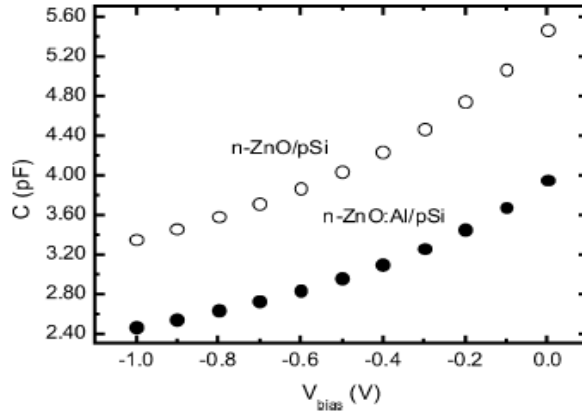


**Figure 5.26:** C-V characteristics in the reverse bias region at 300K for the n-ZnO:Al/p-Si and n-ZnO/p-Si heterojunctions at 1MHz [83].

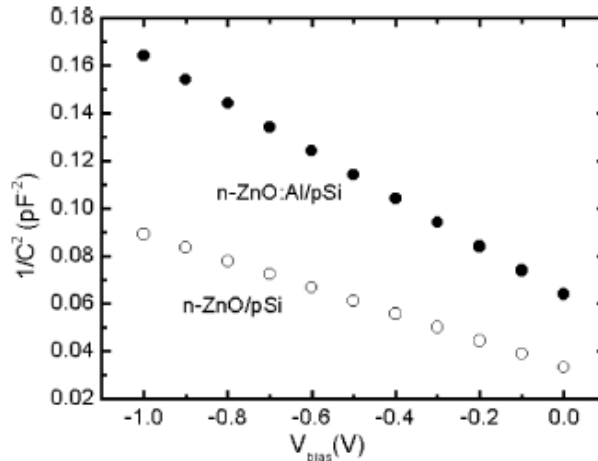


**Figure 5.27:**  $C^{-2}$ -V bias relationship for the n-ZnO:Al/p-Si and n-ZnO/p-Si heterojunctions at 1MHz [83].

The potential barrier at the junction can be measured by small-signal capacitance - voltage (C-V) characteristics. Fig.5.26 presents the C-V characteristics in the reverse bias region at 300K for the n-ZnO:Al/p-Si and n-ZnO/p-Si heterojunctions at 1 MHz. As can be seen, the capacitance of the heterojunction is decreased with an increase in the reverse bias with an approximately linear  $C^{-2}$  -V bias relationship as shown Fig.5.27. This means that the depletion region in the vicinity of the heterojunction interface is expanded with an increase in the reverse bias. This C-V characteristic is also described by the conventional heterojunction theory (5.12):

$$C^2 = [(qN_D N_A \epsilon_1 \epsilon_2) / 2(\epsilon_1 N_A + \epsilon_2 N_D)] * [1 / (V_b + V_D)] \quad (5.12)$$

Here,  $N_D$  is the donor density in n-ZnO,  $N_A$  the acceptor density in p-Si,  $\epsilon_1$  and  $\epsilon_2$  are the dielectric constants of n-ZnO and p-Si, respectively, and  $V_b$  is the applied voltage. Using this formula, they can determine the effective space charge density of the depletion region of both heterojunctions from the slope of the  $C^{-2}(V_b)$  relationship [83].

**Table 5.2:** Characteristic parameters of p-n junction [83].

	n-ZnO/p-Si	n-ZnO:Al/p-Si	n-ZnO/n-Si	n-ZnO:Al/n-Si
$N_D$ ( $m^{-3}$ )	$5 \times 10^{23}$	$9 \times 10^{23}$	$5 \times 10^{23}$	$9 \times 10^{23}$
$V_b$ (eV)	0.66	0.70	0.50	0.56
$W$ (nm)	34	26	30	24

The values obtained are presented in Table 5.2 for  $\epsilon_r(\text{ZnO}) = 8$  and  $\epsilon_r(\text{Si}) = 12$ . The values obtained for  $N_D$  in n-ZnO:Al 1 at.% ( $9 \times 10^{23} m^{-3}$ ) and n-ZnO ( $5 \times 10^{23} m^{-3}$ ) are higher than for  $N_A$  in p-Si, where  $N_A$  is estimated to be about  $8 \times 10^{20} m^{-3}$  from the resistivity of p-Si ( $9 \Omega^{-1} \text{ cm}$ ). These results indicate that the junction is an abrupt p-n type junction. The built-in potential  $V_D$ , or diffusion potential, is estimated to be 0.66 and 0.7 eV for the ZnO:Al/p-Si and ZnO/p-Si junctions, respectively. This result is consistent with the energy difference between the work functions of Si and ZnO. The Fermi level below the vacuum level is 4.97 eV for p-Si, and 4.25 eV for n-ZnO. The difference between them is 0.72 eV. The results obtained for n-ZnO/n-Si are very similar (not shown here). The built-in potential is 0.56 eV for the n-ZnO:Al junction (1 at. %)/n-Si and 0.50 for the ZnO/n-Si. Fig.5.28 shows the band diagram for the n-ZnO/p-Si and the n-ZnO/n-Si junctions. Table 5.2 presents the most important values.

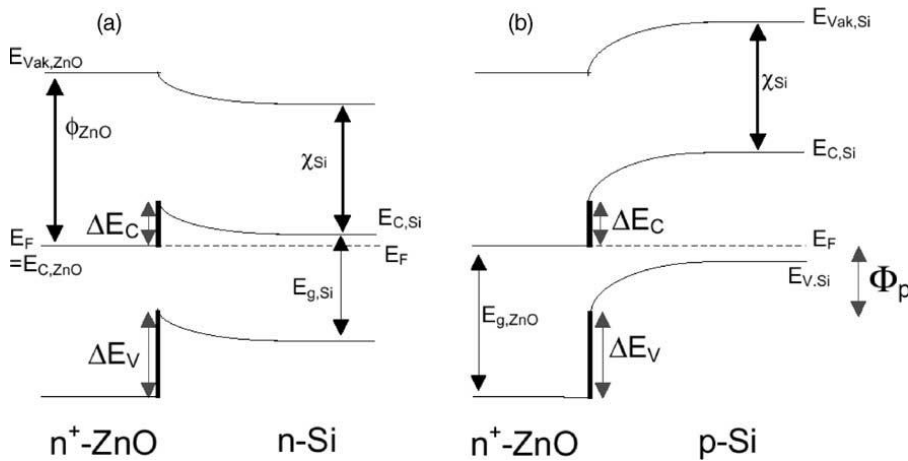


**Figure 5.28:** Band diagram for the n-ZnO/p-Si and the n-ZnO/n-Si [83].



The most likely reason for a more complex behavior (n-ZnO:Al/p-Si and n ZnO:Al/n-Si), compared to the model of a simple p–n heterojunction, are the defects at or near the n-ZnO:Al/c-Si interface, which cause a Fermi energy pinning. The pinning effect makes the height of the energy barrier independent of the ZnO work function. The Fermi energy at metal/n-semiconductor interfaces is often pinned at about  $E_g/3$ . In the case of Si ( $E_g=1.12$  eV), this corresponds to 0.37 eV above the valence band edge. Making this assumption, the energy barrier at the interface seen by the free electrons in  $9\Omega^{-1}$  cm p-Si is 0.53 eV, which is quite consistent with their  $1/C^2$ -V measurements (0.56 eV) [83].

Zhang et al [80] were performed C-V characteristics of p-Si/n-ZnO heterostructured junctions by CTG-1 model high frequency C-V characteristics measurement apparatus (Shanghai third electronics apparatus factory) at room temperature, where the input voltage frequency was fixed at 1 MHz with a sweeping rate of 0.2 V/s at room temperature. The Ohmic contacts to ZnO layers forms through the fusion of indium alloy. From careful check, metal contacts were of adequate non-rectification.

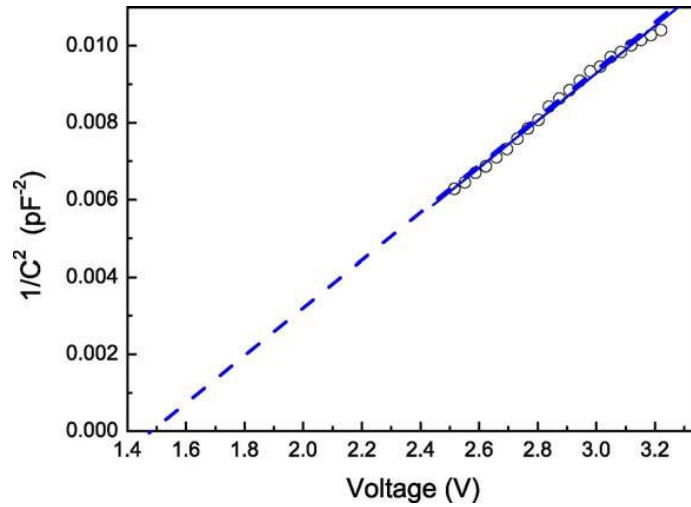


**Figure 5.29:**  $1/C^2$  versus voltage plot of an nc-ZnO/c-Si heterojunction measured at 1 MHz in dark [80].

Fig.5.29 shows a typical C-V relation obtained from the formed nc-ZnO/p-Si heterojunctions measured at a high frequency of 1 MHz under dark and at room temperature. As observed from the figure,  $1/C^2$ -V variation is linear in the voltage range studied, indicating that there is little number of deep levels. The typical features of an n-type metal oxide semiconductor capacitor with an accumulation region are observed, indicating that the junction is abrupt. The variation of capacitance as the bias decreases is caused by changes of the thickness of the carrier

depletion region. The straight lines extrapolated to  $1/C^2 = 0$  give the value of built-in potential  $V_{bi} = 1.49\text{V}$ , which is quite large compared with the reported value for sputtered ZnO:Al/Si 0.56 V. The discrepancy is due to the different interface state densities at the heterojunction interfaces. The difference of built-in potential indicates on a different interface state density at the heterojunction interface or composition and strain. In nanocrystalline ZnO films, the ratio of volume to surface is larger than that of columnar films, and the strain in nanocrystalline films is smaller than that of columnar films. Moreover, the conduction type of substrates and Al dopant are different. These induced the different interface state density at the heterojunction interface. Therefore, the built-in potentials of nc-ZnO/p-Si is larger than that of ZnO:Al/n-Si heterojunctions.

Moreover, it should be noted that  $qV_{bi}$  ( $q$  the electronic charge) obtained from C-V data is larger than the activation energy  $E_a$  got from I-V data. Though the value of  $qV_{bi}$  is close to the activation energy, the forward current in heterojunctions is determined by the thermionic emission of carriers over a potential barrier of  $qV_{bi}$ . In the nc-ZnO/p-Si heterostructures, the  $qV_{bi}$  obtained from the C-V plot is larger than the activation energy got from the temperature dependence of the saturation current. Thus tunneling seems to be an important factor in determining the current flow mechanism. This result further supports the tunneling mechanism of the nc-ZnO/p-Si heterostructures [80].

#### **5.1.4.3. Production techniques of ZnO/Si heterojunctions**

There are a few reports on the n-ZnO/p-Si heterojunction where the ZnO film is grown by different techniques. For example, the electrical characteristics of n-ZnO/p-Si heterojunction diodes grown by pulsed laser deposition at different oxygen pressures. ZnO/p-Si junction was prepared by CVD and an ideality factor was 2.57. The characterization of sol-gel derived yttrium-doped n-ZnO/ p-Si heterostructure was studied. UV electroluminescence (EL) emission from ZnO nanorods with n-ZnO/p-Si heterojunction structure was fabricated by the hydrothermal method [72].

## 6. EXPERIMENTAL PROCEDURE

This study covers production and characterization of the Al doped ZnO thin films deposited on p type silicon wafers by sol-gel dip coating method. The films were deposited to produce p-n heterojunction. The heterojunction were generated between p- type silicon wafers and n- type ZnO:Al thin films by sol-gel dip coating process.

The films had been prepared by the stages of sol preparation; substrate cleaning, dip coating, pre-heating and post heating multiprocessing. The procedure from coating to drying was repeated four times as shown Fig.6.1. The pre-heat treatments were performed at 400°C in air and post heating treatments in 550-800°C for 1 h in air and vacuum. Heat treatment parameters, Al doping concentration and coating process parameters effects on electrical, structural properties of ZnO:Al films and ZnO:Al/p-Si heterojunctions were investigated.

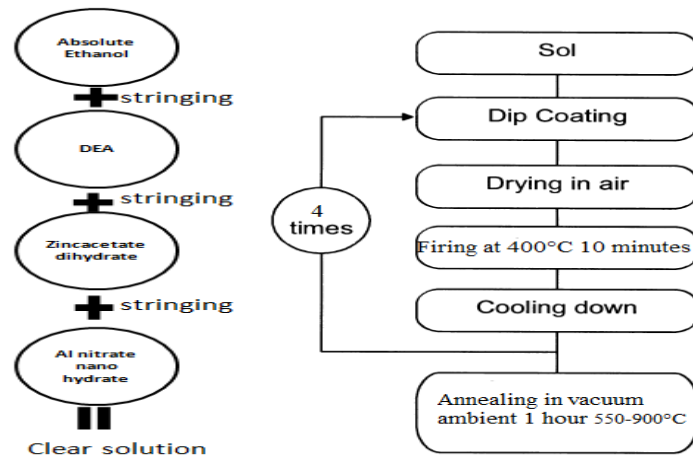


**Figure 6.1:** Flow chart of the preparation of the coating sol and coating procedure for ZnO:Al multilayer coatings.

Before starting the experiments, all laboratory equipments that were used for sol and substrate preparation were cleaned with detergent, than waited for 5 seconds in the sol of sulfuric acid ( $\text{H}_2\text{SO}_4$ ), Potassium dichromate ( $\text{K}_2\text{Cr}_2\text{O}_7$ ) and distilled water. Then all the equipments were rinsed with de-ionized water. At last they were sterilized with water vapour in an auto clave furnace (Nüve OT 012 Bench Top

Steam Sterilizer) as shown Fig.6.2a then dried at 100°C in drying oven (Binder ED 53) as shown Fig. 6.2b.



**Figure 6.2:** a) Nüve OT 012 Bench Top Steam Sterilizer b) Binder ED 53 etuve.

## **6.1. Production Process of ZnO:Al Thin Films and ZnO:Al/p-Si Heterojunctions**

### **6.1.1. Sol Preparation**

The first stage of the dip coating process is sol preparation. A 50 ml aqueous sol was prepared. The sol consists of absolute ethanol as a solvent material, zinc acetate dihydrate  $\text{Zn}((\text{CH}_3\text{COO})_2 \cdot 2\text{H}_2\text{O})$ , 99,5% purity) is added as a starting material and the molar concentration of the zinc is 0.5M. The diethanolamin  $\text{DEA}(\text{CH}_2\text{CH}_2\text{OH})_2$  is added as a stabilizer and a measured amount of Al nitrate nano hydrate  $\text{Al}(\text{NO}_3)_3 \cdot 9\text{H}_2\text{O}$  (extra purity) is added as dopand sources to obtain 0.8-1.0-1.2-1.6 % at. Al ratio ( $R_m = \text{Al}/\text{Zn}$ ).

The molar ratio of DEA to Zincacetat-dihydrat was maintained at 1.0. Then the resulting mixture was stirred with Magnetic stirrer (Heidolph MR 3001K) at 60°C for 1 h to form clear, transparent and homogeneous sol. After cooling, sol was aged at room temperature for 1 day, then the colloidal suspensions were ready to use. The relative humidity was fixed at 43% by dehumidifier to protect the sol quality during the sol preparation and the dip coating processes. The sol was kept in refrigerator to prevent the precipitation and to extend its life.

Differential thermal and thermo gravimetric analyses (DTA/TGA) were performed by using Perkin Elmer Diamond TG-DTA thermal analyses equipment to investigate thermal behaviours of the ZnO:Al thin films, the result analysis is shown in Fig.6.3 [84,85]. Thermal analyses were performed in air with 10°C/min heating and cooling rate from room temperature to 900°C and 900°C to room temperature, respectively.

The analysis in Fig.6.3 was used to settle on heat treatment conditions for annealing of the films.

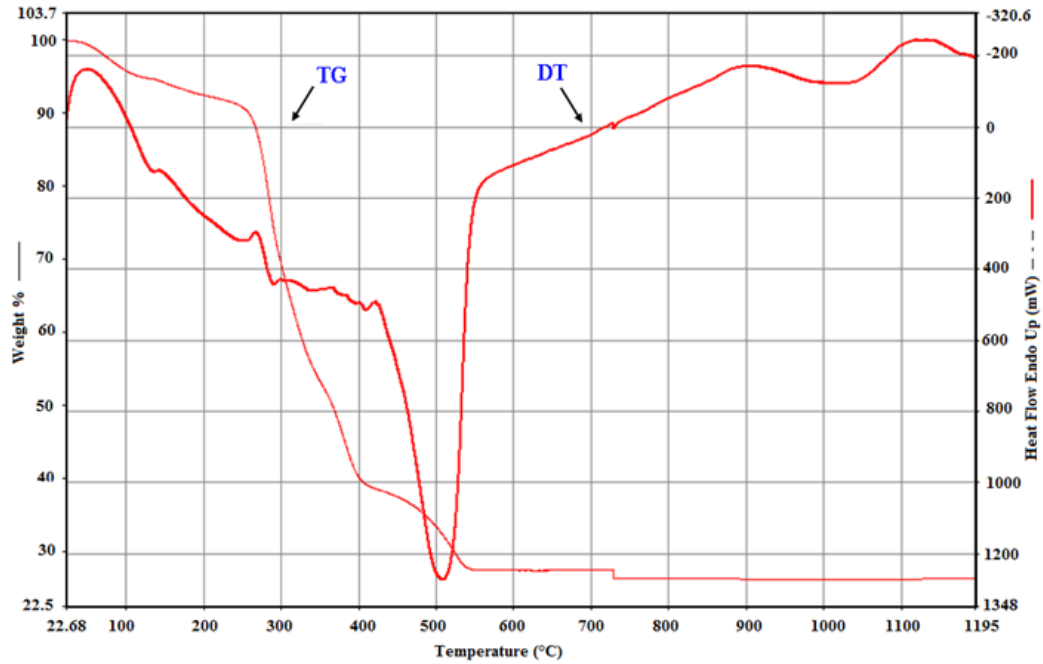


**Figure 6.3:** TG/DT Analyses of dried ZnO:Al gel with 10°C/min heating and cooling rate [76,77].

TG-DT analyses of ZnO:Al indicated an endothermic peak between 290°C and 420°C which shows solvent and organic residuals started to evaporate between these temperatures. A noticeable mass loss (~70 %) was seen at ~520°C which meant the crystallization starts at ~520°C and the increasing lasts till 900°C then started to decrease again. According to these results, the pre-heating temperature which is made to evaporate the organic residuals were defined as 400°C and the annealing temperature which is made for crystallization deposited films were defined as above 520°C till 900°C; 550°C, 600°C, 700°C and 800°C.

### 6.1.2.Pre-treatments of substrates

P-type silicon wafers (100) were used as substrates that are in the dimensions of 10x30 mm, 30x30 mm and 35x35 mm, respectively.

A pretreatment process with three-steps was applied to clean and to dry them before ZnO film deposition. At first, silicon wafers were ultrasonically cleaned in acetone than in alcohol solution for 10 minutes, respectively. Finally, the wafers were dried in air. The ultrasonic cleaning process was performed by using Bondelin Sonorex

Ultrasonic Bath as shown Fig.6.4. After pretreatment, the wafers and the glasses were ready for subsequent sol-gel film deposition.



**Figure 6.4:** Bondelin Sonorex Ultrasonic Bath.

### 6.1.3. Deposition of films

The readily-prepared ZnO:Al sol at different concentrations were deposited on cleaned substrates by sol-gel dip coating technique by a cycle of dipping and drawing the substrates into the sol with 200 mm/min dipping drawing rate and the samples are kept in solution for 5 sec then pre-heated at 400°C for 10 minutes in air. The dipping-drawing cycle with pre-heating was repeated for four times. A computer controlled dip coater (KSV dip coater LMX2) as shown Fig.6.5 was used during film deposition.

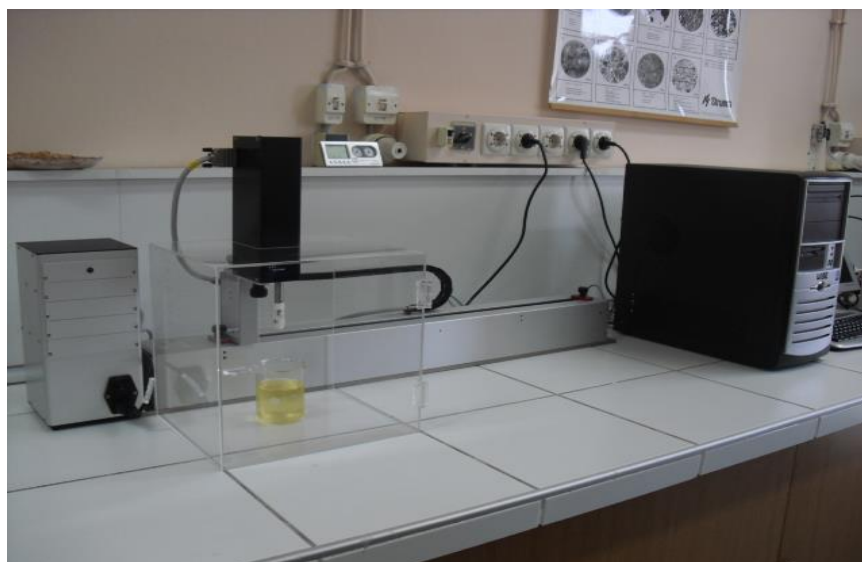


**Figure 6.5:** KSV Dip coater LMX2 equipment.

The four-layered prepared films were post-heated at a range of 550-800°C temperatures for 1 hour in air and vacuum. The pressure was 0,003 mbar in vacuum.

## 6.2.Characterization of ZnO:Al Thin Films

Sol-gel technique has some difficulties and limitations among to other coating techniques. In sol-gel process the properties of the films depend on many different variables such as temperature, humidity and cleanliness of the samples, sol and ambient. The production also has poor reproducibility and reliability. In this study the structural and electrical behaviors of the ZnO:Al films were investigated.

### 6.2.1.Structural properties

X-Ray diffraction patterns and SEM images of the ZnO:Al thin films were investigated to determine the structural properties. The X-Ray diffraction patterns of the thin films were taken at room temperature and the humidity level of the ambient was fixed at 43 % by a dehumidifier. GBC-MMA X-Ray diffractometer as shown Fig. 6.6 with Cu K $\alpha$  radiation of wavelength 1,54 Å was used to record XRD patterns. Diffractometer was operated at 35 kV and 28,5 mA with the energy of 1 kWatt and a 2 deg/min constant scan rate was used to collect 2 $\theta$  data from 20° to 60°.



**Figure 6.6:** GBC-MMA X-Ray diffractometer.

JEOL 6335F Scanning Electron Microscope as shown Fig. 6.7 with 20.0 kV accelerating voltage were used to take SEM images from the surface of the thin films. Hence, it was possible to examine the changes of the surface morphology of the produced thin films at the previous studies.

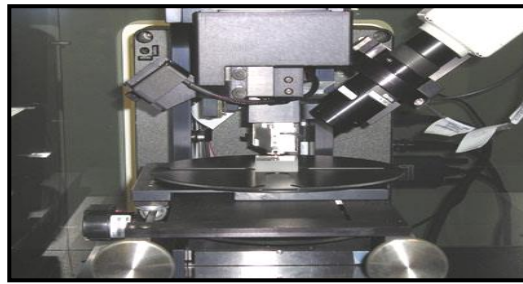


**Figure 6.7:** JEOL 6335F Scanning Electron Microscope.

The thickness measurements were performed by using a surface profilometer Veeco Dektak- 6M surface profilometer as shown Figure 6.8 with 3mg load at different parts of the films. The measurement depends on the thickness difference and the 3mg load moves for 2000 nm between the coated and uncoated parts.



a)



b)

**Figure 6.8:** a) and b) Veeco Dektak- 6M surface profilometer.

### 6.2.2. Electrical properties

The electrical resistivity of ZnO:Al thin films were measured by using a Four Point Resistivity Probe with Mounting Stand (SIGNATONE). The resistivity values calculated with measured thickness values.

### 6.3. Characterization of ZnO:Al/Si Heterojunctions

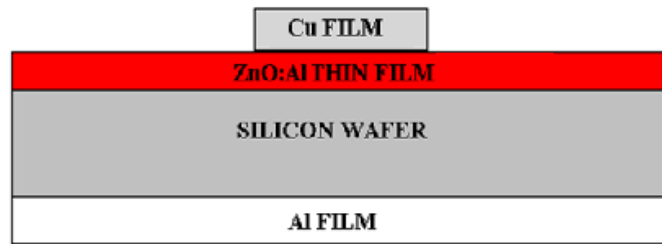
The current-voltage characteristics of the p-n junctions produced by sol-gel dip coating were investigated to examine junction existence. Heterojunctions were fabricated at the configuration of Cu/ZnO:Al/Si/Al. RUSONIC Cold Spray as shown Fig.6.9 was used to obtain Cu and Al ohmic contacts. Hence, it is possible to prepare the samples for current voltage characteristic investigation.





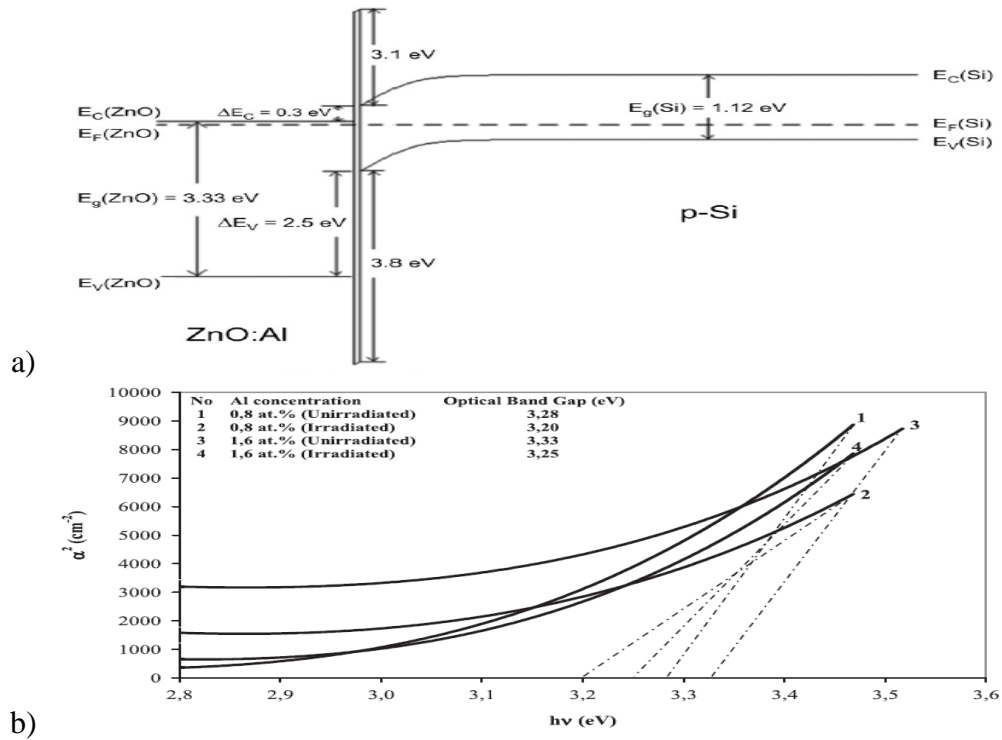
**Figure 6.9:** Rusonic Cold Gas Dynamic Spray equipment.

After the ZnO:Al film deposition, the ohmic back contact of Si wafer was fabricated by cold spray of Al ( $\sim 10 \mu\text{m}$ -average grain size), while the other ohmic contact was fabricated with Cu-grid ( $\sim 22 \mu\text{m}$ -average grain size) through a mask on the front side. During the cold spray, the pressure of air was  $\sim 6$  bar. The areas of Al and Cu electrodes were  $0.7\text{cm}^2$ . Fig.6.10 presents the schematic diagram of ZnO:Al/Si heterojunction.



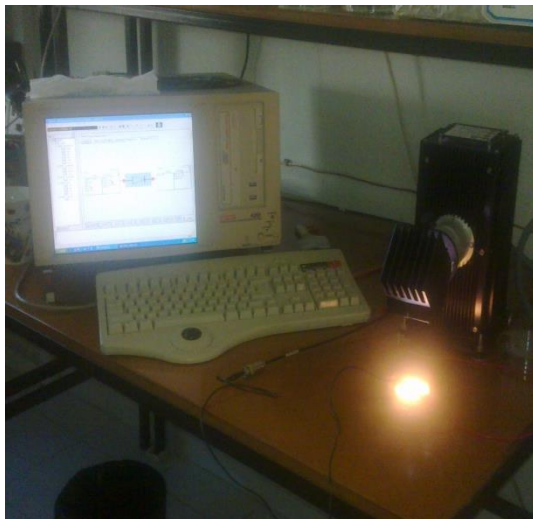
**Figure 6.10:** Schematic diagram of ZnO:Al/Si heterojunction.

Fig.6.11a shows the band gap structure of the ZnO:Al/p-Si heterojunction device in the literature [72]. The similar results for the bandgap structure of the produced ZnO:Al /p-Si heterojunction at 1.2 at% Al concentration can be obtained as  $\sim 1.33$  eV in this study because the ZnO:Al /p-Si heterojunction is produced at the same production condition in the previous study as shown Fig.6.11b [90] .



**Figure 6.11:** a) Bandgap structure of the novel ZnO:Al /p-Si heterojunction b) Optical band gaps of ZnO:Al thin films at 0.8 and 1.6 at % Al concentrations for unirradiated and their radiated states [90].

The current voltage characteristic analyses was made with Direct Current (DC) voltage in the range between -20 and +20 at room temperature, under dark and light (Xenon lamp 100mW/cm<sup>2</sup>) conditions by Keithley 4200 Semiconductor Characterization System (SCS) are shown in Fig.6.12b.



a)



b)

**Figure 6.12:** a) Keithley 4200 Semiconductor characterization system (SCS) b) LOT-Oriel 100/150 W Hg/Hg (Xe) Light Source.

C-V measurement was performed by Hewlett Packard 4192A Impedance Analyzer as shown Fig.6.13, where the input voltage frequency was fixed at 1 MHz with a sweeping rate of 0.2 V/s at room temperature. In C-V and I-V measurements, the devices were kept in a light-proof box shielded very carefully against light to avoid the effect from background light.



**Figure 6.13:** Hewlett Packard 4192A Impedance Analyzer.



## 7.RESULTS AND DISCUSSION

ZnO:Al thin film samples were produced by sol-gel dip coating technique on to p type silicon wafer substrates at different concentrations. Thin film structure has been characterized by X-ray diffraction, Scanning Electron Microscopy (SEM). All the films are polycrystalline with wurtzite structure. The thicknesses of the thin film samples were determined by using surface profilometer and measured in the range of 150-500 nm. The four-point probe technique was used to evaluate the electrical resistivity of thin films. The heterojunction properties of ZnO:Al/p-Si structures were investigated by I-V measurements evaluated with Keithley 4200 Semiconductor Characterization System and C-V measurements with Hewlett Packard 4192A Impedance Analyzer System.

### 7.1. Structural Properties of ZnO:Al Thin Films

Structural properties were analyzed by X-ray diffraction patterns and SEM images of the ZnO:Al thin films. According to X-ray diffraction patterns the average crystallite sizes were calculated by application of Scherrer-Warren formula (7.1) in;

$$D = [(0.9\lambda)/(\beta\cos\theta_{\beta})] \quad (7.1)$$

where  $\lambda$  is the wavelength X-ray of 1.54 Å,  $\theta_{\beta}$  is Bragg diffraction angle,  $\beta$  is the FWHM (Full Width Half Maximum of Distinctive Peak) of  $\theta_{\beta}$ .

#### 7.1.1. Effects of Al concentration

In order to study the effect of aluminium concentration on the microstructural properties of Al-doped ZnO thin films, samples with different value of dopant concentration (0.8 mol. %, 1.0 mol.%, 1.2 mol.% and 1.6 mol.%) were used. The XRD spectra of four films at different doping concentration annealed at 700°C in vacuum are shown in Fig.7.1a. It indicated that the film is a crystalline with a preferential orientation along c-axis and exhibited the wurtzite structure with all XRD peaks identified in the 20-60  $2\theta$  range. According to these patterns, the films

with all Al dop concentration were polycrystalline and showed three orientation peak as (100), (002) and (101).

The c-axis orientation in ZnO:Al films is due to a self-texturing mechanism. We concluded that the film crystal orientation is not affected by the crystallographic structure of a substrate, but is a result of a self-ordering effect caused by the minimization of the crystal surface free energy as well as by the interaction between the deposited material and the substrate surface.

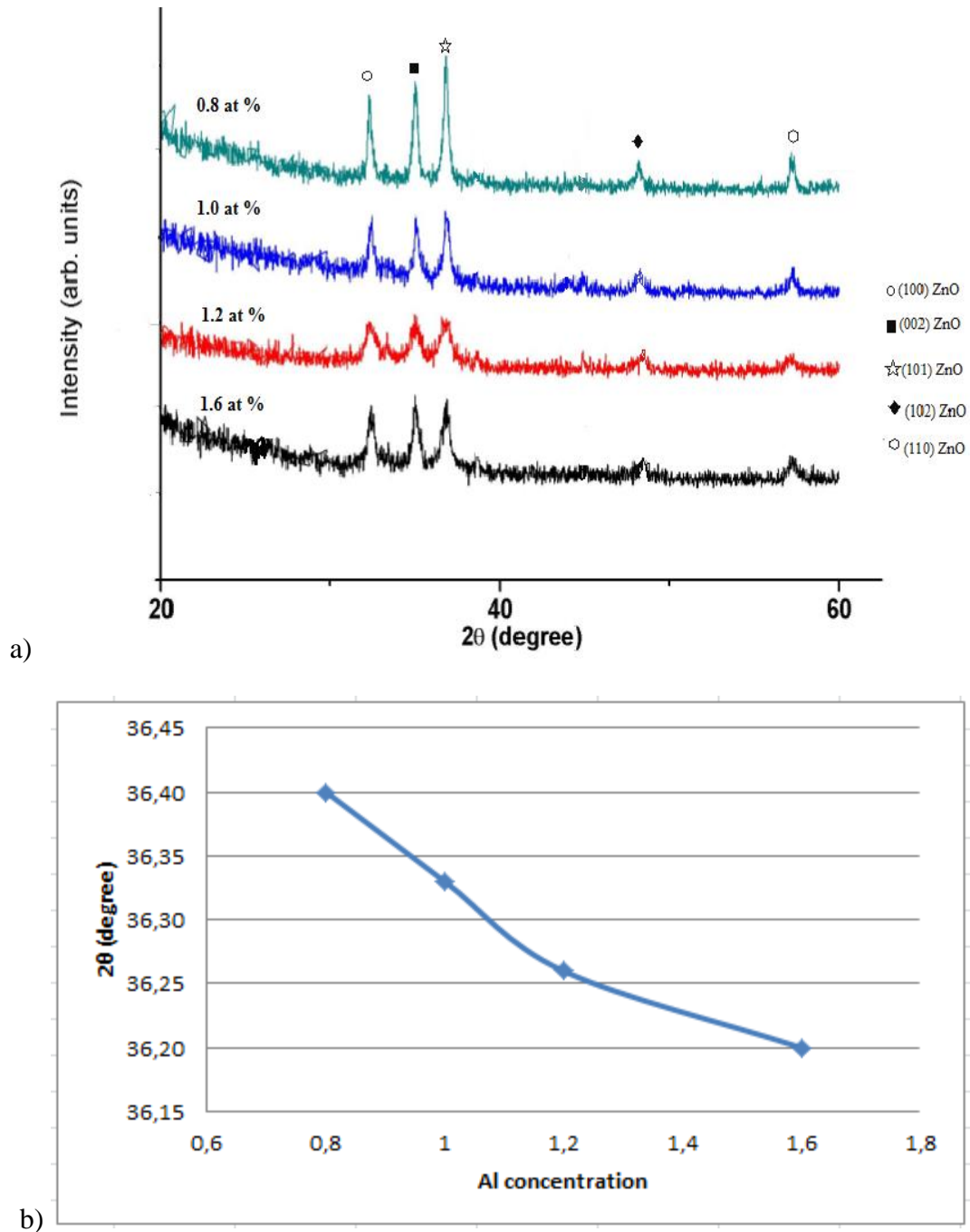


**Figure 7.1:** a) X-Ray diffraction patterns of ZnO:Al thin films depends on Al concentration annealed at 700°C in vacuum b) 2θ value of the samples at different doping concentrations.

The 1.6 mol % aluminum-doped ZnO thin film had the highest (101) diffraction peak intensity. Moreover, the peak intensities of those films decreased with increased doping concentrations as shown Fig.7.1a. This indicates that an increase in doping concentration deteriorates the crystallinity of films, which may be due to the formation of stresses by the difference in ion size between zinc and the dopant and the segregation of dopants in grain boundaries for high doping concentrations. On the other hand, the peak position of the (101) plane is shifted to the low  $2\theta$  value with the increase of Al doping concentration as shown Fig.7.1b. The shift of the diffraction peak position from the undoped ZnO thin film indicates that films were in a uniform state of stress with tensile components parallel to c-axis. Similar shifts that are in agreement with those have also observed by Mass et al [86].

According to calculation of the crystallite sizes from the XRD patterns, it is suggested that the ZnO films are nanocrystalline and the average crystallite sizes are in the range of 18-45 nm. The calculated average crystallite sizes at (100), (002) and (101) orientation showed in Appendix 1.

There is an increasing on the average crystallite size by decreasing of the dopant concentration due to film crystalline distortion. The decrease in the calculated average crystallite size depending on Al concentration is shown in Fig.7.2. The reason of increasing on the average crystallite size could be the difference between ionic radius of the Zn and the dopant element Al ( $r_{\text{Zn}}^{+2}=0,074 \text{ nm}$ - $r_{\text{Al}}^{+3}=0,054\text{nm}$ ). The difference between ionic radiuses of Zn and Al might cause a drag on grain growth by compression stress [87].

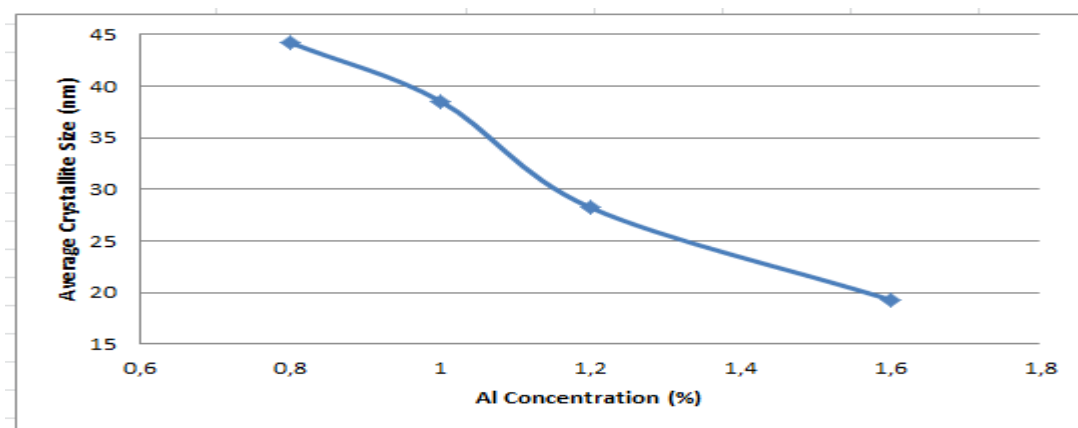


**Figure 7.2:** Average crystallite sizes of ZnO:Al thin films oriented in (101) depends on Al concentration annealed at 700°C in vacuum.

### 7.1.2. Effects of annealing temperature

The X-ray diffraction patterns of the films 1.2 at. % Al doped and annealed at four different temperature values between 550-800°C in air are shown in Fig.7.3.

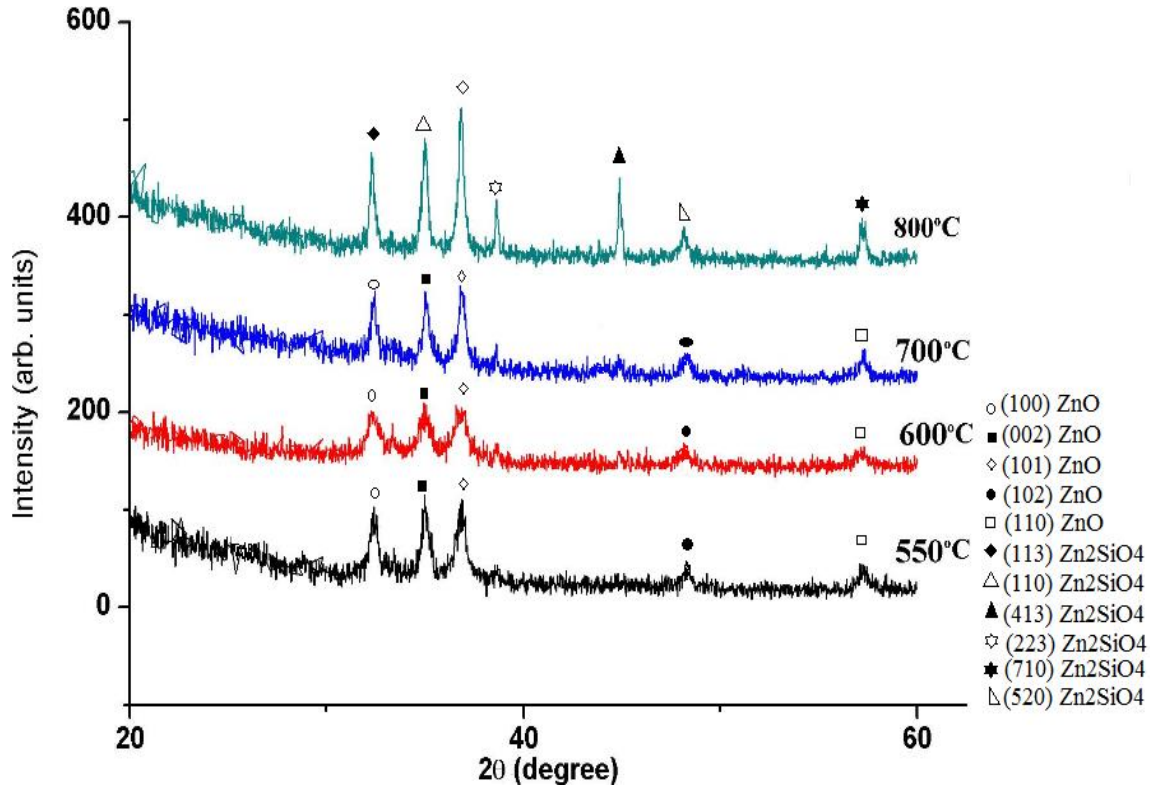


**Figure 7.3:** X-ray diffraction patterns of 1.2 at. % Al doped ZnO:Al thin films annealed in air depends on annealing temperature.

Since the surface properties of the ZnO:Al thin films can affect electrical and optical properties and characteristics of the optical devices, it is very important to investigate the surface morphology of ZnO:Al thin films. Fig.7.5 shows SEM surface micrographs of ZnO:Al films prepared in the air at various deposition temperatures. As the deposition temperature increased, the grain size increased as shown Fig.7.4 and the surface roughness decreased. These results, in agreement with the XRD analysis, indicated that the diffusion probability of ZnO and Al atoms on the surface can be controlled by the deposition temperature. A higher temperature enhances the occupation probability of Al ions on Zn sites, as well as oxygen vacancies and Zn interstitial atoms. In other words, Al atoms can diffuse to the surface, dependent upon the deposition temperature. An increase in crystalline size would be strongly related to a decrease in resistance for free electrons, because of lower grain and grain-boundary scattering.



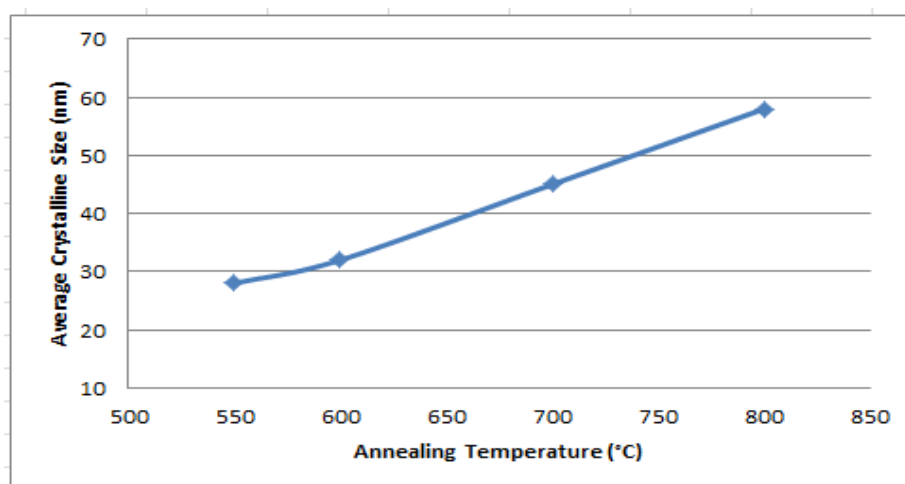


**Figure 7.4:** Average Crystallite Size of 1.2 at. % Al doped ZnO:Al thin films oriented in (101) annealed in air as a function of annealing temperature.

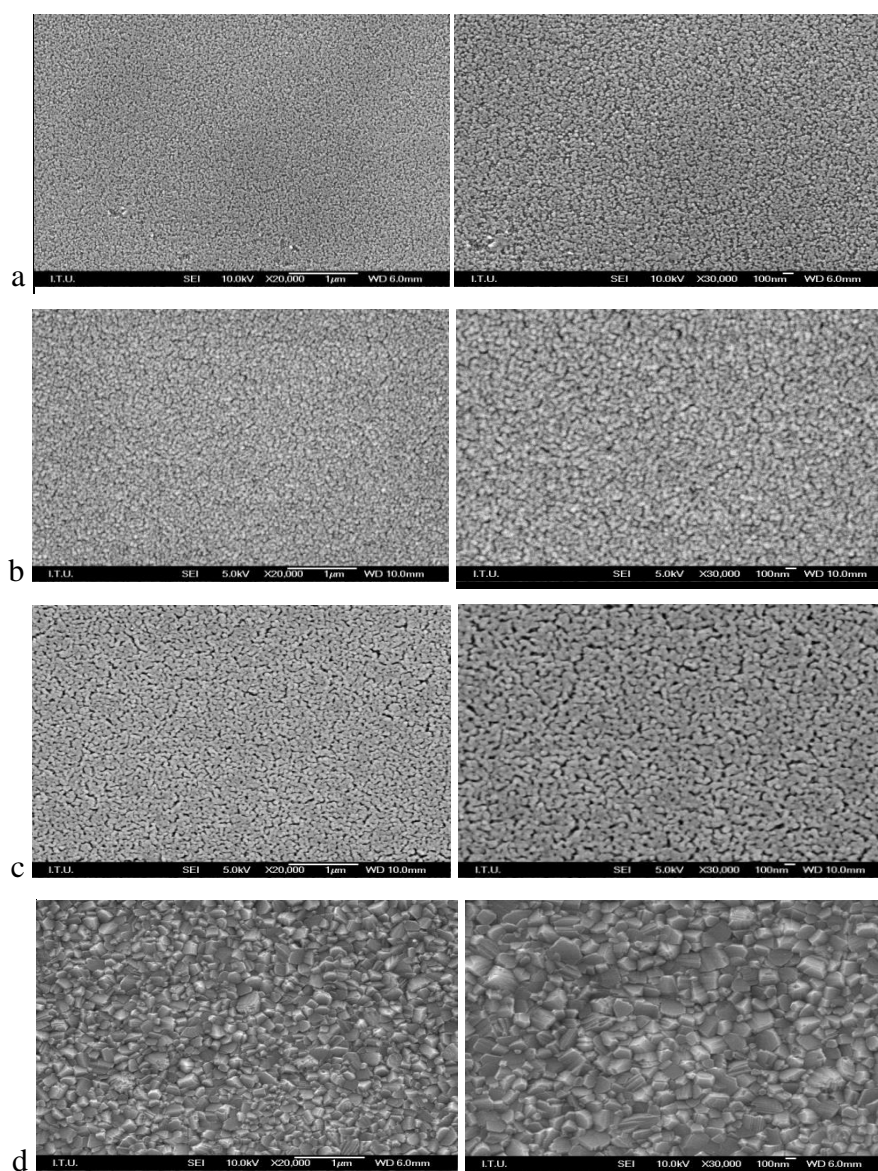


**Figure 7.5:** SEM images of 1.2 at. % Al doped ZnO:Al thin films annealed in air at a) 550°C b) 600°C c) 700°C d) 800°C (20.000X and 30.000X) [88].

The identified diffraction peaks correspond to (100), (002), (101), (102) and (110) plane reflections for Wurtzite-type ZnO. Among these diffraction peaks, the (101) is the most intensive. The intensity of ZnO (101) diffraction peak increased as the annealing temperatures were increased from 550 to 700 °C. The spectrum reveals that ZnO thin film exists a preferred (101) orientation after annealing at high temperature. The mechanism of the c-axis oriented ZnO films can be attributed that the value of surface free energy of ZnO (101) plane is minimum at the growth stage. The intensity of the diffraction peaks of the films are higher with the rise of the annealing temperature of the thin film at the (101) diffraction plane as showed in Appendix A.2.

The grain sizes of ZnO:Al nanocrystallites were in average value range from ~ 20 nm to 58 nm in diameter when the annealing temperature increased from 550 to 800 °C in air in Appendix A.2.

Fig.7.5 shows, the surface of the film become smooth after annealing in air at 600 °C for 1 h and the well-regulated grain boundary with hexagonal structure. However, the film has the trapezium crystals after annealing at 800 °C for 1 h. Although the surface morphology of sample (at 800 °C) indicates the best crystal quality among the four samples, however, the transform of the surface morphology (from the hexagonal to the trapezium) probably predicts a generation of a new compound [88], because a typical ZnO is a hexagonal structure and is impossible to appear as a trapezium like surface. Therefore, we guess that a new zincic compound may be formed in the annealed films. The compound is most probably a zinc silicate, e.g.  $\text{Zn}_2\text{SiO}_4$  can be formed at 770 °C.  $\text{Zn}_2\text{SiO}_4$  has a tetragonal structure or a trigonal structure. Therefore, the hexagonal ZnO and the tetragonal (or trigonal) zinc silicate may coexist in the film; this is the reason of a trapezium shape. Such trapezium is probably a mixture crystal of the hexagonal ZnO and the zinc silicate. The ratio of ZnO to zinc silicate in the film could be decreased by increasing the annealing temperature, since the crystal shape of sample (at 800 °C) is a typical trapezium.

Effects of different annealing temperature, ambient and dopant concentration on the film thickness were investigated. 1.2 at. % Al doped films annealed at the temperature range of 600°C-800°C in vacuum and air as shown Fig.7.6. According to the graph, a decrease in the thickness is obviously seen by the increase of

annealing temperature. The thicknesses of the films annealed in air and vacuum are in the range of 150-440 nm.

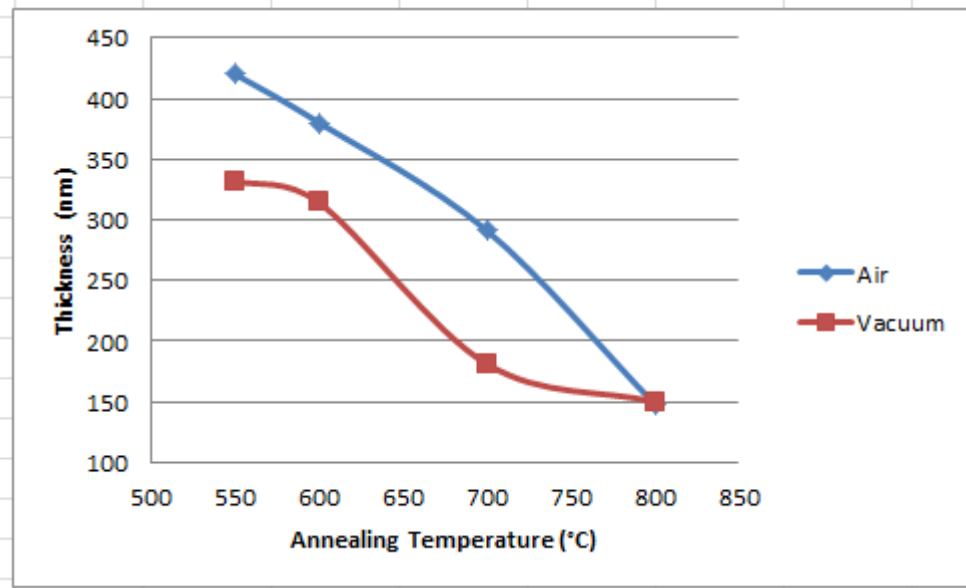


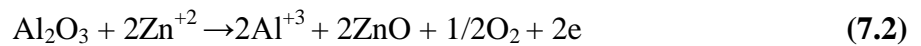
**Figure 7.6:** Variation of ZnO:Al thin film thickness as a function of annealing temperature for 1.2 at.% Al.

The XRD analysis as shown Fig.7.3, SEM examinations as shown Fig.7.5 and thickness measurements as shown Fig.7.6 indicate that higher annealing temperatures induce thinner and denser ZnO:Al films because of the elimination of structural discontinuities, such as grain boundaries and pores.

## 7.2. Electrical Properties of ZnO:Al Thin Films

### 7.2.1. Effects of Al concentration

The resistivity variation of Al-doped ZnO films with different doping concentrations is showed in Fig.7.7. The resistivity first decreased with increased Al concentrations. A minimum resistivity of  $1.32 \times 10^{-4} \Omega \text{ cm}$  was obtained at a doping concentration of 1.2 mol.%. The increase of the quantity of Al led to a subsequent increase of the carrier concentration. The carrier concentrations of these films are supplied from donor sites associated with the excess metal ions. An effective substitution of the dopant (Al) atoms in Zn sites of the ZnO structure took place according to the following equation (7.2):



However, the resistivity was started increasing significantly with increase in the Al doping concentration above 1.2 mol.%. When a small amount of Al is introduced

into the film, the Al is ionized into  $\text{Al}^{+3}$  and replaces  $\text{Zn}^{+2}$ . Thus one free electron is produced from one zinc atom replacement. The carrier concentration increases with Al concentration at first up to 1.2 mol. % doping. The carrier concentration decreases at higher Al concentrations, because increasing dopant atom forms some kind of neutral defects and these neutralized Al atoms do not contribute free electrons. The amount of electrically active Al in the film decreases when doping is high, i.e. more Al atoms are neutralized at higher Al concentration. Similar explanations have also reported for Al-doped ZnO films sol-gel method in the previous studies by Z.Q.Xu et al [17].

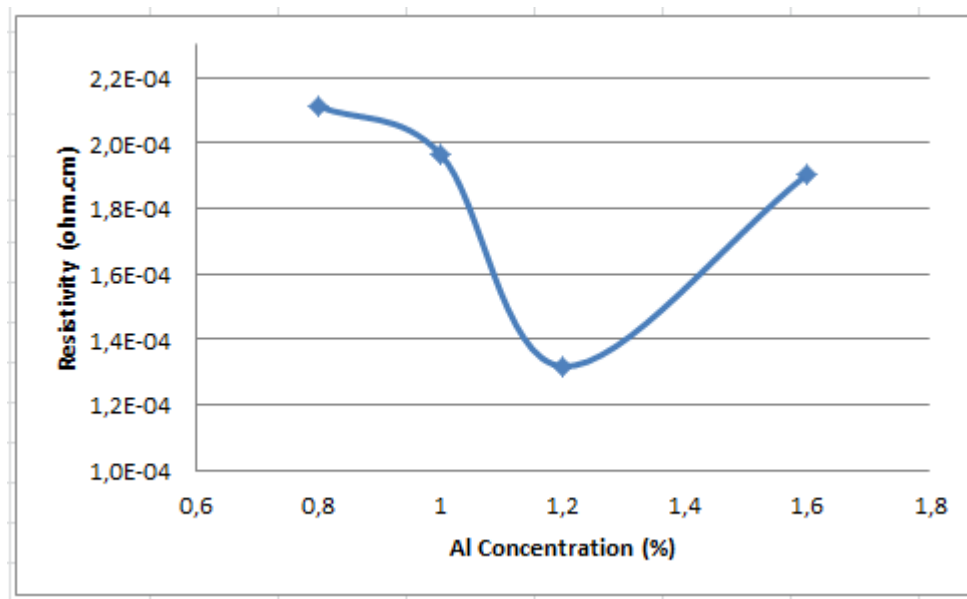


**Figure 7.7:** Variation of resistivity as a function of dopant concentration for Al doped ZnO thin films annealed at 700°C under vacuum.

### 7.2.2. Effects of annealing temperature

The electrical resistivity values of the films with different doping concentrations were plotted as shown Fig.7.8 after the films were annealed at four different annealing temperatures in vacuum. The resistivity has decreased from 0.8 to 1.2 at. % Al concentration. The lowest resistivity is  $\sim 0.1 \times 10^{-4} \Omega \cdot \text{cm}$  at 800 °C in vacuum.

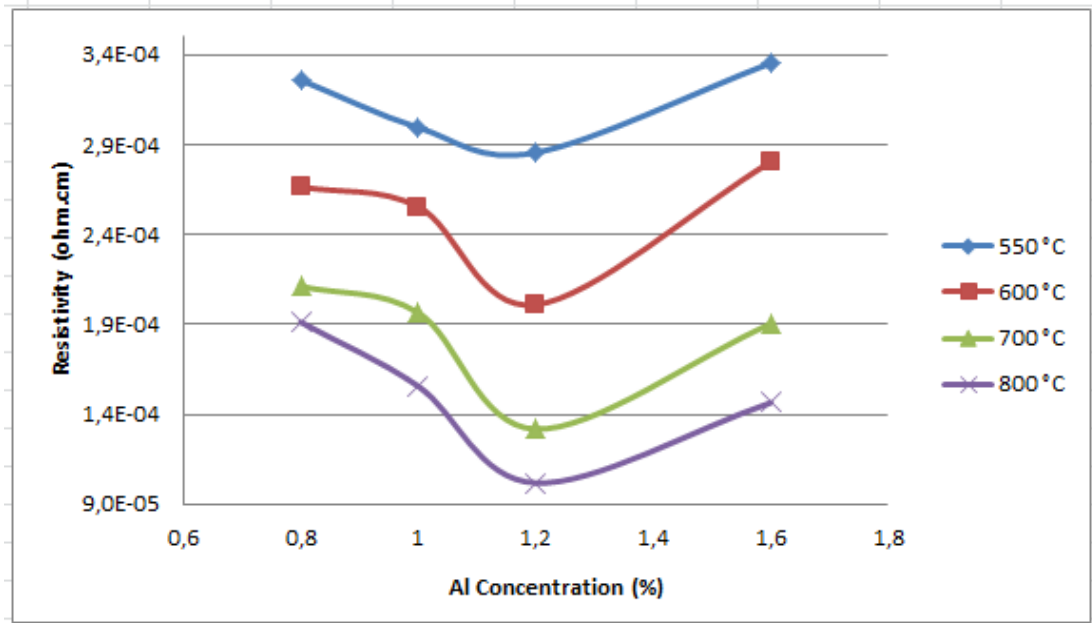


**Figure 7.8:** Variation of resistivity as a function of dopant concentration for Al doped ZnO thin films annealed at different temperatures under vacuum.

The resistivity behaviors of the thin films according to annealing temperature were investigated at the dopant concentration of 1.2 at. % after the thin film was annealed in vacuum and air as shown Fig.7.9 and Fig.7.10. Resistivity of the film decreased from  $\sim 2.9 \times 10^{-4}$  to  $\sim 1.9 \times 10^{-4} \Omega \cdot \text{cm}$  in vacuum. However, there was a decrease on resistivity from  $\sim 14 \times 10^{-2}$  to  $\sim 7 \times 10^{-2} \Omega \cdot \text{cm}$  in air, this decrease was faster with respect to resistivity decrease in vacuum. In general, as the annealing temperature increases, the resistivity of Al doped ZnO film decreases because the crystallinity is enhanced. In addition, the major carrier of Al doped ZnO thin films is the excess metal ions, while in the case of pure ZnO the electrons due to oxygen vacancies or zinc interstitials are not very effective because of oxygen adsorption. When the annealing treatment is performed, the carrier's concentration may increase by desorption of oxygen in the grain boundaries, which act as traps for the carriers. It could partly contribute to the decrease in resistivity.

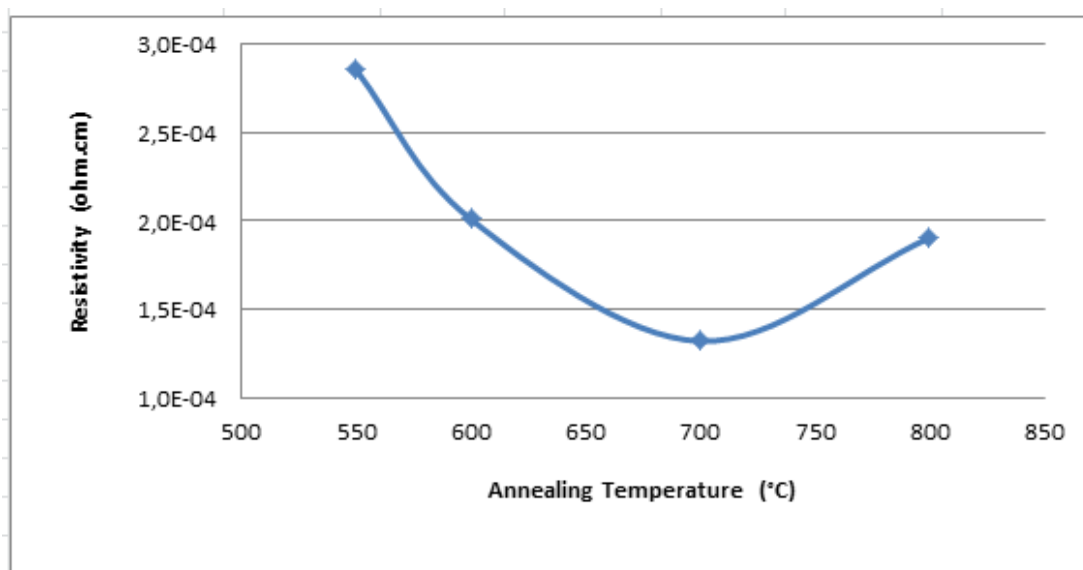


**Figure 7.9:** Variation of resistivity as a function of annealing temperature for 1.2 at. % Al doped ZnO thin films annealed under vacuum.

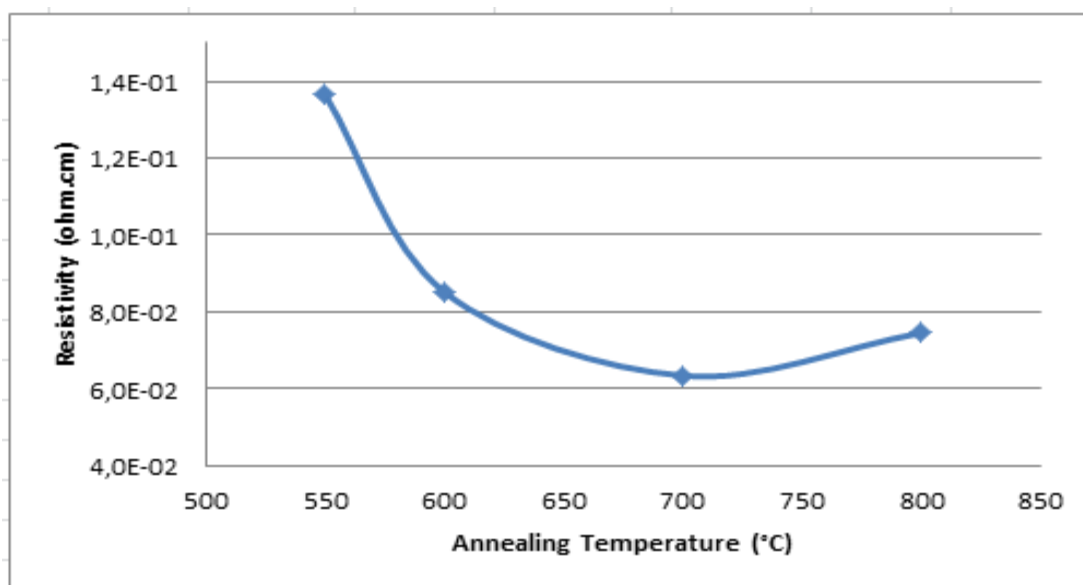
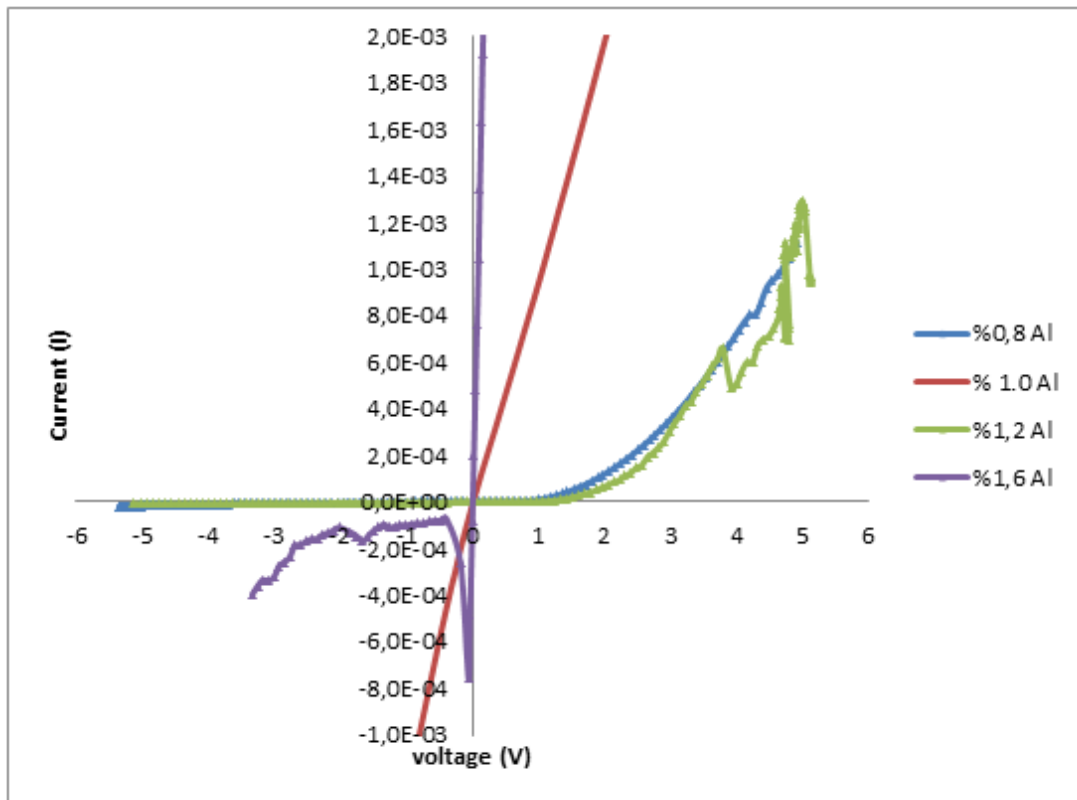


**Figure 7.10:** The changes on the resistivity of 1.2 at. % Al doped ZnO thin films annealed in air as a function of annealing temperature.

### 7.3.Heterojunction Properties of ZnO:Al/ p-Si

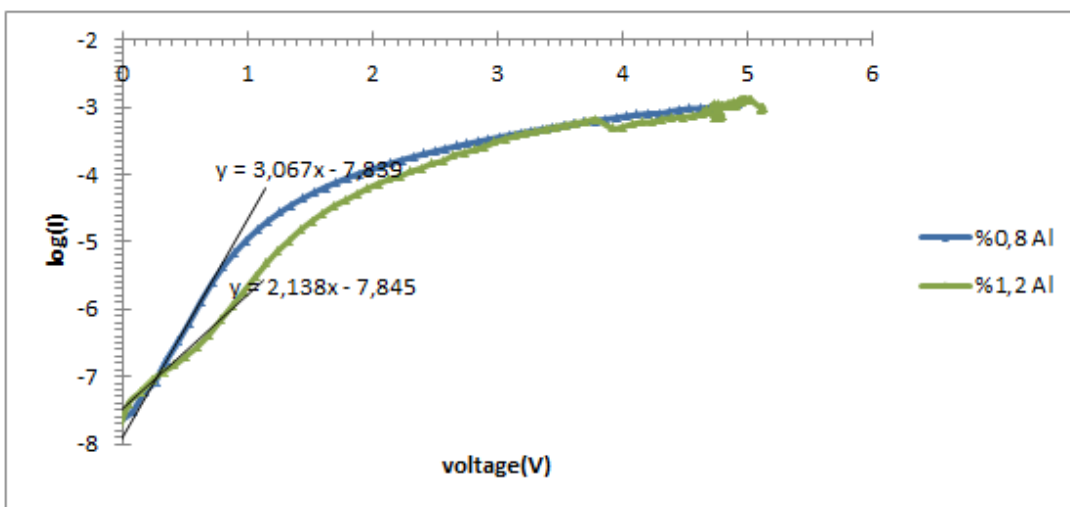
#### 7.3.1.Effects of Al concentration

Fig.7.11 showed the current-voltage characteristic of the ZnO:Al/p-Si heterojunctions measured at room temperature under dark. The ZnO:Al heterojunctions annealed at 700°C in vacuum had different Al concentrations ranging from 0.8 to 1.6 at. %. In forward bias the current through the heterojunctions change with the applied voltage where in reverse bias the current through the heterojunctions does not change substantially with voltage change. These I-V characteristics of the ZnO:Al/p-Si heterojunctions prepared by sol- gel dip coating technique are similar with I-V characteristic of typical diode. The similarity of I-V characteristics indicates the formation of a diode between sol-gel prepared ZnO:Al thin films and p-Si. I-V curve of ZnO:Al/p-Si heterjunction with 1.0 and 1.6 at.% Al concentration lead to the deviation of a diode characteristics from those of the ideal diode. These two I-V curves are symmetrical, non-rectifying, and linear in the small voltage range, implying that the Cu/p-Si junction has ohmic-contact characteristics. When ohmic contact was fabricated with Cu-grid (~22  $\mu\text{m}$ -average grain size) through a mask on the front side by cold spray, ZnO:Al film on the p-Si wafer should be removed from surface due to high pressure of process air. The diodes show rectifying behavior with rectification ratio,  $I_F/I_R$ , ( $I_F$  and  $I_R$  are forward and reverse current respectively) values at a  $\pm 20$  V bias voltage as shown in Table 7.1. The most conductive and rectifier heterojunction is determined as ZnO:Al/p-Si with 1.2 at.% Al concentration



**Figure 7.11:** Current-voltage characteristics of ZnO:Al/p-Si heterojunctions under dark condition for different Al concentrations annealed at 700°C under vacuum.

Fig.7.12 shows dependence of the forward current in logarithmic scale with the change of the Al concentration. The value of the ideality factor of the ZnO:Al/p-Si heterojunction is determined from the slope of the straight line region of the forward bias log I-V characteristics.



**Figure 7.12:** Semilog I-V characteristics of ZnO:Al/p-Si heterojunctions under dark condition for 0.8 % at. and 1.2 % at. Al concentrations annealed at 700°C under vacuum.



When the semi-logarithmic forward-biased curves as shown Fig.7.12 are fitted to the standard diode equation given in Equation (5.1), the ideality factors of the diodes fabricated in vacuum at 700°C are shown in Table 7.1. It is determined that heterojunction with 1.2 at. % Al concentration declare lower ideality factors ( $n$ ) than that of with 0.8 at. % Al concentration. There is a consistency between the changes on the ZnO:Al thin film resistivity (ohm.cm) and ideality factor of heterojunctions according to Al concentration. There is an increase in  $I_0$  as well as an increase in ideality factor in Table 7.1.

**Table 7.1:**  $I_0$ ,  $n$  and  $I_F/I_R$  values of ZnO:Al/p-Si heterojunctions for 0.8 % at. and 1.2 % at. Al concentrations.

Al Concentration (at. %)	$I_0$ (A)	$n$	$I_F/I_R$
0.8	$1.448 \times 10^{-8}$	3.067	31
1.2	$1.428 \times 10^{-8}$	2.138	71.2

The representative in dark and light I-V characteristics for the ZnO:Al/p-Si heterojunction is shown Fig.7.13. Typical good rectifying and photoelectric behavior were observed for the device. The dark leakage current is small, whereas its photocurrent generated under illumination is much higher. It is observed that the heterojunction exhibits a rectifying behavior in the presence of light too. Though no significant change in the current under forward bias conditions takes place after illumination, the current under reverse bias conditions is affected by illumination. Under reverse bias conditions photocurrent caused by the ZnO:Al surfaces exposing under illumination by Xenon lamp ( $100\text{mW}/\text{cm}^2$ ) was obviously much larger than the dark current. For example, when the reverse bias is  $-3\text{ V}$ , the dark currents are only  $5 \times 10^{-6}\text{ A}$  (for 0.8 % at Al concentration) and  $1 \times 10^{-5}\text{ A}$  (for 1.2 % at Al concentration). While the reverse-bias photocurrent reach to  $1.255 \times 10^{-5}\text{ A}$  (for 0.8 % at Al concentration) and  $9.24 \times 10^{-5}\text{ A}$  ( for 1.2 % at Al concentration) under Xenon lamp ( $100\text{mW}/\text{cm}^2$ ) as shown Table 7.2. This is generally understood that the photoelectric effect results from the light-induced electron generation at the depletion area of the p-Si, particularly near the heterojunction interface. Light is absorbed in the p-Si layer and generated electrons and holes are drifted to ZnO:Al side and Si side. So the photocurrents are consequently obtained. Consequently, the current increases linearly as the reverse bias increases as shown Fig.7.13.

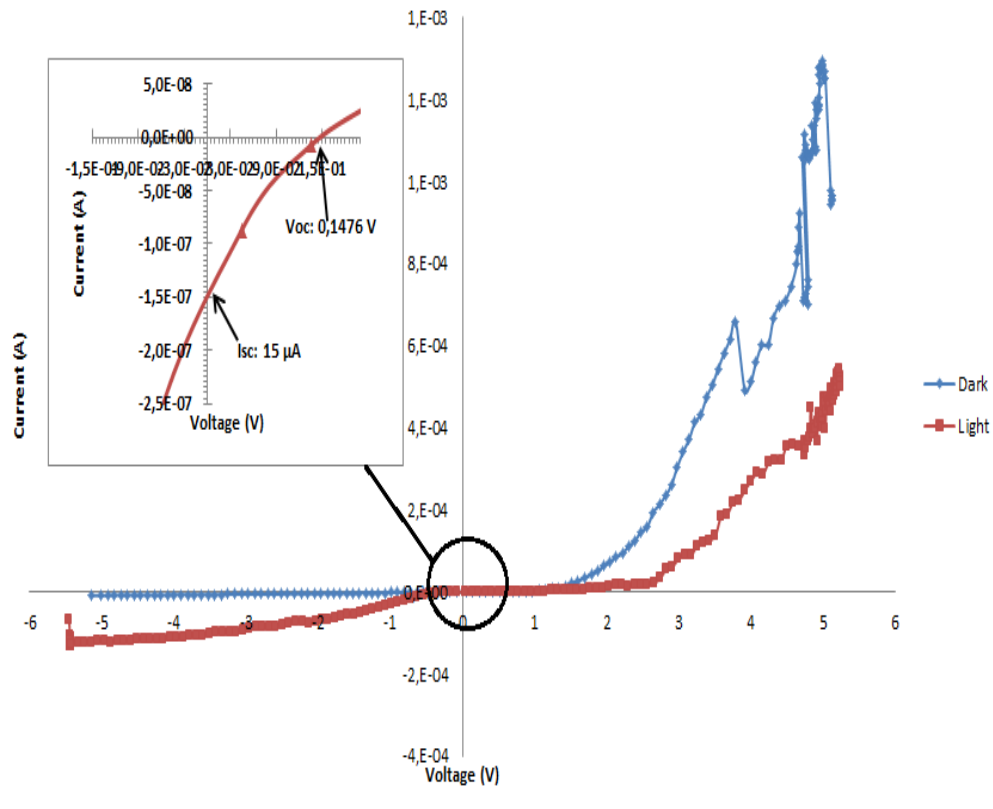
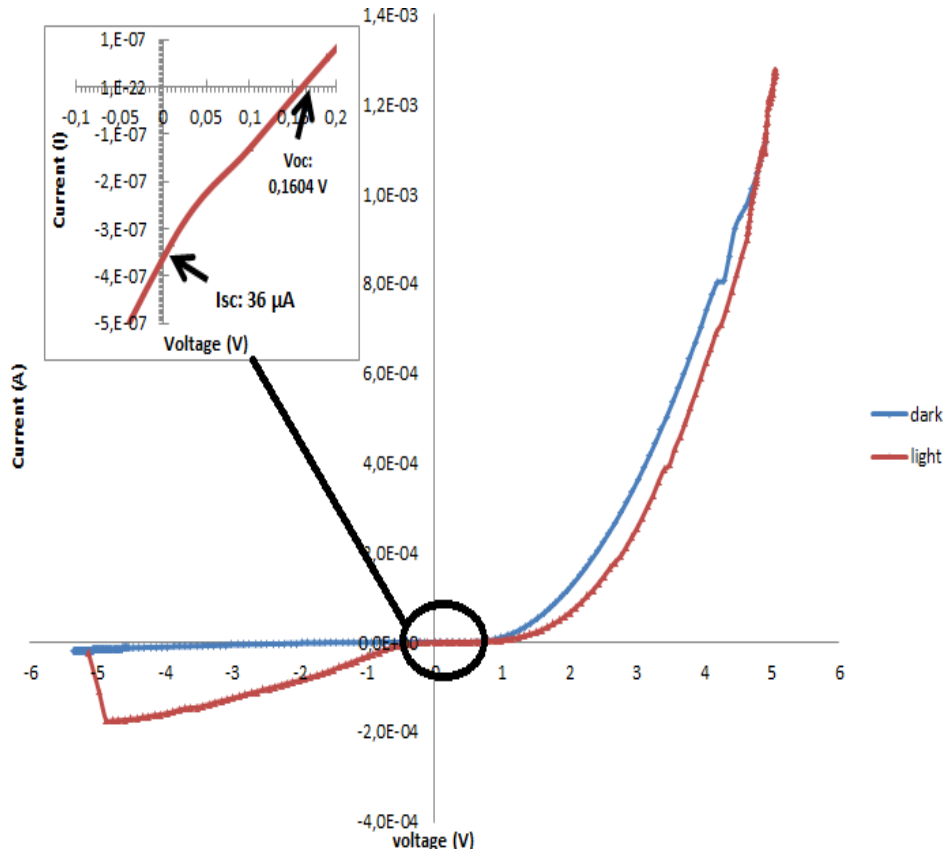


**Figure 7.13:** I-V characteristic of ZnO:Al/p-Si heterojunction annealed under vacuum at 700°C in dark and in light for a) 0.8 % at. and b) 1.2 % at. Al concentrations.

In Table 7.2 the values of the current flow through the ZnO:Al/p-Si heterojunctions under dark and UV illumination in reverse bias are shown. The current flows have risen in each Al concentration with the UV illumination. High photocurrent is obtained under reverse bias due to the crystalline quality of ZnO:Al thin films (obtained in XRD results) is good enough to transmit light into p-Si.

**Table 7.2:** Measured current at -3V under dark and light for heterojunctions for 0.8 % at. and 1.2 % at. Al concentrations

Al Concentration (at. %)	$I_{\text{dark}}$	$I_{\text{light}}$
0.8	$-5 \times 10^{-6}$	$-1.255 \times 10^{-4}$
1.2	$-1 \times 10^{-5}$	$-9.24 \times 10^{-5}$

The "fill factor", more commonly known by its abbreviation "FF" and it is a parameter which, in conjunction with  $V_{\text{oc}}$  and  $I_{\text{sc}}$ , determines the maximum power from a solar cell. The FF is defined as the ratio of the maximum power from the solar cell to the product of  $V_{\text{oc}}$  and  $I_{\text{sc}}$ . The FF is most commonly determined from measurement of the I-V curve as shown in insert of Figure 7.13a and b and is defined as the maximum power divided by equation (7.3) the product of  $I_{\text{sc}}$ ,  $V_{\text{oc}}$ , i.e. [68]:

$$FF = (V_{\text{MP}} \times I_{\text{MP}}) / (V_{\text{OC}} \times I_{\text{SC}}) \quad (7.3)$$

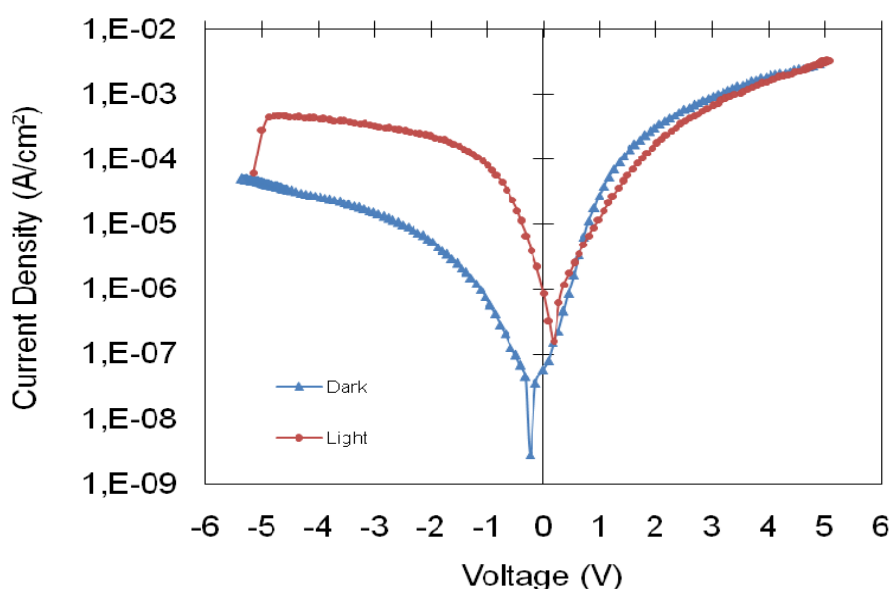
Where  $V_{\text{oc}}$  is the open-circuit voltage ( $V_{\text{oc}}$ , is the maximum voltage available from a solar cell, and this occurs at zero current),  $I_{\text{sc}}$  is the short-circuit current ( $I_{\text{sc}}$  is the current through the solar cell when the voltage across the solar cell is zero),  $V_{\text{mp}}$  is the peak voltage and  $I_{\text{mp}}$  is peak current. The values of  $V_{\text{oc}}$ ,  $I_{\text{sc}}$ ,  $V_{\text{mp}}$  and  $I_{\text{mp}}$  are shown in Table 7.3. A high n-value not only degrades the FF, but since it will also usually signal high recombination, it gives low open-circuit voltages [68].

**Table 7.3:** Measured  $V_{\text{OC}}$ ,  $I_{\text{SC}}$ ,  $V_{\text{MP}}$ ,  $I_{\text{MP}}$  and FF values for heterojunctions under light for 0.8 % at. and 1.2 % at. Al concentrations.

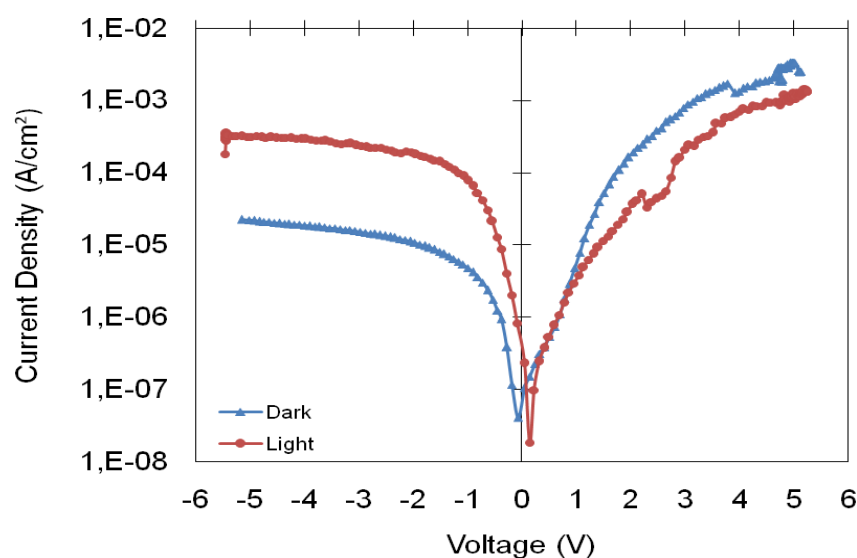
Al Concentration (at. %)	$V_{\text{OC}}$ (V)	$I_{\text{SC}}$ ( $\mu\text{A}$ )	$V_{\text{MP}}$ (V)	$I_{\text{MP}}$ ( $\mu\text{A}$ )	FF
0.8	0.1604	-36	0.0500	-22	% 19.43
1.2	0.1476	-15	0.0538	-760	% 18.40

Fig.7.14 shows the current density-voltage characteristics of ZnO:Al/p-Si heterojunction were measured at room temperature under dark condition and under illumination by UV light source (Xenon lamp  $100\text{mW}/\text{cm}^2$ ). The heterojunctions with different Al concentrations were annealed at  $700^\circ\text{C}$  in vacuum. The results show that the current-voltage characteristics of ZnO:Al/p-Si heterojunction measured

in the dark demonstrating fairly good rectifying behavior and indicating formation of a diode between ZnO:Al and p-Si. The curves in forward bias plotted according to measurements under the dark and light conditions are higher than the curves plotted in reverse bias which indicates that the junctions exhibit diode-like rectifying behavior at 0.8 % at and 1.2 % at Al concentrations. The junction fabricated at 1.2 % at Al concentration shows highest current conduction under dark and light.



a)

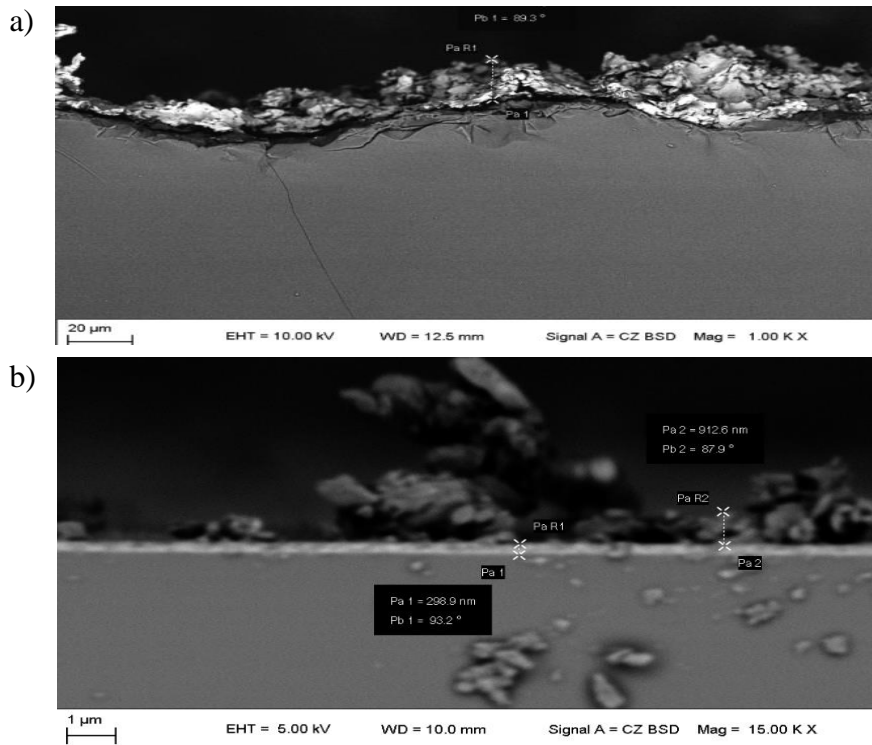


b)

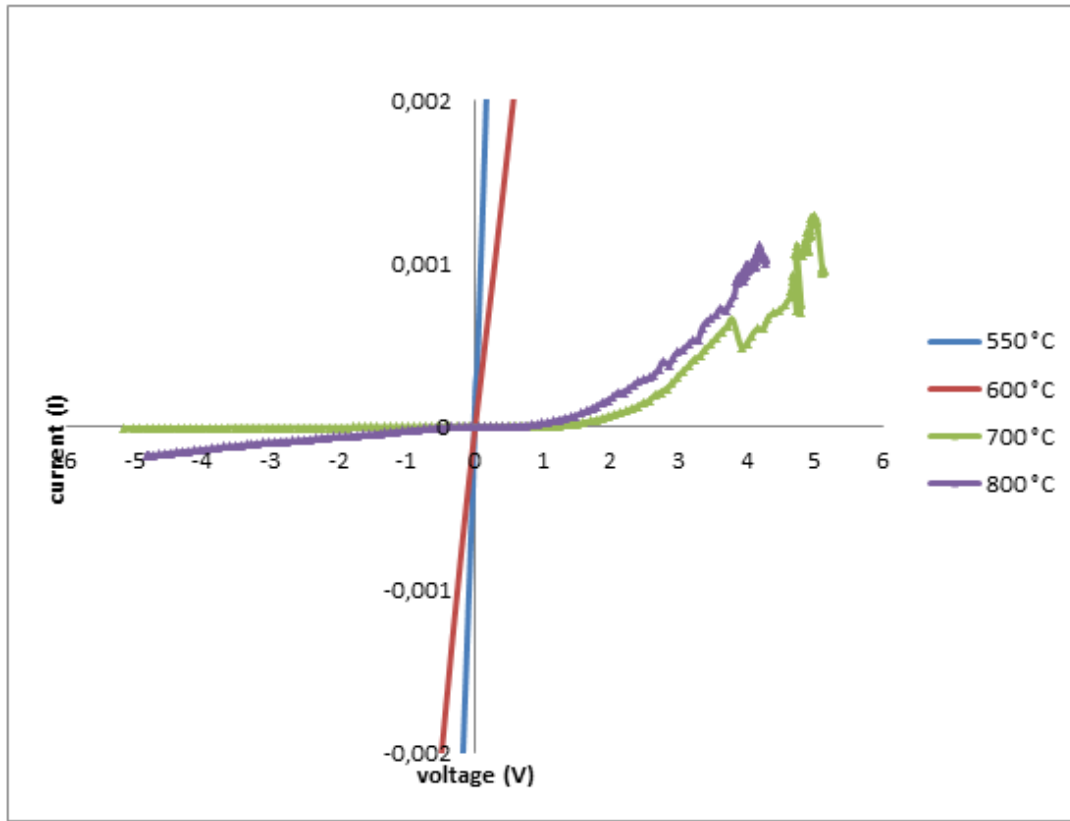
**Figure 7.14:** Measured current density-voltage characteristics of ZnO:Al/p-Si heterojunctions for different Al concentrations annealed at 700°C under vacuum for a) 0.8 % at. % b) 1.2 % at.

### 7.3.2. Effects of annealing temperature

Fig. 7.16 shows the current-voltage characteristic of the ZnO:Al/p-Si heterojunctions measured at room temperature under dark. The heterojunctions were with 1.2.% at Al concentration annealed at different temperatures in vacuum. The junctions annealed at 700 and 800°C exhibit a diode like behavior where the junction annealed at 550 and 600°C do not exhibit a diode like behavior. These two I-V curves are symmetrical, non-rectifying, and linear in the small voltage range, implying that the Cu/p-Si junction has ohmic-contact characteristics. When ohmic contact was fabricated with Cu-grid (~22  $\mu\text{m}$ -average grain size) through a mask on the front side by cold spray, ZnO:Al film on the p-Si wafer should be removed from surface due to high pressure of process air. Cross section SEM examinations as shown Fig.7.15 indicate that ZnO:Al film on the p-Si wafer was removed from surface due to high pressure of process air. for the junction annealed at 550 °C. But ZnO:Al film on the p-Si wafer wasn't removed from surface for the junction annealed at 700 °C. The diodes show rectifying behavior with rectification ratio ( $I_F/I_R$ ) values at a  $\pm 20$  V bias voltage showed in Table 7.4. The highest conductivity is observed when the heterojunction is annealed at 700°C.



**Figure 7.15:** Cross-section SEM image of the Cu/ZnO:Al/p-Si/Al heterojunction films, annealed at a) 500°C and b) 700 °C



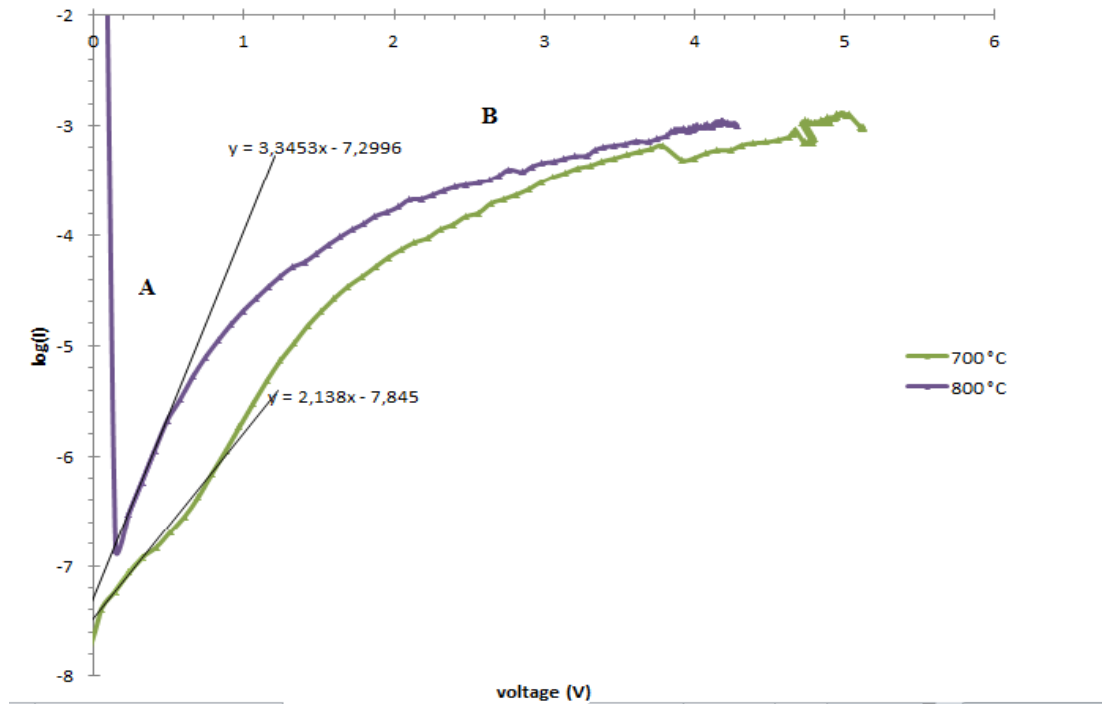
**Figure 7.16:** Measured current density-voltage characteristics of ZnO:Al/p-Si heterojunctions for 1.2 % at. Al concentration under dark condition, annealed under vacuum at different annealing temperatures.

Fig.7.17 shows the temperature dependence of the forward current in logarithmic scale. The forward currents can be classified into two regions according to the applied voltages. In region B, above  $\sim 1.2$  V, the forward current deviates from linearity due to the effect of a series resistance on the system. A simple series resistance model  $I = I_s \exp \left[ \frac{qV - IR_s}{nKT} \right]$  can be applied in an attempt to linearize the characteristics. In region A, below  $\sim 1.2$  V, the temperature dependence of the forward currents can be expressed by given Equation (5.1 or 5.10).

The temperature dependence of the parameter B depends on the dominant current transport mechanism. If the current is controlled by tunneling, B is a constant independent of temperature. If the current is controlled by some other mechanisms, B is generally dependent on temperature. In the plots of  $\log I$  versus V of n-ZnO:Al/p-Si heterojunctions, B is independent of the measurement temperature T, which indicates that the current in this region is dominated by a tunneling mechanism. The forward current can be explained by a multi-step tunneling model, which is attributed to the recombination of electrons, tunneling from ZnO:Al into the gap states in Si,

and holes tunneling across the heterojunction barrier from p-Si to n-ZnO:Al, where they hop between localized states through a multi-step tunneling process. The model for a multi-step tunneling capture-emission process across a semiconductor junction shows the dependence of the currents on both the temperatures and the voltages. This model has successfully explained the voltage and temperature dependencies observed for an amorphous n-Si/crystalline p-Si heterojunction. It is believed that it is also applicable to the case of nc-ZnO/p-Si heterojunctions.

In addition  $I_0$  values of these heterojunctions were given in Table 7.4. It is determined that the  $I_0$  values decrease with the decrease of ideality factor. It is suggested there is a relation between ideality factor of the diodes and resistivity of the ZnO:Al thin films annealed in vacuum.



**Figure 7.17:** Semilog I-V characteristics of ZnO:Al/p-Si heterojunctions under dark with 1.2 % at. Al annealed at 700°C and 800 °C under vacuum.

**Table 7.4:**  $I_0$ ,  $n$  and  $I_F/I_R$  values for ZnO:Al/ p-Si heterojunctions annealed at 700°C and 800°C.

Al Temperature (°C)	$I_0$ (A)	$n$	$I_F/I_R$
700	$1.428 \times 10^{-8}$	2.138	71.2
800	$2.488 \times 10^{-4}$	3.345	4.63

Fig.7.18 shows current-voltage characteristics of ZnO:Al/p-Si heterojunctions measure under light condition. The heterojunctions with 1.2 % at. Al concentration were annealed in vacuum at different annealing temperatures. By the affect of UV light source, the current flow of the heterojunction annealed at 700°C improves

where the current flow of the junction annealed at 800°C does not change considerably in reverse bias. This indicates the junction annealed at 700°C has photoelectric behavior.

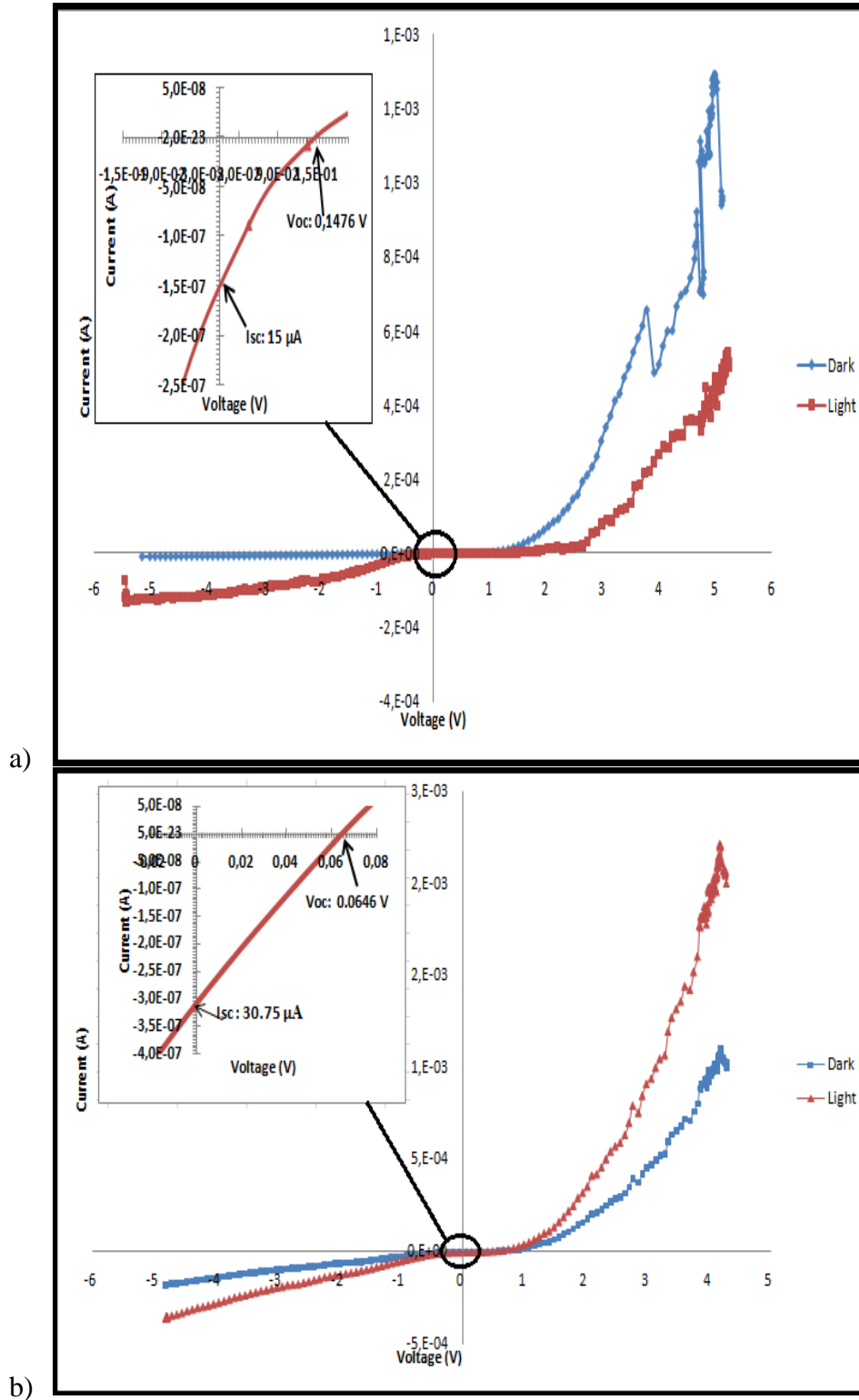


**Figure 7.18:** Measured current-voltage characteristics of ZnO:Al/p-Si Heterojunctions with 1.2 % at. Al dop concentration under dark and light, annealed under vacuum at a) 700 °C and b) 800 °C



In Table 7.5 the values of the current flow through the ZnO:Al/p-Si heterojunctions under dark and UV illumination at 10V reverse bias are shown. The current flows have risen slightly in each temperature with the UV illumination.

**Table 7.5:** Measured current values at -3V under dark and light for heterojunctions annealed at 700°C and 800°C.

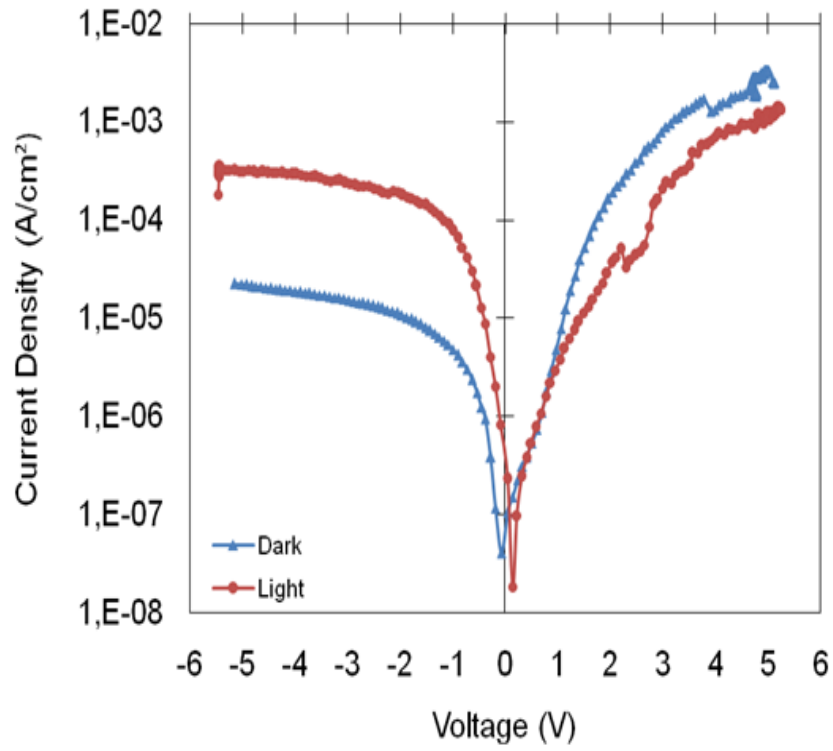
Annealing Temperature (°C)	$I_{\text{dark}}$	$I_{\text{light}}$
700	$-1 \times 10^{-5}$	$-9.24 \times 10^{-5}$
800	$-9.9 \times 10^{-5}$	$-2.004 \times 10^{-3}$

The "fill factor", more commonly known by its abbreviation "FF", is a parameter which, in conjunction with  $V_{\text{oc}}$  and  $I_{\text{sc}}$ , determines the maximum power from a solar cell. The FF is defined as the ratio of the maximum power from the solar cell to the product of  $V_{\text{oc}}$  and  $I_{\text{sc}}$ . The FF is most commonly determined from measurement of the IV curve as shown in insert of Figure 7.18a and b and is defined by Equation (7.1) as the maximum power divided by the product of  $I_{\text{sc}}$ ,  $V_{\text{oc}}$ , i.e [68]. The values of  $V_{\text{oc}}$ ,  $I_{\text{sc}}$ ,  $V_{\text{mp}}$  and  $I_{\text{mp}}$  are shown in Table 7.6. A high n-value not only degrades the FF, but since it will also usually signal high recombination, it gives low open-circuit voltages. Conversely, if IV curves become "squashed" or "rounded" due to unfavorable values of parasitic resistances or poor diode characteristics, then fill factor falls to low values, *e.g.*, below 40% [68]. Accordingly, fill factor provides a useful figure of merit for quality of a solar cell.

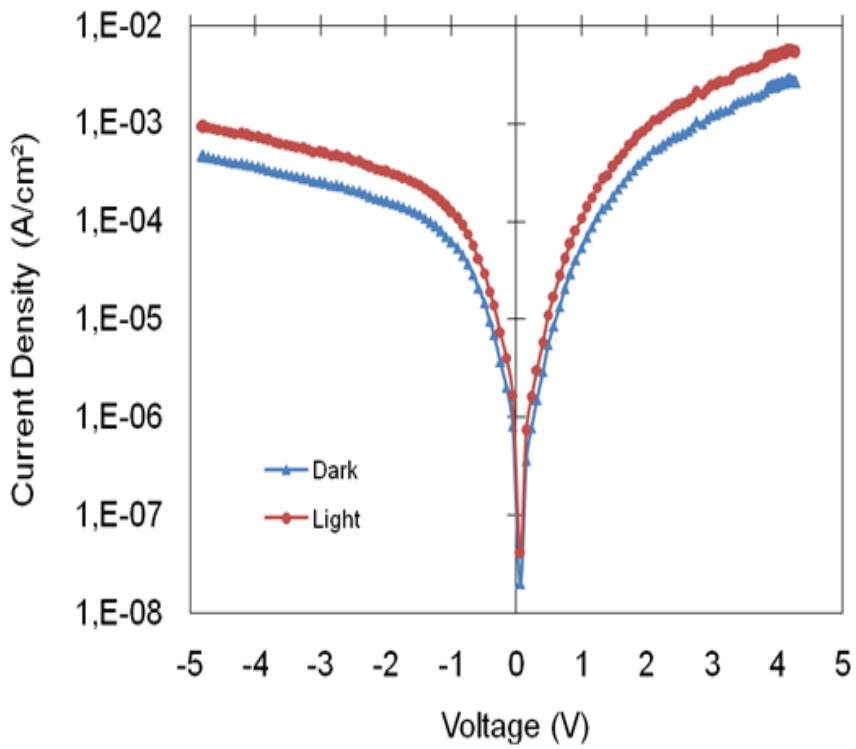
**Table 7.6:** Measured  $V_{\text{oc}}$ ,  $I_{\text{sc}}$ ,  $V_{\text{mp}}$ ,  $I_{\text{mp}}$  and FF values of heterojunctions under light for annealed at 700°C and 800°C.

Annealing Temperature (°C)	$V_{\text{oc}}$ (V)	$I_{\text{sc}}$ (μA)	$V_{\text{mp}}$ (V)	$I_{\text{mp}}$ (μA)	FF
700	0.1476	-15	0.0538	-760	%18.40
800	0.0646	-30.75	0.0235	-18.5	%21.88

Fig.7.19 shows the current-voltage characteristics of a ZnO:Al/p-Si heterojunctions measured at room temperature under dark and light. The investigated heterojunctions in this figure were with 1.2 % at. Al concentration annealed at different temperatures in vacuum. The curves in forward bias plotted according to measurements under the dark and light conditions are higher than the curves plotted in reverse bias that indicates that the junctions exhibit diode-like rectifying behavior at 700 °C and 800°C. The junction fabricated at 700°C shows highest current conduction under dark and light.



a)

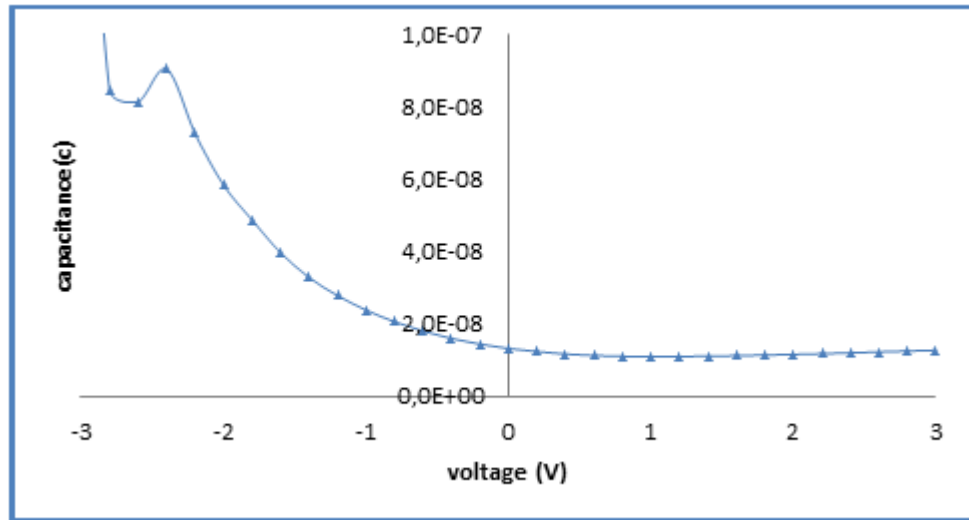


b)

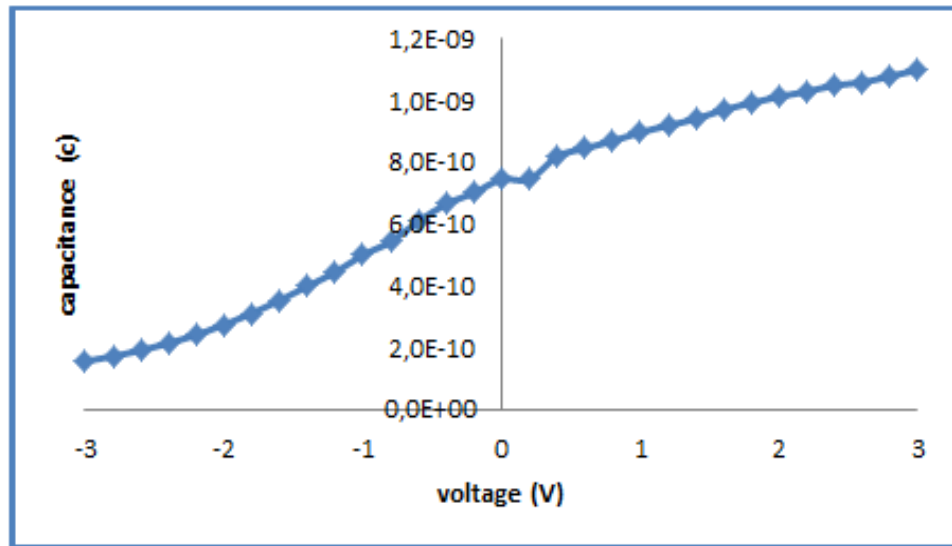
**Figure 7.19:** Measured current density-voltage characteristics of ZnO:Al/p-Si heterojunctions for 1.2 % at. Al concentration, annealed under vacuum at different annealing temperatures a) 700°C and b) 800°C.

#### 7.4. Capacitance-Voltage (C-V) Properties of ZnO:Al/p-Si

The capacitance measurements were performed under dark at room temperature at a frequency of 1 MHz under applied forward and reverse DC bias sweeps (−3 to 3 V) with an AC oscillation level of 0.2 mV. The potential barrier at the junction can be measured by small-signal Capacitance-Voltage (C-V) characteristics. Fig.7.20 presents the C-V characteristics in the reverse bias region at 700°C and 800°C for the n-ZnO:Al/p-Si heterojunctions at 1 MHz [89].



a)



b)

**Figure 7.20:** C-V characteristics in the reverse bias region at a) 700°C and b) 800°C for n-ZnO:Al/p-Si heterojunctions at 1MHz [89].

As can be seen, the capacitance of the heterojunction is decreased with an increase in the reverse bias with an approximately linear  $C^{-2}$ -V bias relationship as shown

Fig. 7.21a. This means that the depletion region in the vicinity of the heterojunction interface is expanded with an increase in the reverse bias [83].

As observed from the Fig. 7.21b,  $1/C^2$ -V variation is linear in the voltage range studied, indicating that there is little number of deep levels. The typical features of an n-type metal oxide semiconductor capacitor with an accumulation region are observed, indicating that the junction is abrupt. The variation of capacitance as the bias decreases is caused by changes of the thickness of the carrier depletion region [80].

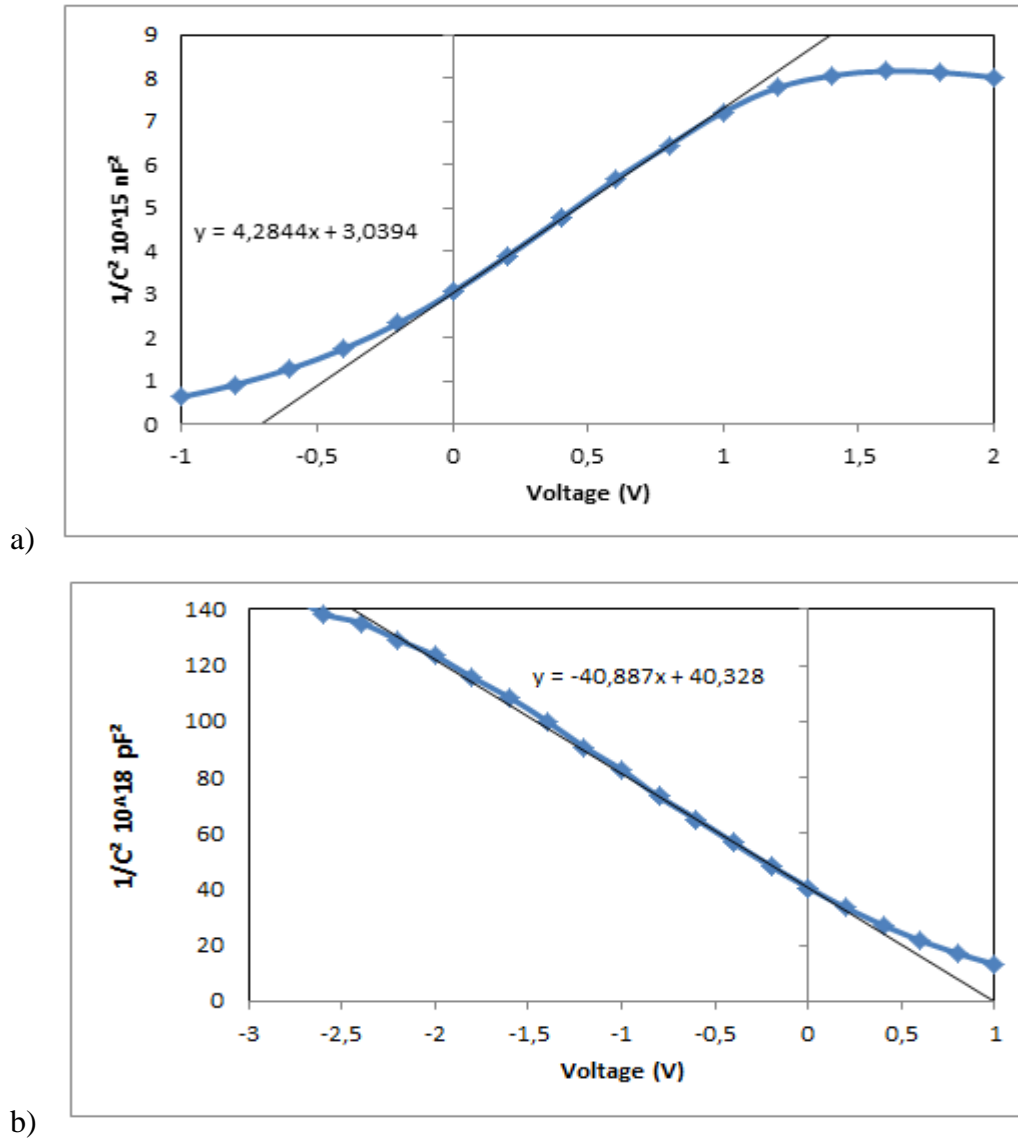


**Figure 7.21:**  $C^{-2}$ -V characteristics for the n-ZnO:Al/p-Si heterojunctions at 1MHz for at a) 700°C and b) 800°C [89].

This C-V characteristic is also described by the conventional heterojunction theory Equation (5.12). Using this formula, they can determine the effective space charge

density of the depletion region of both heterojunctions from the slope of the  $C^{-2}(V_{bi})$  relationship. For an applied reverse voltage  $V \gg kT/q$ , and knowing that  $N_a \gg N_d$ , the relationship between the depletion layer capacitance per unit area and the applied voltage is given by Equation (5.7) where  $V_{bi}$  is the built-in potential,  $\epsilon_s$  is the semiconductor permittivity and  $N_d$  its doping level. Assuming a uniform doping level in the semiconductor, the plot of  $1/C^2$  vs.  $V$  is a straight line, of which the intercept with the voltage axis gives the value of the built-in or diffusion potential ( $V_{bi}$ ). The slope of the straight line gives the ionized donor concentration ( $N_d$ ).

The width of depletion layer ( $W_D$ ) is calculated by the following equation (7.4) [83];

$$W_D = \sqrt{\frac{2\epsilon_s \epsilon_0 V_D}{qN_D}} \quad (7.4)$$

The values of  $V_{bi}$ ,  $N_D$  and  $W_D$  obtained are presented in Table 7.7 for  $\epsilon_r(\text{ZnO}) = 8.66$  and  $\epsilon_r(\text{Si}) = 11.70$ . These results indicate that the junction is an abrupt p-n type junction. The built-in potential  $V_{bi}$ , or diffusion potential, is estimated to be 0.70 and 0.98 eV for at annealed 700 °C and 800 °C, respectively. This result is consistent with the energy difference between the work functions of Si and ZnO. The Fermi level below the vacuum level is 4.97 eV for p-Si, and 4.25 eV for n-ZnO. The difference between them is 0.72 eV. The difference of built-in potential indicates on a different interface state density at the heterojunction interface or composition and strain. In nanocrystalline ZnO films, the ratio of volume to surface is larger than that of columnar films, and the strain in nanocrystalline films is smaller than that of columnar films. The most likely reason for a more complex behavior (n-ZnO:Al/p-Si and n ZnO:Al/n-Si), compared to the model of a simple p–n heterojunction, are the defects at or near the n-ZnO:Al/c-Si interface, which cause a Fermi energy pinning. The pinning effect makes the height of the energy barrier independent of the ZnO work function [83].

**Table 7.7:** Built-in potential, donor concentration and barrier heights for ZnO films grown at different substrate temperatures.

Substrate temperature (°C)	$V_{bi}$ (eV)	$N_D$ (cm <sup>-3</sup> )	$W_D$ (cm <sup>-3</sup> )
700	0.70	$4.28 \times 10^{15}$	57.64
800	0.98	$4.09 \times 10^{17}$	454.91



## 8. CONCLUSION

In this study the ZnO:Al films with 0.8, 1.0, 1.2 and 1.6 % at Al concentrations were fabricated on p-type silicon substrates by sol-gel dip coating technique. After immersing the p-type Si wafer substrates into the colloidal suspension, the samples were preheated at 400°C for 10 minutes. This procedure was repeated for four times. After the final preheating, the samples were then annealed at 550°C, 600°C, 700°C and 800°C annealing temperatures for 1 hour. The annealing ambients of the thin films were selected as air and vacuum to examine the changes in the physical properties. After the coating process, structural, electrical and heterojunction properties were determined.

Following conclusions can be drawn according to the results of this study:

1. ZnO:Al thin films were in hexagonal wurtzite crystal structure when annealed at 550°C, 600°C, 700°C. However the annealing process at 800 °C (for 1 h) resulted with the formation of the trapezium crystals indicating the occurrence of another zinc compound such as zinc silicate ( $\text{Zn}_2\text{SiO}_4$ ).
2. The average crystallite sizes had a tendency to decrease with increase in Al doping concentration. The decrease of the crystallite size resulted with the decrease of the film thickness. Thicknesses of the films decreased from 500 to 150 nm as Al concentration increases from 0.8 to 1.6 % at. The increase in Al concentration and change in the annealing ambient had nearly no influence on thickness where the increase in annealing temperature caused a decrease in the thickness of the films.
3. The minimum resistivity values were obtained from the film containing 1.2 % at. Al concentration which was annealed in vacuum at 800°C. As a general trend the resistivity of ZnO:Al thin films decreased with the increase of annealing temperature.

4. In forward bias the current through the ZnO:Al/p-Si heterojunctions changed with the applied voltage where in reverse bias the current through the heterojunctions had insignificant change under dark. These I-V characteristics of the ZnO:Al/ p-Si heterojunctions are similar with I-V characteristic of typical diode. The photoelectric behaviors were observed for the heterojunctions under light conditions. UV illumination improved the current through the ZnO:Al/p-Si heterojunctions in forward bias. In reverse bias the photocurrent caused by illumination was obviously much larger than the current under dark condition.
5. The electrical properties of the heterojunctions were investigated by Capacitance-Voltage (C-V) measurements. C-V curves were measured as a function of reverse bias at room temperature. C-V characterization techniques was used as a test of the interface homogeneity of the ZnO:Al/p-Si heterojunction.
6.  $1/C^2$ -V variation is linear in the voltage range, indicating that there is little number of deep levels. The typical features of an n-type metal oxide semiconductor capacitor with an accumulation region are observed, indicating that the junction is abrupt. The variation of capacitance as the bias decreases is caused by changes of the thickness of the carrier depletion region. The difference of built-in potential indicates on a different interface state density at the heterojunction interface or composition and strain. In nanocrystalline ZnO films, the ratio of volume to surface is larger than that of columnar films, and the strain in nanocrystalline films is smaller than that of columnar films.
7. Consequently, deposition of the 1.2 % at. Al doped ZnO:Al thin film on p type Si substrate by annealing at 700°C in vacuum, is the best candidate for the ZnO:Al /p-Si heterojunction to utilize in electronic devices.



## REFERENCES

- [1] **Ö Pehlivan.**, 2013. Growth And Morphological Characterization Of Intrinsic Hydrogenated Amorphous Silicon Thin Film For A-Si:H/C-Si Heterojunction Solar Cells, *Master Thesis*.
- [2] **M. Karaman.**, 2011. Characterization And Fabrication of Silicon Thin Films for Solar Cell Applications, *Master Thesis*.
- [3] **USA Patent.**, 1946. Light sensitive device, *U.S. Patent 2,402,662*, 25/06/1946.
- [4] **J. Perlin.**, 2010. The Silicon Solar Cell Turns 50, *National Renewable Energy Laboratory*. Retrieved 5 October 2010.
- [5] **M.A. Sharan.**, 2009. Efficiency enhancement of stationary solar energy based power conversion systems in Canada, *Applied Energy*, 86, 1405-1409.
- [6] **S. Andreas.**, 2012. Transparent Conducting Oxides, *Materials*, 5, 661-683.
- [7] **M. Lukas Schmidt, L. Judith MacManus-Driscoll.**, 2007. ZnO-Nanostructures, Defects and Devices, *Materials today* Volume 10 Issue 5 Pages 40-48.
- [8] **G.M. Wu, Y.F. Chen, H.C. Lu.**, 2010. Aluminum-Doped Zinc Oxide Thin Films Prepared by Sol-Gel and RF Magnetron Sputtering, *Proceedings of the VIII International Conference ION, Kazimierz Dolny, Poland*.
- [9] **D.C. Look, D.C. Reynolds, J.W. Hemsky, R.L. Jones, J.R. Sizelove.**, 1999. Al-doping effects on structure, electrical and optical properties of c-axis-orientated ZnO:Al thin films *Appl. Phys. Lett.* 75, 811.
- [10] **M. Sahal, B.Hartiti, A.Ridah, M.Mollar, B.Mari.**, 2008. Structural, electrical and optical properties of ZnO thin films deposited by sol-gel method, *Microelectronics Journal*, 39, 1425–1428.
- [11] **K. Ung Sim, S. Wook Shin, A.V. Moholkar, J. Ho Yun, J. Ha Moon , J. Hyeok Kim.**, 2010. Effects of dopant (Al, Ga, and In) on the characteristics of ZnO thin films prepared by RF magnetron sputtering system, *Current Applied Physics*, 10, 463–467.
- [12] **H.W. Leea, S.P. Laua, Y.G. Wang, K.Y. Tseb, H.H. Hngb, B.K.**, 2004. Structural, electrical and optical properties of Al-doped ZnO thin films prepared by filtered cathodic vacuum arc technique, *Taya Journal of Crystal Growth* 268 596–601.
- [13] **A.F. Lotus, Y.C. Kang, J.I. Walker, R.D. Ramsier, G.G. Chase.**, 2010. Effect of aluminum oxide doping on the structural, electrical, and optical properties of zinc oxide (AZO) nanofibers synthesized by electrospinning, *Materials Science and Engineering B*, 166, 61–66.

- [14] **M.-Chul Jun, S.-Uk Park, J.-Hyuk Koh.,** 2012. Comparative studies of Al-doped ZnO and Ga-doped ZnO transparent conducting oxide thin films Jun et al. *Nanoscale Research Letters*, 7:639.
- [15] **E. M. Mkawi, K. Ibrahim, M. K. M. Ali, M. A. Farrukh, A. S. Mohamed.,** 2015. The effect of dopant concentration on properties of transparent conducting Al-doped ZnO thin films for efficient  $\text{Cu}_2\text{ZnSnS}_4$  thin-film solar cells prepared by electrodeposition method, *Appl Nanosci* DOI 10.1007/s13204-015-0400-3.
- [16] **G. Srinivasan, R.T. Rajendra Kumar, J. Kumar.,** 2007. Influence of Al dopant on microstructure and optical properties of ZnO thin films prepared by sol–gel spin coating method, *Optical Materials*, 30, 314–317.
- [17] **Z.Q. Xu, H. Deng, Y. Li, Q.H. Guo, Y.R. Li.,** 2006. Characteristics of Al-doped c-axis orientation ZnO thin films prepared by the sol–gel method, *Materials Research Bulletin*, 41 354–358.
- [18] **H. Li, J. Wang, H. Liu, H. Zhang, X. Li.,** 2005. Zinc Oxide Films Prepared By Sol-Gel Method, *Journal of Crystal Growth*, 275, 943-946.
- [19] **K. Haga, T. Suzukia, Y. Kashiwaba, H. W Atanabe, B. P. Zhang, Y. Segawa.,** 2003. High-quality ZnO films prepared on Si wafers by low-pressure MO-CVD, *Thin Solid Films*, 433, 131–134.
- [20] **Y. M. Hu, C. W. Lin, J. C. A. Huang.,** 2006. Dependences of the Al thickness and annealing temperature on the structural, optical and electrical properties in ZnO/Al multilayers, *Thin Solid Films*, 497 130 – 134.
- [21] **S. J. Henley, M.N.R. Ashfold, D. Cherns.,** 2004. The growth of transparent conducting ZnO films by pulsed laser ablation, *Surface and Coatings Technology*, 177 –178, 271–276.
- [22] **H. Zhou, D. Yi, Z. Yu, L. Xiao, J. Li.,** 2007. Preparation of aluminum doped zinc oxide films and the study of their microstructure, electrical and optical properties, *Thin Solid Films*, 515, 6909–6914.
- [23] **F. Yakuphanoglu, Y. Caglar, M. Caglar, S. Alican.,** 2010. ZnO/p-Si heterojunction photodiode by sol–gel deposition of nanostructure n-ZnO film on p-Si substrate, *Materials Science in Semiconductor Processing*, 2010.
- [24] **A. E. Jimenéz Gonzalez, J. A. Soto Urueta.,** 1998. Optical transmittance and photo conductivity studies on ZnO:Al films prepared by the sol-gel technique, *Solar Energy Materials and Solar Cells*, 52, 345-353.
- [25] **D. R. Uhlmann, T. Suratwala, K. Davidson, J. M. Boulton, G. Teowee.,** 1997. Sol-gel derived coatings on glass, *Journal of Non-Crystalline Solids*, 218, 113-122.
- [26] **V. Musat, B. Teixeira, E. Fortunato, R. C. C. Monteiro, P. Vilarinho.,** 2004. Al-doped ZnO thin films by sol–gel method, *Surface and Coatings Technology*, 180-181, 659–662.
- [27] **W. M. Tsang, F. L. Wong, M. K. Fung, J. C. Chang, C. S. Lee, S. T. Lee.,** 2008. Transparent conducting aluminum-doped zinc oxide thin film

prepared by sol–gel process followed by laser irradiation treatment, *Thin Solid Films*, 517, 891–895.

- [28] **T. H. Breivik, S. Diplas, A. G. Ulyashin, A. E. Gunnæs, B. R. Olaisen, D. N. Wright, A. Holt, A. Olsen.,** 2007. Nano-structural properties of ZnO films for Si based heterojunction solar cells, *Thin Solid Films*, 515, 8479–8483.
- [29] **D. Song, B. Guo, Armin G. Aberle.,** 2002. Heterojunction properties of ZnO:Al/p-Si prepared by RF magnetron sputtering, *Optoelectronic and Microelectronic Materials and Devices, Conference*, 153-156.
- [30] **D. R. Askeland, P. P. Phule.,** 2006. The science and Engineering of Materials, *Master Thesis*.
- [31] **J. Singh.,** 2007. Electronic and Optoelectronic Properties of Semiconductor Structure, *Cambridge University Press*.
- [32] **S. M. Sze.,** 2002. Semiconductor Dvices: Physics and Technology, *John Willey and Sons Inc.*
- [33] Url-1< [http://www.learnabout-electronics.org/semiconductors\\_02.php](http://www.learnabout-electronics.org/semiconductors_02.php) > 14.10.2015
- [34] **L. Łukasiak, A. Jakubowski.,** 2010. History of Semiconductors, *Journal of Telecommunications and Information Technology*.
- [35] Url-2< <http://ece-www.colorado.edu/~bart/book/>> 14.10.2015
- [36] **Y. Singh.,** 2009. Semiconductor Devices, *I. K. International Pvt Ltd Press*.
- [37] **S. Mahajan, K. S. Sree Harsha.,** 1999. Principles of Growth and Processing of Semiconductors, *WCB/McGraw-Hill*.
- [38] Url-3< <http://hyperphysics.phy-astr.gsu.edu/hbase/solids/sili.html>> 14.10.2015
- [39] **H. Morkoç, Ü. Özgür.,** 2009. Zinc Oxide: Fundamentals, Materials and Device Technology, *Master Thesis*.
- [40] **K.Pui Sze.,** 2005. Process Development For Zno-Based Devices.*Master Thesis*.
- [41] **N. F. Habubi, S. S. Chial, S. Jabbar, W. Jabbar.,** 2012. Synthesis and Optical Properties of Sprayed ZnO and ZnO:Ga Thin Films, *Journal of the Arkansas Academy of Science*, Vol. 66.
- [42] **H. L. Hartnagel, A. L. Dawar, A. K. Jain, C. Jagadish.,** 1995. Semiconducting Transparent Thin Films, *Institute of Physics Publishing, Bristol*.
- [43] **R. Bel Hadj Tahar.,** 2005. Structural and electrical properties of aluminum-doped zinc oxide films prepared by sol–gel process, *Journal of the European Ceramic Society*, 25 3301–3306.
- [44] **X. Zi-qiang, D. Hong, L. Yan, C. Hang.,** 2006. Al-doping effects on structure, electrical and optical properties of c-axis-orientated ZnO:Al thin films. *Materials Science in Semiconductor Processing*, 9 132–135.
- [45] **D. H Zhang, T. L. Yang, Q. P. Wang, D. J. Zhang ,**2001. Electrical and optical properties of Al-doped transparent conducting ZnO films

- deposited on organic substrate by RF sputtering. *Mater. Chem. Phys.*, 68, 233–238.
- [46] **S. M. A. Durrani, A. M. Al-Shukri Iob, E. E. A. Khawaja**, 2000. Optical constants of zinc sulfide films determined from transmittance measurements, *Thin Solid Films*, 379, 199–202.
- [47] **J. F. Chang, M. H. Hon**, 2001. The effect of deposition temperature on the properties of Al-doped zinc oxide thin films, *Thin Solid Films*, 386, 79–86.
- [48] **Y. Igasaki, H. Kanma**, 2001. Argon gas pressure dependence of the properties of transparent conducting ZnO:Al films deposited on glass substrates, *Appl. Surf. Sci.* 169, 508–511.
- [49] **S. Brehme, F. Fenske, W. Fuhs, E. Nebauer, M. Poschenrieder, B. Selle, Sieber**, 1999. Free-carrier plasma resonance effects and electron transport in reactively sputtered degenerate ZnO:Al films. *Thin Solid Films*, 342, 167–173.
- [50] **M. L. Addonizio, A. AntonaiaCantele, G. Privato**, 1999. Transport mechanisms of RF sputtered Al-doped ZnO films by H<sub>2</sub> process gas dilution. *Thin Solid Films*, 349, 93–99.
- [51] **J. M. E. Harper, J. L. Vossen, W. Kern (Eds.)**, 1978. Thin Film Processes, *Academic Press, New York*, p. 175, Ch. II-5.
- [52] **D. Song, P. Widenborg, W. Chin, A. G. Aberle**, 2002. Investigation of lateral parameter variations of Al-doped zinc oxide films prepared on glass substrates by rf magnetron sputtering, *Solar Energy Materials & Solar Cells*, 73 1–20.
- [53] **K. Ellmer**, 2000. Magnetron sputtering of transparent conductive zinc oxide: relation between the sputtering parameters and the electronic properties, *J. Phys. D: Appl. Phys.* 33 R17–R32.
- [54] **B. Faure, G. Salazar-Alvarez, A. Ahniyaz, I. Villaluenga, G. Berriozabal, Y. R De Miguela, L. Bergstrom**, 2013. Dispersion and surface functionalization of oxide nanoparticles for transparent photocatalytic and UV-protecting coatings and sunscreens, *Science and Technology of Advanced Materials*, 14 023001 (23pp).
- [55] **C. J. Brinker, G. W. Scherer**, 1990. Sol-Gel Science: The Physics and Chemistry of Sol-Gel Processing. *New York: Academic Press, Inc.*
- [56] **C. J Brinker**, 1988. Hydrolysis and Condensation of Silicates: Effects on Structure. *Journal of Non-Crystalline Solids*, vol. 100, pp. 31-50, 1988.
- [57] **S. K. Young**, 2002. Overview of Sol-Gel Science and Technology
- [58] **L. C. Klein**. 1988. Sol-Gel Technology for Thin Films, Fibers, Preforms, Electronics and Specialty Shapes, *ISBN 0-8155-1154-X Noyes Publication*, p.52.

- [59] **M. Nogami, Y. Moriya.,** 1980. Journal of Non-Crystalline Solids Vol.37, pp.191-201.
- [60] **Y. Huang, H. Zheng, I. Ball.,** 2001. Advances In Sol-Gel Technology, *Master Thesis*.
- [61] **M. A. Johnson.** 2003. Viscoelastic Roll Coating Flows, *Master Thesis*.
- [62] **C. J. Brinker., A. J. Hurd., G. C. Frye Schunk, C. S. Ashley.,** 1991. Sol-Gel Thin film Fomiation, *J. Ceiam. Soc. Jpn* 99 1991 862-877.
- [63] **R. Krechetnikov, G. M. Homsy.,** 2005. Coating in the presence of a substrate-liquid interaction potential, *Physics Of Fluids*, 17, 102105.
- [64] **C. T. Jones.,** 2000. Dip coating, *Metal Finishing*, 98, 172-174.
- [65] **S. Li. Sheng.,**2005. p-n Junction Diodes, *Master Thesis*.
- [66] **Dr. A. Sproul.** N.D. Understanding the p-n Junction, *UNSW Bookshop*.
- [67]Url-4<<http://hyperphysics.phy-astr.gsu.edu/hbase/solids/pnjun.html>> 21.10.2015
- [68]Url-5<<http://www.pveducation.org/pvcdrom/pn-junction/bias-of-pn-junction>> 21.10.2015
- [69]Url-6<[http://www.electronicshub.org/characteristics-and-working-of-p-n-junction-diode/#PN Junction Diode](http://www.electronicshub.org/characteristics-and-working-of-p-n-junction-diode/#PN_Junction_Diode)> 21.10.2015
- [70] Url-7< [http://www.electronics-tutorials.ws/diode/diode\\_3.html](http://www.electronics-tutorials.ws/diode/diode_3.html)> 21.10.2015
- [71] **B.M. Wilamowski.** 2010. Semiconductor Diode, *Master's Thesis*.
- [72] **H. Bo, M. Zhong Quan, X. Jing, Z. Lei, Z. Nan Sheng, L. Feng, S. Cheng, S. Ling, Z. Cheng Yue, Y. Zheng Shan, Y. Yan Ting.,** 2009. Characterization of AZO/p-Si heterojunction prepared by DC magnetron sputtering, *Materials Science in Semiconductor Processing*, 12, 248-252.
- [73] **N. Baydogan, O. Ozdemir, H. Cimenoglu.,** 2013. The improvement in the electrical properties of nanospherical ZnO:Al thin film exposed to irradiation using a Co-60 radioisotope, *Radiation Physics and Chemistry* 89 (2013) 20–27.
- [73] **P K Patel, V A Kheraj, C F Panchal, M S Desai, P D Vakil, K J Patel.,** 2009. Automated measurements of junction characteristics to evaluate parameters for semiconductor diodes, *Indian Journal of Pure & Applied Physics*, Vol.47 pp.517-522.
- [74]Url-8<<http://conceptselectronics.com/diodes/effect-temperature-diode-characteristics/>> 21.10.2015
- [75] **V. Midili.,** 2012. Realization of a capacitance-voltage measurement system for semiconductor characterization, *Master Thesis Espoo*.
- [76] **F. Chaabouni, M.Abaab, B. Rezig.,** 2006. Characterization of n-ZnO/p-Si films grown by magnetron sputtering, *Superlattices and Microstructures*, 39 171–178.

- [77] **V. Tvarozek, P. Sutta, S. Flickyngerova, I. Novotny, P. Gaspierik, M. Netrvalova, E. Vavrinsky.,** 2009. Preparation of transparent conductive AZO thin films for solar cells
- [78] **O. Lupan, S. Shishiyanu, V. Ursaki, H. Khallaf, L. Chowb, T. Shishiyanu, V. Sontea, E. Monaico, S. Railean.,** 2009. Synthesis of nanostructured Al-doped zinc oxide films on Si for solar cells applications, *Solar Energy Materials & Solar Cells*, 93 1417–1422.
- [79] **J. Hun Park, K. Hyuk Pak, C.-Ryung Cho.,** 2006. Deposition-Temperature Effects on AZO Thin Films Prepared by RF Magnetron Sputtering and Their Physical Properties, *Journal of the Korean Physical Society*, Vol. 49, pp. S584-S588.
- [80] **Y. Zhang, J. Xu, B. Lin, Z. Fu, S. Zhong, C. Liu, Z. Zhang.,** 2006. Fabrication and electrical characterization of nanocrystalline ZnO/Si heterojunctions, *Applied Surface Science*, 252, 3449–3453.
- [81] **D. Song, D. -Holger Neuhaus, J. Xia, G. Armin Aberle.,** 2002. Structure and characteristics of ZnO:Al/n-Si heterojunctions prepared by magnetron sputtering, *Thin Solid Films*, 422 180–185.
- [82] **L. Li, C. X. Shan, B. H. Li, B. Yao, D. Z. Shen, B. Chu, Y. M. Lu.,** 2010. Light-Harvesting in n-ZnO/p-Silicon Heterojunctions, *Journal Of Electronic Materials*, Vol. 39, No. 11.
- [83] **R. Romero, M. C. López, D. Leinen, F. Mart'ín, J.R. Ramos-Barrado.,** 2004. Electrical properties of the n-ZnO/c-Si heterojunction prepared by chemical spray pyrolysis, *Materials Science and Engineering*, B 110 87–93.
- [84] **Ü. H. Tuğral.,** 2010. Characterization of Nanostructured ZnO:Al Films and The Effect of Beta Radiation on Their Colour Paramaters, *Master Thesis*.
- [85] **M. Tekin.,** 2009. Investigation on Structural, Optical and Electrical Properties and Behaviour Against Gamma Irridiation of Al:ZnO Thin Films Prepared by Sol-Gel Spin Coating Method, *Master Thesis*.
- [86] **J. Mass, P. Bhattacharya, RS. Katiyar.,** 2003. Effect of high substrate temperature on Al-doped ZnO thin films grown by pulsed laser deposition, *Mater Sci Eng*, B 103:9.
- [87] **M. Tekin, H. Tugral, Ö. Özdemir, H. Çimenoglu, E. S. Kayalı, A. B. Tugrul, N. Baydogan, M. Baydogan, N. Altinsoy, G. Albayrak, H. Sengel, F. Akmaz, A. Parlar.,** 2009. Investigation of heat treatment and Al Doping on irradiated nanosize hexagonal ZnO, *5th International Advanced Technologies Symposium (IATS'09), Karabuk, Turkey*.
- [88] **N. Baydoğan, O. Karacasu, H. Çimenoglu.,** 2012. Effect of annealing temperature on ZnO:Al/p-Si heterojunctions, *Thin Solid Films*, 520 5790-5796
- [89] **N. Baydogan, Y. Gokce, M. Baydogan, H. Cimenoglu.,** 2013. Capacitance-Voltage (C-V) Properties of ZnO:Al/p-Si Heterojunctions, *Defect and Diffusion Forum Vols. 334-335 (2013) pp 349-352*.

- [90] **N. Baydogan, O. Ozdemir, H. Cimenoglu.,** 2013. The improvement in the electrical properties of nanospherical ZnO:Al thin film exposed to irradiation using a Co-60 radioisotope, *Radiation Physics and Chemistry* 89 (2013) 20–27.





## **APPENDICES**

**APPENDIX A.1:** Average crystallite sizes and relative intensities changing of the peak diffractions depend on Al concentration in vacuum ambient.

**APPENDIX A.2:** Average crystallite sizes and relative intensities changing of the peak diffractions at 1.2 at. % Al dop concentration in oxygen ambient depend on annealing temperature



## APPENDIX A.1:

**Table A.1:** Average crystallite sizes and relative intensities changing of the peak diffractions depend on Al concentration in vacuum.

Dopant Concentration Al at. %	Relative Intensity (100)	Crystallite Size (nm) (100)	Relative Intensity (002)	Crystallite Size (nm) (002)	Relative Intensity (101)	Crystallite Size (nm) (101)
0.8	91	40.25	96	43.35	100	44.20
1.0	82	30.18	87	33.26	97	38.54
1.2	76	24.55	83	27.12	95	28.25
1.6	74	18.90	80	19.10	92	19.32

## APPENDIX A.2:

**Table A.2:** Average crystallite sizes and relative intensities changing of the peak diffractions at % 1.2 at. Al dop concentration in air depend on annealing temperature

Annealing Temperature (°C)	Relative Intensity (100)	Crystallite Size (nm) (100)	Relative Intensity (002)	Crystallite Size (nm) (002)	Relative Intensity (101)	Crystallite Size (nm) (101)
550	65	20.95	79	27.80	89	28.00
600	70	22.15	81	29.52	92	32.00
700	76	29.80	83	38.26	95	45.00
800	82	38.92	96	49.57	100	58.00



## CURRICULUM VITAE



**Name Surname** : Yeliz KÖSE

**Place and Date of Birth** : Bursa 02/10/1987

**E-Mail** : yelissgokce@hotmail.com

### EDUCATION

**B.Sc.** :İstanbul University

### PROFESSIONAL EXPERIENCE AND REWARDS:

- De-Ka Electronic In. / R&D Engineer / 02.2011–09.2012
- Gülaylar Group / Purchase Engineer / 09.2012–03.2014

### PUBLICATIONS, PRESENTATIONS AND PATENTS ON THE THESIS:

- **Nilgün Baydoğan, Yeliz Gökçe, Murat Baydoğan, Hüseyin Çimenoglu.** 2012. "Capacitance-Voltage (C-V) Properties of ZnO:Al/p-Si Heterojunctions", *Defect Diffus. Forum*, Vol. 334-335, s. 349-352.